

Analysis and Modelling of Atmospheric Transport Over Open-Pit Mines

by
Seyedahmad Kia

A Thesis
presented to
The University of Guelph

In partial fulfilment of requirements
for the degree of
Doctor of Philosophy
in
Mechanical Engineering

Guelph, Ontario, Canada

© Seyedahmad Kia, December, 2021

ABSTRACT

ANALYSIS AND MODELLING OF ATMOSPHERIC TRANSPORT OVER OPEN-PIT MINES

Seyedahmad Kia

University of Guelph, 2021

Advisors:

Dr. Amir A. Aliabadi

Dr. Brian Freeman

Diagnostic models of wind field and pollutant dispersion face difficulty when applied to complex terrain. Open-pit mines are an example of this difficult environment. To elucidate such difficulties, two models are developed and compared with one another. The first model is based on the prognostic Computational Fluid Dynamics-Lagrangian Stochastic (CFD-LS) paradigm, while the second model is based on the diagnostic CALifornia PUFF (CALPUFF) software. Two mine depths (100 [m] and 500 [m]) and three thermal stability conditions (unstable, neutral, and stable) are investigated using the two models. The CFD results showed that the skimming flow is only predicted under the neutral case, while more complex flow patterns emerge otherwise. Under the unstable case, the shallow and deep mines induce enhanced mixing downstream of the mine, resulting in substantial vertical plume transport and dilution of the pollutants released from the mine. Under the stable case, the plume from the shallow mine is restricted to the surface layer downstream of the mine. However, under the stable case, the plume from the deep mine rises into the substantial portion of the boundary layer due to the formation of a standing wave over and inside the mine. The results suggest that the CFD model can predict transport phenomena over open-pit mines reliably, so that the meteorological fields may be incorporated in operational models to improve the

accuracy of their predictions. On the other hand, the CALPUFF model generally deviates from CFD-LS predictions, and the disagreement between the two models is the greatest when modeling the deep mine, under neutral/stable conditions, or when its solutions are considered close to the mine edge. Among many reasons, the variances appear to be related to the internal algorithms of the CALPUFF model to predict the wind field structure appropriately. The results should caution practitioners considering diagnostic models for application over complex terrain, with opportunities to investigate such discrepancies at greater detail in follow up research.

Dedication

I dedicate my dissertation work to my dear father, who has been nicely my supporter until my research was fully finished, my beloved mother who, for months past, has encouraged me attentively with her fullest and truest attention to accomplish my work with truthful self-confidence, and my bother, who is always my best friend.

Contributions Statement

The Very Large-Eddy Simulation (VLES) method used in Computational Fluid Dynamics (CFD) analysis was initially developed by Dr. Amir A. Aliabadi at the University of Guelph [7] and Dr. Mojtaba Ahmadi-Baloutaki at Conestoga College [1]. It was further refined and developed for application to the synthetic mines by the author [68].

The CALifornia PUFF (CALPUFF) model was originally developed by Sigma Research Corporation (SRC), now Exponent, Inc. The CALPUFF View, which is a third party management tool that makes it easier to work with, was developed by Lakes Environmental Software. The author adapted the CALPUFF model to run the synthetic mines simulations based on the flow fields extracted from the CFD model.

The Lagrangian Stochastic (LS) model development and analysis was conducted by Dr. John Wilson and Dr. Thomas Flesch at the University of Alberta [142, 143]. The author provided flow fields to this model using the CFD results and analyzed the output of the LS model.

The author obtained field monitoring data in an actual mine using the mini SONic Detection And Ranging (SODAR) device. Other members of the Atmospheric Innovations Research (AIR) laboratory, University of Alberta, and industrial partners conducted other measurements in support of the CFD model validation. Such measurements included the Tethered And Navigated Air Blimp (TANAB) [21, 96] and ultrasonic anemometers.

Acknowledgments

The author wholeheartedly thanks Dr. Amir A. Aliabadi (University of Guelph), Dr. Brian Freeman (Lakes Environmental Software), and Dr. Thomas Flesch (University of Alberta), for their passionate mentorship and everlasting support that made this research see the light. The author also thanks feedback from Dr. Bahram Gharabaghi (University of Guelph), Dr. Scott Krayenhoff (University of Guelph), and Dr. Jesse Thé (Lakes Environmental Software).

The Tethered And Navigated Air Blimp (TANAB) was partially developed by the assistance of Denis Clement, Jason Dorsers, Katharine McNair, James Stock, Darian Vyriotes, Amanda Pinto, and Phillip Labarge. The author thanks Andrew F. Byerlay for designing and constructing the tether reel system for TANAB. The author thanks Nikolaos Veriotes and Manoj K. Nambiar for field assistance in collecting environmental data. The author is indebted to Steve Nyman, Chris Duiker, Peter Purvis, Manuela Racki, Jeffrey Defoe, Joanne Ryks, Ryan Smith, James Bracken, and Samantha French at the University of Guelph, who helped with the campaign logistics. Special credit is directed toward Amanda Sawlor, Datev Dodkelian, Esra Mohamed, Di Cheng, Randy Regan, Margaret Love, and Angela Vuk at the University of Guelph for administrative support. The computational platforms were set up with the assistance of IT staff Jeff Madge, Joel Best, and Matthew Kent at the University of Guelph. Technical guidance from John D. Wilson from University of Alberta is appreciated.

In-kind technical support for this work was provided by Rowan Williams Davies and Irwin, Inc. (RWDI). This work was supported by the University of Guelph, Ed McBean

philanthropic fund; the Discovery Grant program (401231) from the Natural Sciences and Engineering Research Council (NSERC) of Canada; Government of Ontario through the Ontario Centres of Excellence (OCE) under the Alberta-Ontario Innovation Program (AOIP) (053450); and Emission Reduction Alberta (ERA) (053498). The author was partially financially supported by the University of Guelph and Lakes Environmental Software.

Table of Contents

List of Tables	xii
List of Figures	xv
List of Abbreviations	xvi
List of Mathematical Symbols	xviii
1 Introduction	1
1.1 Methods of Quantifying Area-fugitive Emissions from Complex Terrains . . .	3
1.1.1 Flux Chamber, Eddy Covariance, and Flux Gradient Paradigms . . .	3
1.1.2 Methods Employing High Spatiotemporal Resolution Modeling	5
1.2 Research Gaps and Objectives	17
1.3 Structure of the Thesis	19
2 Methodology	20
2.1 Actual Mine Environment and Observations	20
2.2 Computational Fluid Dynamics (CFD) Model	25
2.2.1 Calculation of the CFD Model Friction Velocity and Obukhov Length at the Reference Height	31
2.2.2 Model Geometry and Domain Size	33
2.2.3 Numerical Schemes, Solution Control, Averaging, and Probing	35
2.2.4 Grid Resolution	38
2.3 Lagrangian Stochastic (LS) Model	40
2.4 CALifornia PUFF (CALPUFF) Model	41
2.4.1 Simulation Approach	45
2.5 Statistical Analysis	50
3 Results and Discussion	52
3.1 CFD	52
3.1.1 Comparison Against Observations	52
3.1.2 Spatial Variability of Fields	56
3.1.3 Surface-Layer Profiles	63

3.2	CALPUFF-CFD-LS	68
3.2.1	Plume Visualization for CALPUFF and CFD-LS Models	68
3.2.2	Different CALPUFF Weather Station Setups	71
3.3	Implications	83
4	Conclusions, Limitations, and Recommendations	85
4.1	Conclusions	85
4.2	Limitations	88
4.3	Recommendations	88
	References	89
A	Literature Summary Tables: Flux Chamber (FC), Eddy Covariance (EC), and Flux Gradient (FG) Methods	104
B	Literature Summary Tables: Computational Fluid Dynamics (CFD) Models	106
C	Literature Summary Tables: CALifornia PUFF (CALPUFF) Model	112
D	Literature Summary Tables: Lagrangian Stochastic (LS) Model	116
E	Literature Summary Tables: Inverse Dispersion Modelling (IDM) Methods	118
F	Surface-Layer Profiles	121
G	Code and Data Availability	132
H	Published Work	133
H.1	Peer-Reviewed Journal Papers	133
H.2	Refereed Conferences	133

List of Tables

2.1	Dimensions of the stepped shallow and deep mines.	33
2.2	CFD input variables for different thermal stability and mine depth simulation cases.	36
2.3	Different mesh grading options in the horizontal and vertical regions of the simulation domain.	40
2.4	Bias (RMSE) for mean horizontal velocity (\bar{U}) and potential temperature ($\bar{\Theta}$) calculated for CFD on profile P3 with different cell numbers versus observations; data reported for the shallow mine case under thermally-unstable condition.	40
2.5	Monin-Obukhov Length classification for atmospheric stability [122].	43
2.6	Emission rate and location for the center of emission sources (S1 to S5) for shallow and deep cases. The z value for shallow and deep cases are 50 and 250 [m] from bottom of the pit, respectively, in a terrain-following coordinate system.	47
2.7	The number of surface stations inside and outside the mine for meteorological forcing of the CALMET model.	49
2.8	The field measurement and model development activities that supported this thesis.	50
3.1	Friction velocity and Obukhov length: observed and predicted by CFD on profile P3; data reported for shallow and deep mine cases; data reported under various thermal stability conditions.	53
3.2	Bias (RMSE) for mean horizontal wind speed (\bar{U}) and potential temperature ($\bar{\Theta}$) calculated for CFD versus observations; data reported for shallow and deep mine cases; data reported under various thermal stability conditions.	58
3.3	Bias [$\mu\text{g m}^{-3}$] (RMSE [$\mu\text{g m}^{-3}$]) of the tracer concentration outside of the mine, predicted by CALPUFF against CFD-LS for different locations of surface stations and thermal stability conditions for case C6 of the shallow and deep mines.	79
3.4	$FAC2$ percentage of the tracer concentration, predicted by CALPUFF against CFD-LS for different locations of surface stations and thermal stability conditions for case C6 of the shallow and deep mines.	79

3.5	Bias [m s^{-1}] (RMSE [m s^{-1}]) of horizontal wind speed inside and outside of the mine at 10 [m] above surface predicted by CALMET against CFD-LS for different locations of surface stations and thermal stability conditions for case C6 of the shallow and deep mines.	80
3.6	Bias [m s^{-1}] (RMSE [m s^{-1}]) of wind speed on vertical boundary-layer profiles inside and downstream of the mine, predicted by CALMET versus CFD-LS for different locations of surface stations and thermal stability conditions for case C6 of the shallow and deep mines.	80
3.7	MAE [Degree] of horizontal wind direction at 10 [m] above surface inside and outside of the mine predicted by CALMET against CFD-LS for different locations of surface stations and thermal stability conditions for case C6 of the shallow and deep mines.	81
3.8	MAE [Degree] of wind direction on boundary-layer profiles inside and downstream of the mine, predicted by CALMET against CFD-LS for different locations of surface stations and thermal stability conditions for case C6 of the shallow and deep mines.	81
A.1	Literature review of Flux Chamber (FC), Eddy Covariance (EC), and Flux Gradient (FG) methods on GHG emission flux quantification.	104
B.1	Literature review of CFD simulations over simple and complex terrains. . . .	106
C.1	Literature review of CALMET/CALPUFF and hybrid simulations over simple and complex terrains.	112
D.1	Literature review of Lagrangian Stochastic (LS) simulations over simple and complex terrains.	116
E.1	Literature review of IDM simulations over simple and complex terrains. . . .	118

List of Figures

1.1	A flux chamber used to measure GHG emissions from a tailings pond in an open-pit mining facility; photo courtesy of Dr. Thomas Flesch.	4
1.2	An eddy covariance sensor used to measure GHG emissions from an open-pit mining facility; photo courtesy of Dr. Thomas Flesch.	5
1.3	Illustration of an Inverse Dispersion Modelling (IDM) technique: 1) the source emits gas at a rate Q [kg s^{-1}]; 2) gas concentration C [$\mu\text{g m}^{-3}$] is measured downwind of the source (either near the ground or above the surface using air sampling); 3) a dispersion model predicts the normalized concentration C/Q_{sim} at the downwind location; 4) the emission rate Q [kg s^{-1}] is determined by dividing the measured C [$\mu\text{g m}^{-3}$] by the predicted C/Q_{sim} . For most gases a background concentration C_b [$\mu\text{g m}^{-3}$] needs to be subtracted from the observations; Figure courtesy of Dr. Thomas Flesch.	16
2.1	Summary of the thesis procedure.	21
2.2	a) Map of the regional area where the mining facility is located; b) location of the meteorological instruments deployed at the site for model comparison, color coded with surface height above sea level; figure extracted from Nahian et al. (2020) [95].	22
2.3	mini SODAR used at the site; photo courtesy of Dr. Amir A. Aliabadi. . . .	23
2.4	Tethered And Navigated Air Blimp (TANAB) used at the site; photo courtesy of Dr. Amir A. Aliabadi.	24
2.5	a) Shallow and b) deep synthetic mine geometries, c) shallow and d) deep synthetic mine walls.	34
2.6	Top view of probing locations.	37
2.7	a) Mean horizontal velocity (\bar{U}) and b) potential temperature ($\bar{\Theta}$) profiles at P3 versus observations with different cell numbers for the thermally-unstable shallow mine simulation; note the Tethered Air Blimp (TAB) is another name for TANAB.	39
2.8	a) Shallow and b) deep synthetic mine geometries generated by CALPUFF View.	46
2.9	Location of emission sources, discrete receptors, and upper air stations in the CALPUFF domain.	47

2.10	Arrangement of surface and upper air stations associated with the operational case C6; location of the validation points for wind field modeling using CALPUFF.	49
3.1	Mean horizontal wind speed (\bar{U}) and potential temperature ($\bar{\Theta}$) profiles predicted by CFD (P1 to P5) and measured using observations (TANAB (TAB), SODAR) for thermally-unstable shallow (a and b) and deep (c and d) mine cases.	55
3.2	Mean horizontal wind speed (\bar{U}) profiles predicted by CFD (P1 to P5) and measured using observations (SODAR) for thermally-neutral shallow (a) and deep (b) mine cases.	56
3.3	Mean horizontal wind speed (\bar{U}) and potential temperature ($\bar{\Theta}$) profiles predicted by CFD (P1 to P5) and measured using observations (TANAB (TAB), SODAR) for thermally-stable shallow (a and b) and deep (c and d) mine cases.	57
3.4	Wind field velocity vectors and magnitude contours for thermally-unstable (a and b), thermally-neutral (c and d), and thermally-stable (e and f) cases for the shallow (a, c, e) and deep (b, d, f) mines.	60
3.5	Passive field contours for thermally-unstable (a and b), thermally-neutral (c and d), and thermally-stable (e and f) cases for the shallow (a, c, e) and deep (b, d, f) mines.	62
3.6	Wind field velocity vectors and passive scalar contours for thermally-unstable (a and b), thermally-neutral (c and d), and thermally-stable (e and f) cases for the shallow (a, c, e) and deep (b, d, f) mines on a horizontal cross section at 10 [m] above grade.	64
3.7	Contour plots of surface tracer concentration for the shallow mine case, as predicted from CALPUFF case C6 (left) and CFD-LS (right).	69
3.8	Contour plots showing a vertical slice of tracer concentration downwind of the shallow mine ($x=7000$ [m]), as predicted with CALPUFF case C6 (left) and CFD-LS (right). The distribution of sources in the mine is shown below the plots for reference.	70
3.9	Bias [$\mu\text{g m}^{-3}$] and RMSE [$\mu\text{g m}^{-3}$] of the tracer concentrations outside of the mine, comparing CALPUFF predictions against CFD-LS over different number of surface station setting cases and thermal stability conditions of the shallow (a and b) and deep (c and d) mine configurations.	72
3.10	FAC2 [%] of the surface tracer concentrations predicted by CALPUFF against the CFD-LS values over the different number of CALPUFF surface station settings and thermal stability conditions for the shallow (a) and deep (b) mine configurations.	72
3.11	Bias [m s^{-1}] and RMSE [m s^{-1}] of horizontal wind speed inside and outside of the mine at 10 [m] above surface, comparing CALMET predictions against CFD-LS over different number of surface station cases and thermal stability conditions of the shallow (a and b) and deep (c and d) mine configurations.	74

3.12	Bias [m s^{-1}] and RMSE [m s^{-1}] of horizontal wind speed on vertical boundary-layer profiles inside and downstream of the mine predicted by CALMET against CFD-LS over different number of surface station cases and thermal stability conditions of the shallow (a and b) and deep (c and d) mine configurations.	75
3.13	MAE [Degree] of horizontal wind direction at 10 [m] above surface inside and outside the mine predicted by CALMET against CFD-LS over different number of surface station cases and thermal stability conditions of the shallow (a) and deep (b) mine configurations.	77
3.14	MAE [Degree] of wind direction on boundary-layer profiles inside and downstream of the mine predicted by CALMET against CFD-LS over different number of surface station cases under different thermal stability conditions of the shallow (a) and deep (b) mine configurations.	77
3.15	Bias [$\mu\text{g m}^{-3}$] and RMSE [$\mu\text{g m}^{-3}$] of the tracer concentration predicted by CALPUFF against CFD-LS over different receptor locations in the stream-wise direction at 10 [m] above surface under different thermal stability conditions of the shallow (a and b) and deep (c and d) mines for case C6.	82
F.1	Profiles of normalized mean velocity in the x -direction (\overline{U}_x) outside (P3 to P10) and inside (P11 to P13) the mine for different thermal stability cases and topographies; a) shallow and b) deep mines.	122
F.2	Profiles of normalized mean velocity in the z -direction (\overline{U}_z) outside (P3 to P10) and inside (P11 to P13) the mine for different thermal stability cases and topographies; a) shallow and b) deep mines.	123
F.3	Profiles of change in mean potential temperature from the surface ($\overline{\Theta}$) outside (P3 to P10) and inside (P11 to P13) the mine for different thermal stability cases and topographies; a) shallow and b) deep mines.	124
F.4	Profiles of normalized mean mixing ratio (\overline{S}) outside (P3 to P10) and inside (P11 to P13) the mine for different thermal stability cases and topographies; a) shallow and b) deep mines.	125
F.5	Profiles of normalized turbulent sensible kinematic vertical heat flux ($\overline{w\theta}$) outside (P3 to P10) and inside (P11 to P13) the mine for different thermal stability cases and topographies; a) shallow and b) deep mines.	126
F.6	Profiles of the normalized resolved TKE (k_{res}) outside (P3 to P10) and inside (P11 to P13) the mine for different thermal stability cases and topographies; a) shallow and b) deep mines.	127
F.7	Profiles of the normalized sub-grid TKE (k_{sgs}) outside (P3 to P10) and inside (P11 to P13) the mine for different thermal stability cases and topographies; a) shallow and b) deep mines.	128
F.8	Profiles of the normalized total TKE ($k_{tot} = k_{res} + k_{sgs}$) outside (P3 to P10) and inside (P11 to P13) the mine for different thermal stability cases and topographies; a) shallow and b) deep mines.	129

F.9	Profiles of normalized advective plus turbulent flux of passive scalar in the x -direction ($\overline{US} + \overline{us}$) outside (P3 to P10) and inside (P11 to P13) the mine for different thermal stability cases and topographies; a) shallow and b) deep mines.	130
F.10	Profiles of normalized advective plus turbulent flux in the z -direction ($\overline{WS} + \overline{ws}$) outside (P3 to P10) and inside (P11 to P13) the mine for different thermal stability cases and topographies; a) shallow and b) deep mines.	131

List of Abbreviations

ABL	Atmospheric Boundary Layer
bLS	backward Lagrangian Stochastic
CALMET	CALifornia METeorological model
CALPUFF	CALifornia PUFF Model
CFD	Computational Fluid Dynamics
CFD-LS	Computational Fluid Dynamics-Lagrangian Stochastic
DES	Detached Eddy Simulation
DNS	Direct Numerical Simulations
EC	Eddy Covariance
FC	Flux Chamber
FG	Flux Gradient
GHG	GreenHouse Gas
GPM	Gaussian Plume Model
IDM	Inverse Dispersion Modeling
LES	Large-Eddy Simulation
LIDAR	LIght Detection And Ranging
LS	Lagrangian Stochastic
LTNE	Local Thermal Non-Equilibrium
MAE	Mean Absolute Error
MM5	Fifth-Generation Penn State/NCAR Mesoscale Model
MMD	Micro-meteorological Mass Difference
MOST	Monin-Obukhov Similarity Theory

OpenFOAM	Open Fields Operations And Manipulation
PIV	Particle Image Velocimetry
POD	Proper Orthogonal Decomposition
POP	Persistent Organic Pollutants
RANS	Reynolds-Averaged Navier-Stocks
RMSE	Root Mean Square Error
SGS	Sub-Grid Scale
SODAR	SONice Detection And Ranging
TAB	Tethered Air Blimp
TANAB	Tethered And Navigated Air Blimp
TKE	Turbulence Kinetic Energy
VLES	Very Large-Eddy Simulation
WRF	Weather Research and Forecasting

List of Mathematical Symbols

Latin Symbols

a_σ	Length-scale constant [-]
a_τ	Time-scale constant [-]
B	Buoyant production [$\text{m}^2 \text{s}^{-3}$]
b_u	Constant for surface-layer scaling in the x direction [-]
b_v	Constant for surface-layer scaling in the y direction [-]
b_w	Constant for surface-layer scaling in the z direction [-]
C	Gas concentration [$\mu\text{g m}^{-3}$]
C_Δ	LES filter size parameter [-]
C_μ	TKE model constant [-]
C_k	TKE model constant [-]
C_b	Background gas concentration [$\mu\text{g m}^{-3}$]
Co	Courant number [-]
d_a	Distance from the puff center to the receptor in the along-wind direction [m]
d_c	Distance from the puff center to the receptor in the cross-wind direction [m]
Δx	Grid spacing in the x direction [m]
Δy	Grid spacing in the y direction [m]
Δz	Grid spacing in the z direction [m]
g	Gravitational acceleration [m s^{-2}]
H	Effective height above the ground of the puff center [m]
h	Mixed-layer height [m]
i	Index [-]

$I_u(z)$	Turbulence intensity as a function of height z [-]
k_{res}	Resolved component of TKE [$\text{m}^2 \text{s}^{-2}$]
k_{sgs}	SGS component of TKE [$\text{m}^2 \text{s}^{-2}$]
k_{tot}	Total TKE [$\text{m}^2 \text{s}^{-2}$]
K_c	Eddy diffusivity [$\text{m}^2 \text{s}^{-1}$]
ℓ_0	Largest eddy size in the VLES model [m]
L	Obukhov length [m]
l	SGS mixing length [m]
L_{res}	Resolved Obukhov length [m]
L_y	Inlet height in the VLES model [m]
L_z	Inlet width in the VLES model [m]
\mathbf{m}	Unit vector along the streamwise direction [-]
N	Number of vortices [-]
\overline{P}_*	Resolved-scale static kinematic pressure [$\text{m}^2 \text{s}^{-2}$]
P	Shear production [$\text{m}^2 \text{s}^{-3}$]
Pr	Prandtl number [-]
Pr_T	Turbulent Prandtl number [-]
Q	Emission rate [kg s^{-1}]
R	Radius of influence [km]
Re	Reynolds number [-]
Re_T	SGS model turbulence Reynolds number [-]
Ri_b	Bulk Richardson number [-]
$RMAX$	Maximum radius of influence [km]
\overline{S}	Mean passive scalar [-]
s	Deviation of passive scalar from the mean value due to turbulent fluctuations [-]
\overline{S}_{ij}	Strain rate [s^{-1}]
Sc	Schmidt number [-]
Sc_T	Turbulent Schmidt number [-]
T_L	Effective Lagrangian timescale [s]

TI	Turbulence intensity [-]
\mathbf{u}	Velocity perturbation [m s^{-1}]
u	Deviation of velocity from the mean value due to turbulent fluctuations in the x direction
u_*	Friction velocity [m s^{-1}]
u_{*res}	Resolved friction velocity [m s^{-1}]
\bar{U}	Mean flow velocity in the x direction [m s^{-1}]
U^+	Non-dimensional mean horizontal velocity [-]
U_{ref}	Reference velocity [m s^{-1}]
v	Deviation of velocity from the mean value due to turbulent fluctuations in the y direction [m s^{-1}]
\bar{V}	Mean flow velocity in the y direction [m s^{-1}]
w	Deviation of velocity from the mean value due to turbulent fluctuations in the z direction [m s^{-1}]
$w_{*,res}$	Convective velocity scale (Deardorff velocity) [m s^{-1}]
\bar{W}	Mean flow velocity in the z direction [m s^{-1}]
\mathbf{x}	Position vector [m]
\mathbf{x}_i	Position vector for the center of the current vortex [m]
z^+	Non-dimensional wall-normal distance [-]
z_{ref}	Reference height [m]
z_0	Characteristic aerodynamic roughness length of the surface [m]

Greek Symbols

α	Power law exponent parameterized as a function of aerodynamic roughness length [-]
β	Vertical term of the Gaussian plume equation [m^{-1}]
Γ_i	Circulation for the current vortex [$\text{m}^2 \text{s}^{-1}$]
δ_{ij}	Kronecker-delta function [-]
Δ	Grid spacing [m]
ϵ	Dissipation rate [$\text{m}^2 \text{s}^{-3}$]

θ	Deviation of potential temperature from the mean value due to turbulent fluctuations [K]
$\bar{\Theta}$	Mean potential temperature [K]
Θ^+	Normalized temperature near the wall [-]
κ	von Kármán constant [-]
κ_θ	Thermal von Kármán constant [-]
ν	Kinematic viscosity [$\text{m}^2 \text{s}^{-1}$]
ν_T	Turbulent viscosity [$\text{m}^2 \text{s}^{-1}$]
π_i	SGS kinematic heat flux [$\text{m s}^{-1} \text{K}$]
σ_{max}	Size of the largest energy-containing vortices in the VLES model [m]
σ_u	x -component of velocity vector standard deviation [m s^{-1}]
σ_v	y -component of velocity vector standard deviation [m s^{-1}]
σ_w	z -component of velocity vector standard deviation [m s^{-1}]
σ_i	Characteristic length for the radius of current vortex [m]
σ_i	SGS passive scalar flux [m s^{-1}]
σ_x	Standard deviations of the Gaussian distribution in the along-wind direction [m]
σ_y	Standard deviations of the Gaussian distribution in the cross-wind direction [m]
σ_z	Standard deviations of the Gaussian distribution in the vertical direction [m]
τ	Time-scale for all energy-containing eddies in the VLES model [s]
τ_{ij}	SGS momentum flux [$\text{m}^2 \text{s}^{-2}$]
τ_0	Characteristic life time for the largest energy-containing eddies in the flow in the VLES model [s]

Chapter 1

Introduction

The extraction of minerals from an open-pit in the ground is a surface mining procedure called open-pit mining. The surface mining technique can be used when minerals or ore deposits are close to the surface of the earth (up to 1 [km]-depth). Mining activities often create large fugitive dust and GreenHouse Gases (GHGs) from the extraction, so it is crucial to understand atmospheric transport processes inside and near open-pit mines carefully. The open-pit mine is completely different from the usually studied valleys formed from fluvial or glacial activity. Air circulations, shear layers, and meandering can be created as a result of the existence of an open-pit terrain [127]. The ventilation of air within an open-pit depends on the wind flow characteristics induced by the mine pit and meteorological conditions [16, 39, 127]. Many studies measured and analyzed the amount of dust, volatile organic compounds, GHGs, and polycyclic aromatic compounds released from open pits [13, 46, 65, 76, 80, 97, 107, 116].

Natural topographical examples similar to the depression of an open-pit mine are the Arizona's Meteor Crater [73, 141], Peter Sinks in Utah [26], and the Gruenloch doline in Austria [140], all of which have been investigated in detail. Meteorological characteristics of such depressions are different from those of homogeneous flat terrain and valleys. For example, a temperature-stratified, quiescent, and cool pool of air forms at the bottom of such depressions under thermally-stable conditions during the night [26, 73, 140, 141]. In comparison to flat terrain and valleys, the meteorological features inside the depression exhibit reduced slope flows, reduced advective transfer with air outside of the depression, reduced turbulent sensible heat flux with the bottom surface of the depression, change of wind direction from the cool pool to altitudes outside the depression, and formation of weak and intermittent turbulent jets on the depression walls near the ground [26, 140]. Also, standing

waves or oscillating temperature fields have been observed in such depressions, and the temperature stratification is noted to disintegrate under high wind conditions [73, 141]. The meteorological conditions of such depressions are understood to be influenced by synoptic events, the seasonal weather variation, topography, and radiative heat transfer between the depression and the sky, which is a function of depression aspect ratio [26, 140]. It is informative to study if open-pit mines exhibit similar meteorological conditions, particularly given the confounding influence of nearby industrial operations.

Most oil sand mines are categorized as shallow open-pit mines of less than 100-m depth. Deep open-pit mines can be used in coal mining and hard rock mining for ores such as copper, gold, iron, aluminum, and many other minerals. These kinds of mines are mostly deeper than oil sand mines with more than a few hundred meters in depth. To prevent and minimize damage and danger from rock falls, the walls of the pit are generally dug on an angle less than vertical. This design angle depends on how weathered the rocks are, the type of rock, and also how many structural weaknesses occur within the rocks, such as faults, shears, joints, or foliations. At the side of the pit, a haul road is situated, forming a ramp to let trucks drive, carrying ore and waste rock.

While the structure of the Atmospheric Boundary Layer (ABL) in orographically complex terrain can be complicated [21, 68, 87, 88, 95–97, 117], there are few comprehensive field studies that focus on the ABL over an open-pit mine environment. Much of the understanding of the wind flow and atmospheric transport of material from those pits is through modelling efforts. An important practical application of atmospheric models is in helping quantify gas or particulate emission rates from the fugitive sources. Such quantifications may be needed to meet regulatory requirements, understand the management and mitigation of emissions, and prioritize emissions mitigation efforts. Quantifying emissions from open-pit mines is a serious challenge for traditional measurement techniques. In the following sections the methods of quantifying area-fugitive emissions from complex terrain related to open-pit mines are described. First, the simple methods of emission measurements is explained, and after that the methods with high spatiotemporal resolution modelling are introduced. Finally, the Inverse Dispersion Modelling (IDM) paradigm is described.

1.1 Methods of Quantifying Area-fugitive Emissions from Complex Terrains

Estimations of fugitive emissions from large area sources such as tailings ponds and open-pit mine faces are characterized by a large amount of uncertainty, which is amplified for the mining industry when different methods, area delineations, and procedures are applied. The Flux Chamber (FC), Eddy Covariance (EC), and Flux Gradient (FG) are the main simple measurement techniques, while the high resolution modelling methods, such as the prognostic Computational Fluid Dynamics (CFD) model, the diagnostic CALifornia PUFF model (CALPUFF) model, empowered by Lagrangian Stochastic (LS) and Inverse Dispersion Modelling (IDM) techniques, provide the well-known and more accurate methods of emission quantification.

1.1.1 Flux Chamber, Eddy Covariance, and Flux Gradient Paradigms

The Flux Chamber (FC) (Figure 1.1) technique is a simple but intrusive method for area-fugitive emission flux quantification for complex terrains, which does not require expansive expertise and equipment, while it provides relatively easy and rapid measurements. FCs have a central role in the measurement of emissions but there are challenges with this method. FCs modify the environment within the measurement chamber, which can alter the ambient emission rate. They have a small measurement footprint, and this may require an extensive sampling survey to quantify a large source accurately. Therefore, they are not suited for continuous measurements [10, 115].

Non-intrusive and continuous micro-meteorological methods of determining area-fugitive emission fluxes are Eddy Covariance (EC) [40] (Figure 1.2) and Flux Gradient (FG) [90] techniques that can be used to measure fluxes from complex terrains. These methods intrinsically produce integrated flux estimates representative of hectares to square kilometers of land. The EC technique is a non-interference technique that does not disrupt the surface being measured, nor does it modify the transport processes at the source. The EC technique may not be appropriate for measurements of emission out of open-pits as this technique is not suitable for sites with a high degree of spatial heterogeneity which complicates analysis (i.e. interpreting the measurement footprint in relation to spatial emission variability). Also, it is possible that the complex wind-flow over complex terrains invalidate the EC technique for measurements [40, 151]. The FG estimates of emission flux are based on relationships



Figure 1.1: A flux chamber used to measure GHG emissions from a tailings pond in an open-pit mining facility; photo courtesy of Dr. Thomas Flesch.

between the vertical gradient of pollutant mixing ratio and the associated flux. In the atmosphere, turbulent exchange dominates molecular diffusion by several orders of magnitude under most conditions, and the factor relating the gradient to the flux is a transfer coefficient dependent on the characteristics of turbulence, called the eddy diffusivity (K_c [$\text{m}^2 \text{s}^{-1}$]) [131]. For FG measurements, the effective footprint is the same as the EC footprint at the geometric mean of the two sampling heights [56] for a homogeneous surface area.

The comparison of the mentioned techniques were investigated by You et al. (2021a and 2021b) [150, 151] while applied to area-fugitive GHG emissions from a tailings pond. They showed that flux chambers underestimated the fluxes. Also, their results showed that larger footprints together with high spatiotemporal resolution of micro-meteorological flux measurement methods (EC and FG) may result in more robust estimates of GHG emissions. The summary of reviewed studies on quantifying the emissions with the FC, EC, and FG methods are presented in Table A.1.



Figure 1.2: An eddy covariance sensor used to measure GHG emissions from an open-pit mining facility; photo courtesy of Dr. Thomas Flesch.

1.1.2 Methods Employing High Spatiotemporal Resolution Modeling

Methods based on high spatiotemporal resolution modeling consider atmospheric transport phenomena on a latitude and longitude grid of the earth surface over time, unlike the previous section that introduced methods focusing on point or line measurements. Techniques based on high spatiotemporal resolution modeling can be broadly categorized as prognostic models, diagnostic models, or hybrid models. Prognostic models solve transport questions at a fundamental level, but they are computationally inefficient, while diagnostic models rely on empirical formulations to simulate transport phenomena more computationally efficiently at the cost of reduced accuracy. Hybrid models mix the two paradigms to improve computational efficiency and accuracy simultaneously. Related to high spatiotemporal resolution modeling approaches are the Lagrangian Stochastic (LS) and Inverse Dispersion Modelling (IDM) techniques, all of which will be reviewed in the following subsections.

1.1.2.1 Monin-Obukhov Similarity Theory (MOST)

The foundation for many methods is the surface layer theory. In the atmospheric sciences, the determination of regional-scale surface fluxes of momentum, sensible heat, and latent heat over complex terrain is a basic challenge. Monin-Obukhov Similarity Theory (MOST) [91] is the main practical model for the computation of these fluxes using measurements in the atmospheric surface layer [103]. MOST is developed for homogeneous surfaces, but it has been applied for heterogeneous surfaces as well. The applicability of this similarity theory over heterogeneous surfaces has been justified due to the strong mixing effects of atmospheric turbulence in such cases [20]. Panofsky and Dutton (1984) [101] presented a full description and assumptions of the ABL and MOST, and the applications of MOST on wind flow over complex terrains were reviewed by Breedt et al. (2018) [18] and Han et al. (2020) [50].

1.1.2.2 Prognostic Modelling

The prediction of wind field over complex terrains, such as an open-pit mine are usually based on the numerical solution of the Navier-Stokes transport equations and a turbulence model in a domain that includes the local terrain [69]. In the 1990s and early 2000s Baklanov (1995 and 2000) [11, 12] was the first to propose the need to approach the atmospheric transport problem over open-pit mines from a multi-physics perspective, highlighting the combination of scales involved and the importance of topography. The limitation of the availability of observation platforms and the difficulty in acquiring data from complex environments have resulted in atmospheric turbulence studies to only focus on relatively smooth terrain and horizontally homogeneous environments [7, 51, 64, 86]. However, the study of the ABL and surface-atmosphere interaction over complex terrain is significant for many applications. Horizontal gradients of momentum or temperature can be formed by surface heterogeneity, which influence or complicate the horizontal and vertical transport mechanisms, for instance by slope flows or thermals [83, 87, 95]. The established model parameterizations of turbulent processes for atmospheric flows over smooth and homogeneous surfaces often fail to be applied over complex terrain successfully [118].

Numerical simulation technology is increasingly being employed to give advanced warning of potential air quality problems as a result of open-pit mining emissions in addition to providing a basis for future planning of activities. The initial entrainment and subsequent dispersion of fugitive dust and other pollutants present a process complicated by the combination of the in-pit topography, the surrounding natural topography, and the dynamic

nature of emissions from these sites [127].

There is growing interest in applying Computational Fluid Dynamics (CFD) to simulate complex micro-meteorological processes inside and around open-pit mines. In general, the problem can be described in terms of the interaction, within the ABL, between the atmosphere and the objects that define the complex surface geometry [38]. In high-resolution numerical modeling, equations of the transportation of mass, momentum, energy, and atmospheric species are solved to predict the future time evolution of the atmosphere or alternatively reconstruct a past state of the atmosphere at high resolution for detailed investigation of transport phenomena. The computational cost of CFD is dropping as a result of the increasing speed of computers, so the amount of physical experimentation can be reduced considerably by running CFD models instead. Not only can CFD be used to conduct virtual experiments, it can also be used to design physical experiments better with increased efficiency [148].

While Direct Numerical Simulations (DNS) are too computationally expensive, and Reynolds-Averaged Navier-Stokes (RANS) or eddy viscosity models suffer from lack of accuracy, Large-Eddy Simulations (LES) have been used as a useful alternative numerical tool to simulate the ABL with sufficient reliability [7]. In LES, the turbulent eddies of the size of the computational grid cells and larger are explicitly resolved, while the effects of the smaller eddies on the large ones and the mean flow field are parameterized using Sub-Grid Scale (SGS) models [71]. LES is able to simulate explicitly the complex flows and turbulence structures in the atmospheric boundary layer in a transient manner. Its results can be used to complement field measurements and laboratory observations in order to enrich the fundamental understanding of atmospheric transport processes [24]. In low-Reynolds number or highly thermally-stable flows, LES can predict the unsteady variation in flow and concentration fields more accurately than RANS models [81]. This superiority stems from the fact that LES resolves large scales of turbulence that may be the driving forces for pollutant dispersion. Therefore, it can provide reliable results in a wider range of flows and applications. Complex terrains with topographical changes may induce slope flows, flow separations, and re-circulations, which can be simulated more successfully using the LES method [39]. In addition to the numerical techniques used in hybrid LES methods, Very Large-Eddy Simulation (VLES) is another powerful tool to economize the CFD simulations. The concept of VLES, originally proposed by Speziale (1998) [130] is one of the earliest hybrid CFD methods. The main distinction between VLES and the standard LES is the determination of filter width with respect to the grid size. In pure LES, the filter width is

associated with the grid size, while the filter width in VLES can be set arbitrarily at any value between the grid size and the large characteristic length-scales of the flow [72, 133]. Increasing the filter width will reduce the computational cost of the model at the cost of accuracy. Based on this definition, the VLES becomes LES when the filter width is set as its lowest limit of grid size. Pope (2000) [106] proposed a numerical definition for the distinction between LES and VLES. According to Pope (2000) [106], an LES with a sufficiently fine grid and filter length should resolve more than 80% of the Turbulence Kinetic Energy (TKE) everywhere in the domain except near-wall regions where wall treatments may be used. In contrast, the VLES is defined as a method with coarse grid size and filter length that would resolve possibly less than 80% of the TKE in the domain.

The airflow over complex terrains such as mountains, valleys, and cavities have been studied to investigate the processes of natural ventilation. Baklanov (1995) [11] developed a numerical spatial model of turbulent dynamics of the atmosphere over complex topography to perform atmospheric transport simulations over an open pit area using LES with an SGS model closure of Smagorinsky-Deardorff. The study aimed to demonstrate the wind flow and the open-pit-atmosphere interaction under various thermal stability conditions. The study predicted formation of tear-off currents, circulation zones, and thermals. In another study, Brés and Colonius (2008) [19] characterized two- and three-dimensional global instabilities of compressible flow over open cavities using a DNS method. They considered cavities that were homogeneous in the span-wise direction. Their results indicated that the instabilities were hydrodynamic (rather than acoustic) in nature and arose from a generic centrifugal instability mechanism associated with the mean recirculating vortical flow in the downstream part of the cavity. Kang and Sung (2009) [63] performed Particle Image Velocimetry (PIV) measurements and Proper Orthogonal Decomposition (POD) analysis in turbulent flows over a laboratory-scale open cavity to characterize large-scale vortical structures responsible for self-sustained oscillations. Goreishi-Madiseh et al. (2017) [43] developed a three-dimensional unsteady Local Thermal Non-Equilibrium (LTNE) CFD model to evaluate thermal storage and heat transfer between ventilation air and a rock pit. Their results suggested that the seasonal thermal energy storage of the rock pit could assist thermal management in an underground mine and could reduce energy consumption for winter heating and summer cooling. Shi et al. (2000) [126] used a high-resolution three-dimensional non-hydrostatic CFD model to simulate the air circulation inside a 2-km wide and 100-m deep open-pit mine. They were able to predict the air circulation inside the cavity, which was responsible for the dilution of pollutants inside the pit. Their results showed that both mechanical and thermal

forcing were important mechanisms controlling the evolution of the atmosphere inside the pit. Silvester et al. (2009) [127] used a CFD code based on the standard $k - \epsilon$ RANS turbulence model to study the mechanically-forced circulations developed inside the Old Moor open-pit (1-km wide and 650-m deep). They showed that the interaction of the wind sweeping over the cavity and the internal atmosphere caused strong mechanical shear near the top of the pit. Choudhury and Bandopadhyay (2016) [25] applied a three-dimensional numerical simulation to model the flow of air and the transport of gaseous pollutants in an Arctic open-pit mine and investigated the effects of low and high wind speeds on the pollutants' profiles in the mine. They showed that while higher velocities of air could remove the pollutants from the pit bottom, they could not remove pollutants from the pit entirely and necessitated artificial mitigation measures.

In general, most CFD studies have considered the case of a thermally-neutral (not vertically stratified) ambient atmosphere. However, thermal stability has been seen to have a strong influence over flow features in complex topography. Bhowmick (2015) [15] used CFD to estimate the fugitive dust retention in two idealized open-pit domains for various weather conditions in a clear sky. The domains were simulated for both summer and winter weather conditions in a high-latitude Arctic and a sub-Arctic open-pit mine. The RANS method with a standard $k - \epsilon$ turbulence model was used to simulate the fugitive dust transport in the pits. The results showed that the combined effect of mechanical and thermal (surface heat flux) forcing during summer conditions cleared the fugitive dust from the open-pit mine within one hour. However, in winter, the negative heat flux from the pit surface often lead to an atmospheric inversion in the open-pit domain, which resulted in extensive retention of fugitive dust for a prolonged duration. Tukkaraja et al. (2016) [136] simulated the air temperature inversion conditions in a hypothetical open-pit mine using CFD with a RANS method based on the $k - \epsilon$ turbulence model and investigated the effect of the temperature inversion on the dispersion of gas and dust particles in the pit. They showed that the gas and dust particles were trapped inside the pit under inversion conditions, while they were dispersed in the absence of inversion. Joseph et al. (2018) [61] studied two distinct open-pit mines for an artificial and an actual terrain using CFD. They presented an evaluation of a buoyancy-modified $k - \epsilon$ dust dispersion model for predicting fugitive dust deposition from a surface quarry. The dust clouds were modeled as volumetric emission, and their dispersion were simulated by coupling the flow field with stochastic tracking of the particulates. They concluded that 1) the in-pit deposition is underestimated without a realistic flow field, 2) CFD models of thermally-neutral condition are not sufficient, requiring analysis of thermally-

unstable and stable conditions, and 3) in-pit topography and surrounding terrain must be considered.

Some studies simulated the idealized terrain to show the advantages and disadvantages of simplified geometry. The LES method by Bhowmick et al. (2015) [15] showed that the idealized pits had several advantages over the actual pits: idealized domains contained no faceted topography due to simplified geometry; mesh quality in numerical simulations was better due to the absence of vertices and ridges; acceptable resolution in the solution could be achieved with higher grid density compared to an actual pit domain due to a planar pit surface; less number of mesh elements were needed; and statistically-stationary flow conditions were reached more quickly than the simulation for the actual pit. Flores et al. (2014) [39] performed a Detached Eddy Simulation (DES), which combines the LES in the domain interior, to resolve large atmospheric eddies, with the RANS method near walls, to model transport phenomena near walls, using the Open Fields Operations And Manipulation (OpenFOAM) CFD simulation package to simulate and predict particle dispersion in an idealized mine and an actual open-pit mine in Chile. The idealized pit, which was a simplified topography, retained the same general dimensions of the Chuquicamata copper mine, but it represented the pit as an inverted truncated cone with a superior diameter of 4 km, an interior diameter of 1 km, and a depth of 1 km. The simulations were performed for three different conditions: 1) thermally-neutral condition: air advection with mean wind speed of 10 [m s^{-1}] driving mechanical turbulence under isothermal conditions; 2) thermal buoyancy-driven condition: air advection with mean wind speed of 1 [m s^{-1}] driving mechanical turbulence with surface vertical sensible heat flux of 240 [W m^{-2}] driving thermal buoyancy; and 3) thermally-unstable condition: both air advection (10 [m s^{-1}]) and surface heat flux (240 [W m^{-2}]) being considered. The results showed that the buoyant currents contributed to the removal of a large percentage of the particles. The summary of reviewed studies of CFD simulations over simple and complex terrains are presented in Table B.1.

1.1.2.3 Diagnostic and Hybrid Modelling

As far as diagnostic models are concerned, the CALifornia PUFF (CALPUFF) model is an industry standard. CALPUFF is a multilayer, multi-species, and non-steady-state puff dispersion model, that simulates the effects of time- and space-varying meteorological conditions on pollution transport [123]. CALPUFF's meteorological pre-processor is the CALifornia Meteorological (CALMET) model, which is a meteorological model that calculates hourly wind and temperature fields on a three-dimensional gridded modeling domain using interpolation

and extrapolation techniques. Associated fields, such as the mixing height, surface characteristics, and dispersion properties, are also calculated by CALMET. CALPUFF's transport, dispersion, and transformation calculations typically use either the three-dimensional fields generated by CALMET, or they use alternatively non-gridded meteorological data in simpler dispersion models [123].

Numerous studies have investigated the performance of diagnostic and hybrid models, which will be reviewed here. Li and Guo (2006) [78] performed three-dimensional CFD dispersion and CALPUFF simulations to track odor dispersion from a 3000-sow farrowing farm under different thermal stability conditions. They used vertical profiles of wind and temperature in ABL for CFD simulations and evaluated their effects on odor dispersion. A flat terrain and un-irrigated agricultural land with 0.1 [m] ground roughness was defined in the CALPUFF model. Their results of both models showed that detectable odor traveled farther under stable conditions than under unstable conditions with the same wind speed. Under the same atmospheric stability conditions, odor concentrations were found to be higher at lower wind speed than that at greater wind speed. Also, they showed that stronger odor concentration and longer detectable travel distance were favored with stable atmospheric conditions and lower wind speed. Comparing the CFD and CALPUFF simulations showed that odor concentration predicted by the CFD model were higher than those predicted by the CALPUFF model in short distances (less than 300 [m]).

Arregocés et al. (2016) [8] evaluated the impacts of an open-pit coal mine located in the north of Colombia on the dispersion and transport of PM_{10} due to the emissions from the mining activities. CALPUFF was used to perform the simulation, and it was validated with the environmental concentration data of PM_{10} from 5 receivers. They used a concept of intake fraction, which is defined as the fraction of material or its precursor released from a source that is finally inhaled or ingested by a population. The surface meteorological data were obtained from six stations located within the domain area with hourly time resolution. The results showed that the terrain effect on wind speed and direction were notable. Also, their simulations demonstrated that a significant portion of intake fraction occurred beyond 45 [km] from the source, emphasizing the need for detailed long-range dispersion modeling.

The ability of the CALPUFF model to simulate dry and wet deposition processes up to 1000 [km] from the source was evaluated by Giaiotti et al. (2018) [44] in the specific case of radionuclides released in the atmosphere, during the 1986 Chernobyl Nuclear Power Plant accident. 211 surface stations, 194 precipitation stations, and 14 upper air stations were imported as meteorological input for feeding the CALMET pre-processor. The results show

smoother contamination pattern than the reality because of fine structure of the depositions. The results show that the predicted contamination pattern depends strongly on the source term employed in the simulation.

Chang et al. (2003) [23] evaluated CALPUFF using different kinds of emission sources involving instantaneous release of sulfur hexafluoride tracer gas in a mesoscale region with desert basins and mountains. Networks of surface wind observations and special radiosonde and pilot balloon soundings were available to compare the model results and the observations. They showed that CALMET and CALPUFF can predict the wind field and plume in the horizontal direction better than vertical direction.

Cui et al. (2020) [28] performed a field campaign consisting of ABL observations and tracer experiments in a hilly region of the Gobi Desert in northwest China. They have also executed the CALMET and CALPUFF models to predict the wind field and tracer dispersion. The CALMET model showed thermal heterogeneity to some extent in the temperature fields and mixing height distributions and large deviations in the friction velocity between the model and observations. The comparison of the CALPUFF model with the tracer measurements indicated that under the condition of low topographic influence, the predictions of CALPUFF are in good agreement with the measurements for the near distance, but in the far distance because of wind shears and vertical thermal discontinuity, a general tendency toward under-prediction of the concentration was observed.

Wang et al. (2008) [139] evaluated the performance of CALMET in terms of simulating winds, for lake breeze events, that were highly variable in space and time. In their work, the reference winds were generated by the Fifth-Generation Penn State/NCAR Mesoscale Model (MM5) assimilating system and compared to the results of CALMET. They conducted statistical evaluations to quantify overall model differences in wind speed and direction over the domain. They showed that below 850 [m] above the surface, relative differences in wind speed were about 25 to 40 % (layer averaged) and the differences became larger because of the limited number of upper-air stations near the studied domain. Their analyses implied that model differences were dependent on time because of time-dependent spatial variability in winds.

Cox et al. (2005) [27] performed a study to assess the performance of three diagnostic wind models (CALMET, MCSCIPUF, and SWIFT) by direct comparison against wind field data. Their results showed that the models appear to have nearly equal ability to produce valid horizontal winds and all models performed the best during non-stable times, as would be expected when more mixing is present.

Ruggeri et al. (2020) [119] used a CALMET/CALPUFF modeling system to estimate airborne levels of Persistent Organic Pollutants (POPs) in a medium-sized urban area. To develop the required spatial and temporal resolution of temperature and wind profiles, the Weather Research and Forecasting (WRF) model was used as the initial estimate for CALMET to obtain the 3D wind field covering the modeling domain and period. Results exhibited that the WRF/CALMET/CALPUFF modeling system predicts POPs airborne concentrations with reasonable accuracy at a local scale. Source apportionment showed the prevalence of emissions from open burning of municipal solid waste on the simulated atmospheric concentrations. The spatial pattern obtained from simulations exhibited that the lowest or highest levels predicted by the model occurred in areas where no samples were taken, suggesting that the real gradient in the POPs air concentrations would be much greater. They showed the usefulness of the implementation of an atmospheric dispersion model, not only in the study of air quality and exposure levels, but also as a tool for the proper design of monitoring networks.

In another study, Tang et al. (2021) [132] combined the WRF data and CALMET to investigate the impact of horizontal resolution on the simulated near-surface wind fields of Super Typhoon Meranti (2016). As indicated by the reasonably large correlation coefficient (> 0.4) between the simulated and observed winds, the performance of the WRF/CALMET-coupled system was generally satisfactory. The simulation results appeared to improve slightly but continuously with higher horizontal resolution. The summary of reviewed studies of CALMET/CALPUFF simulations over simple and complex terrains are presented in Table C.1.

1.1.2.4 Lagrangian Stochastic Modelling

Both prognostic and diagnostic models have been empowered by the Lagrangian Stochastic (LS) dispersion modeling paradigm. The LS paradigm has been specifically developed to simulate atmospheric dispersion of pollutants in complex turbulent flows where other techniques such as similarity theory and gradient-transfer theory are in principle not valid [142, 143]. The unique feature of the LS paradigm is its ability to conserve the mass of transported atmospheric pollutants. LS models simulate the atmospheric dispersion by tracking the turbulent motions of individually-labeled fluid elements or particles [82]. A forward LS model mimics the trajectories of thousands of tracer particles as they travel downwind of a source, and it is the most natural means of modeling dispersion in the atmospheric boundary layer. Each trajectory is the summation of discrete changes in particle position and velocity

over time [145].

Raza et al. (2001) [112] performed meso-scale atmospheric dispersion and ground concentration calculations by using a fully three-dimensional LS particle trajectory model. They also used a Gaussian Plume Model (GPM) with Pasquill-Gifford's stability classes and investigated the effects of variation in release height on the ground concentration and dispersion parameters for continuous releases. The comparison of the results demonstrated a need for using a three-dimensional model over the simple GPM for meso-scale atmospheric dispersion applications. Their results showed that the GPM overpredicts the ground concentration because it cannot take into account the vertical wind shear. Also, they reported a weak dependence on the release height in the numerically-calculated dispersion coefficients.

Cassiani et al. (2015) [22] have developed an LS model with proposing a correction for the vertical gradient of air density incorporated into a skewed probability density function formulation for turbulence in the convective boundary layer and by replacing the zero mean fall speed of a tracer-particle with the terminal speed of the particle to expand the application of LS to predict spore and pollen dispersal by Reynolds (2018) [114].

A single particle LS model has been developed and applied by Ferrero and Maccarini (2021) [32] with the purpose of simulating the concentration fluctuations in dispersion. Their model treats concentration variance as a quantity whose motion is driven by an advection-diffusion process and they vary the coefficients of the turbulence parameterization to match the small-scale turbulence. The results showed that the parameterization for the variance dissipation time-scale, tested in neutral conditions, can be used also in stable and unstable conditions and in low-wind speed conditions.

Fattal et al. (2021) [30] simulated the accumulated particulate matter concentration at a given vertical column due to traffic sources in an urban area. They presented a mass-consistent urban LS model for pollutant dispersion, where the flow field was modeled using a hybrid approach. They modelled the surface layer based on the typical turbulent scales in both of the canopy and inertial sub-layers. They proposed an efficient methodology, using a footprint analysis based on backward LS modeling as well as merging the traffic routes into area source cells. They demonstrated the positive effect of urban green space on the reduction of concentration profiles. Table D.1 provides a summary of studies focused on the LS paradigm.

1.1.2.5 The Inverse Dispersion Modelling Paradigm

Another emission quantification paradigm is Inverse Dispersion Modeling (IDM) (Figure 1.3), which is a flexible technique, adaptable to many methods discussed earlier. The main idea in IDM is to establish a relationship between concentration measurements downwind of a source of emission and the strength of the emission source [124]. If this relationship is known as a function of meteorological conditions and the specific site parameters, then the strength of the emission source can be determined by measuring the concentration downwind. IDM requires a dispersion model to establish this relationship. The IDM technique is capable of continuous and long-term emission measurements. By considering a source of pollutants, which is emitting gas to the atmosphere at an unknown rate Q [kg s^{-1}], the average gas concentration would be C [$\mu\text{g m}^{-3}$] downwind of the source, which will be enhanced above the upwind background concentration level C_b [$\mu\text{g m}^{-3}$]. The concentration increase is proportional to Q [kg s^{-1}], and a measurement of $(C - C_b)$ [$\mu\text{g m}^{-3}$] indicates Q [kg s^{-1}]. The link between Q [kg s^{-1}] and $(C - C_b)$ [$\mu\text{g m}^{-3}$] is calculated with an atmospheric dispersion model that mathematically predicts how gases disperse in the atmosphere. Given a theoretical ratio $(C/Q)_{\text{Sim}}$, provided by an atmospheric dispersion model, one may write [35]

$$Q = \frac{(C - C_b)}{(C/Q)_{\text{Sim}}}. \quad (1.1)$$

IDM is only defined when it is associated with a specific dispersion model. Such models result from a variety of types such as Gaussian plume, K-theory, and LS. One of the challenges with IDM is choosing an appropriate dispersion model for a specific problem and understanding the strengths and weaknesses of that model. Dispersion models can be categorized by their spatial scale. Short-range models focus on gas dispersion within a few kilometers of an emission source where the attention is the atmospheric surface layer near the ground. Regional models have a broader focus in scale from 10 to 100 [km]. The larger the spatial scale of the model, the greater the spatial and temporal ranges of motions that must be accounted for. This increases 1) the complexity, 2) the number of model inputs, and 3) the uncertainty in the model predictions. In choosing a dispersion model for IDM some important questions to consider are as follows: 1) is the model relatively easy to use? 2) are model inputs directly measurable (e.g. avoiding subjective inputs such as fractional cloud cover)? 3) is there flexibility in handling arbitrarily shaped and sized emission sources? 4) does the model scale match the scale of the IDM problem? and 5) is there guidance on using

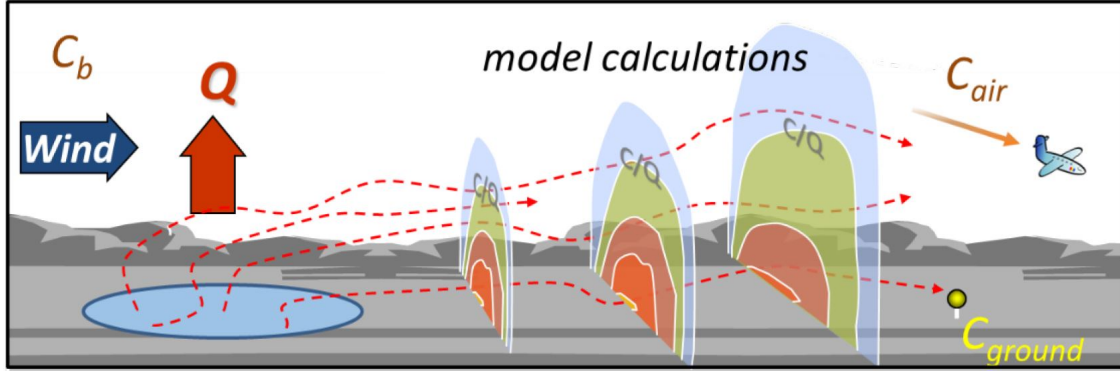


Figure 1.3: Illustration of an Inverse Dispersion Modelling (IDM) technique: 1) the source emits gas at a rate Q [kg s^{-1}]; 2) gas concentration C [$\mu\text{g m}^{-3}$] is measured downwind of the source (either near the ground or above the surface using air sampling); 3) a dispersion model predicts the normalized concentration C/Q_{sim} at the downwind location; 4) the emission rate Q [kg s^{-1}] is determined by dividing the measured C [$\mu\text{g m}^{-3}$] by the predicted C/Q_{sim} . For most gases a background concentration C_b [$\mu\text{g m}^{-3}$] needs to be subtracted from the observations; Figure courtesy of Dr. Thomas Flesch.

the model with IDM [143, 144]?

Most IDM applications to estimate industrial emissions are local in scale, with concentration sensors within a few kilometers of the source. In these situations, simple short-range dispersion models are appropriate for IDM calculations. Not all time periods are conducive to accurate dispersion model predictions, including light wind periods, periods of intense thermal stratification, or periods of rapid atmospheric changes (e.g., near sunrise or sunset). Recognizing these shortcomings, IDM procedures often include meteorological filtering criteria to eliminate error-prone periods from the analysis [33]. The use of different dispersion models in an IDM calculation will inevitably result in different emission estimates, even for well-accepted models using the same input data, and used with appropriate guidance. This inter-model variability is one of several sources of IDM uncertainty, such as assuming the source emission rate is spatially homogeneous, or that wind conditions are spatially homogeneous.

Numerous studies on applications of IDM to quantify area-fugitive emissions from complex terrain can be reviewed here. IDM has many possible implementations based on combinations of dispersion models and gas sensor types [36, 37]. A backward Lagrangian Stochastic (bLS) model provides an efficient method for calculating dispersion from area sources [37]. Flesch et al. (2005) [35] used the bLS model to diagnose gas emissions from a swine farm. The bLS model took as input the average wind velocity and direction, surface roughness,

and atmospheric stability parameter. They found that the complex terrains would make the simple bLS model less defensible, and proper measurement locations were less clear. Moreover, if other emission sources had surrounded the farm, it may become impossible to separate the farm tracer pollutant plume from a complex background pollutant plume.

In order to examine methodologies to quantify methane emissions from small surface sources, Gao et al. (2009) [41] performed a study to estimate methane emissions from a ground-level grid using a simplified Micro-meteorological Mass Difference (MMD) method and an IDM technique (bLS). Their results indicated that the simplified MMD and the bLS techniques provided equally-accurate measurements of source emission rates from the ensemble of release trials. However, compared to the MMD technique, which needs sensors at several heights, the IDM technique is preferable due to its simplicity; it can be used with measurements at just one height.

Hu et al. (2016) [57] performed an analysis of trace gas dispersion experiments with multiple point sources and line-averaging laser gas detectors on gently-rolling terrain to establish how well the emission rate can be inferred from IDM, using an LS wind transport model. They found that the unwanted impact of the terrain is adequately compensated by representing detector light paths as curves. Also, their results showed that the quality of the inversions is less sensitive to extremes of stratification than has been reported for other trials.

Liao et al. (2019) [79] examined the ability of an IDM technique, in combination with an open-path laser system, for measuring ammonia emissions from vegetable greenhouses. They found that determination of the area and height of the greenhouse emission sources are critical to emission rate estimates, while removing the periods with inaccurate wind simulations has minimal effect on the daily and total emission rate estimations since the omitted periods mainly occur during nighttime (low emission rate periods). The summary of reviewed studies of IDM simulations over simple and complex terrains are presented in Table E.1.

1.2 Research Gaps and Objectives

An in-depth understanding of gas and particulate transport from open-pit mines relies on the use of atmospheric models. However, atmospheric models are challenged by the topographic complexity of open-pit mines. While prognostic models provide an avenue for high fidelity modelling of terrain impacts, they are difficult and computationally expensive tools that

may not be broadly usable.

In the present work, first the focus is on the development of a CFD-LS model for wind flow and dispersion of area-fugitive gas pollutants for open-pit mines. In previous studies, the simulation of over-simplified open-pits (e.g. in the form of a cylinder or inverted cone) was conducted over shallow or deep mines, while more realistic mine geometries (e.g. kidney shape) and variation in mine depth were overlooked. Thermal stability conditions appear to play a significant role in forming flow fields and defining the complexity of the flow pattern inside and surrounding the pit. The neutral condition is studied in many works since wind and temperature field patterns are much easier to capture than thermally-unstable and stable conditions. The other thermal stability conditions have received less attention in the literature. A realistic kidney-shaped mine is used in this study, and both a shallow (100 [m]) and a deep (500 [m]) mine are considered. The CFD-LS model is used to simulate conditions where the ambient (upwind) flow is thermally-unstable, neutral, or stable. An important step in the model evaluation is the comparison of the modelled flow variables upwind to field data collected upwind of an actual open-pit mine.

In the second step, the capability of diagnostic models on open-pit mine ABL simulation is investigated. Diagnostic models like CALPUFF provide a much more practical tool for this purpose. However, the ability of diagnostic models to accurately represent the atmospheric transport phenomena above and surrounding open-pit mines is uncertain. Therefore, the objective of this study is to compare the prognostic and diagnostic paradigms. The results from the CALPUFF model are compared against the results of the high-resolution CFD-LS model using a variety of different CALPUFF setups. A key focus for the comparison is to assess how close the two models would predict the emission flux of GHGs release from the open-pit mines of shallow and deep configurations under different thermal stability conditions. The thesis is focused on the following questions:

- What are the effects of thermal stability conditions and mine depth on atmospheric transport phenomena over complex terrain?
- How do results from different implementations of CALPUFF compare to the CFD-LS simulations?
- Does the number and location of the input weather stations for CALPUFF influence the agreement with the CFD-LS simulations?
- Does the agreement between the CFD-LS and CALPUFF predictions of surface gas

concentrations downwind of the mine depend on location?

Finally, the results are also used to consider the prospects for an IDM calculation of gas emission rates from the mine pits. The IDM approach to quantifying emissions has many potential advantages compared with other methods, but it requires an accurate and practical means of calculating gas dispersion.

1.3 Structure of the Thesis

The thesis is organized as follows. Section 2 describes the methodology. Section 2.1 introduces the open-pit mine characteristics and the experimental instruments, which are deployed to collect a validation dataset. Details of the CFD model are presented in Section 2.2. The details of the LS and CALMET/CALPUFF models are presented in Sections 2.3 and 2.4, respectively. The statistical analysis for comparison of a model against a reference set of data is described in Section 2.5. In Section 3, the results and discussions are provided. Section 3.1 summarizes the results and discussions for the CFD model development and comparison against observations. Section 3.2 summarizes the results and discussions for the CALPUFF-CFD-LS model comparisons, and Section 3.3 provides the implications for the applicability of IDM using various dispersion modelling approaches. Finally, Section 4 offers the conclusions, limitations, and recommendations of this thesis.

Chapter 2

Methodology

In this chapter the methodology is developed in several parts. First, an example of an actual open-pit mine environment is provided, for which meteorological observations were also collected for the purpose of model evaluations. Next, the prognostic Computational Fluid Dynamics (CFD) model is developed, which is based on a Very Large-Eddy Simulation (VLES) method. Next, the Lagrangian Stochastic (LS) model is introduced, which is used for gas dispersion analysis in comparison to the diagnostic models. Next, the diagnostic CALifornia PUFF (CALPUFF) model is introduced. Finally, statistical metrics are defined for the purpose of comparing model results against a set of reference data. The summary of the thesis procedure is given in Figure 2.1, which will motivate the following subsections.

2.1 Actual Mine Environment and Observations

The experimental measurements were performed in an open-pit mining facility in northern Canada in selected periods in 2018 and 2019. The facility is located near the Wood Buffalo National Park of Canada (Figure 2.2). As shown in Figure 2.2b, the facility includes a tailings pond, which is an area of refused mining waste where the waterborne refuse material is pumped, and most of the outlets of the pumps are located near the barren area on the east side of the pond. Open-pit mining excavations are primarily conducted over the mine area. The mine is approximately 100-m deep, with a width-to depth aspect ratio of greater than 20.

A SONic Detection And Ranging (SODAR) device, a Tethered And Navigated Air Blimp (TANAB) [21, 96], and an ultrasonic anemometer were used to determine profiles of wind speed and potential temperature as well as friction velocity and turbulent sensible heat flux

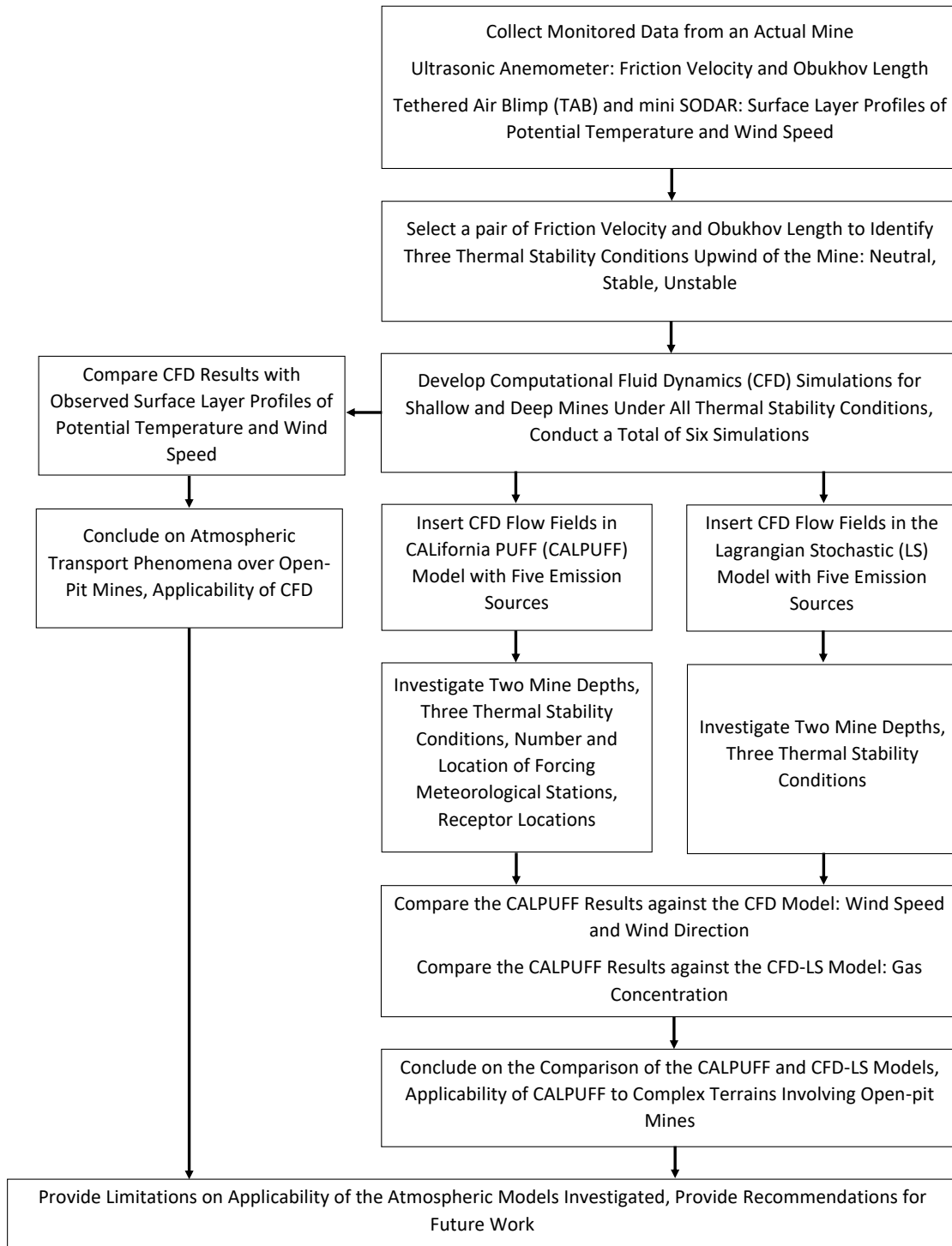


Figure 2.1: Summary of the thesis procedure.

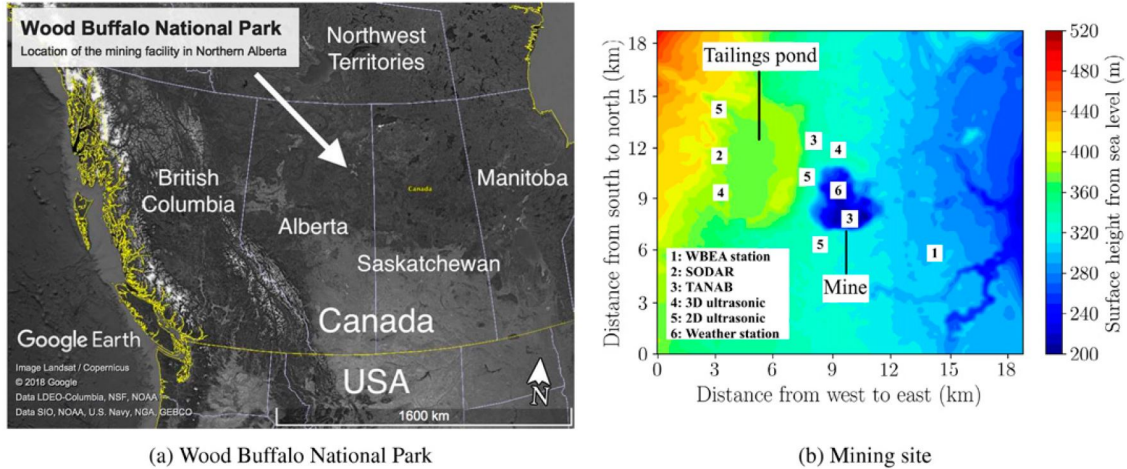


Figure 2.2: a) Map of the regional area where the mining facility is located; b) location of the meteorological instruments deployed at the site for model comparison, color coded with surface height above sea level; figure extracted from Nahian et al. (2020) [95].

at a reference height of $z = 10$ [m].

Wind speed and direction were measured with a 4000 series mini SODAR instrument by Radiometrics Corporation¹ (Figure 2.3) with a vertical resolution of 10 [m] from 30 [m] to 200 [m] altitudes with an output frequency of 60 [min]. This acoustic wind profiler had the capacity of measuring wind speed from 0 to 50 [m s^{-1}] with an accuracy of ± 0.5 [m s^{-1}] and wind direction from 0 to 359° with an accuracy of $\pm 5^\circ$.

The customized Tethered And Navigated Air Blimp (TANAB) contained a micro-climate sensor called TriSonicaTM Mini weather station by Applied Technologies, Inc.² (Figure 2.4) to measure wind speed, wind direction, pressure, temperature, and relative humidity with a sampling frequency of 10 [Hz] [21, 96]. It was capable of measuring temperature from 248.15 to 353.15 [K], wind speed from 0 to 30 [m s^{-1}], pressure from 50 to 115 [kPa], and relative humidity from 0 to 100 %. The measurement resolution of this mini weather station was ± 0.1 [m s^{-1}] for wind speed, $\pm 1^\circ$ for wind direction, and ± 0.1 [K] for temperature. Moreover, the accuracy of measurement for wind speed was ± 0.1 [m s^{-1}], for wind direction was $\pm 1^\circ$, and for temperature was ± 2 [K]. The TAB was launched up to an altitude of 200 [m] from the surface. Meteorological variables were statistically sampled every five minutes to produce means of horizontal wind speed and potential temperature as a function of time of day and height.

¹<http://radiometrics.com>

²<http://www.apptech.com>



Figure 2.3: mini SODAR used at the site; photo courtesy of Dr. Amir A. Aliabadi.



Figure 2.4: Tethered And Navigated Air Blimp (TANAB) used at the site; photo courtesy of Dr. Amir A. Aliabadi.

A CSAT 3B ultrasonic anemometer measured the three-dimensional wind components and temperature at a sampling frequency of 10 Hz as recommended by Aliabadi et al. (2019, 2021) [4, 5] from Campbell Scientific Inc.³. It was used to calculate the turbulent statistics of friction velocity u_* [m s^{-1}] and Obukhov length L [m] upwind of the mine. The anemometer had the capability of measuring wind speeds up to 30 [m s^{-1}] and temperature from 243.15 to 323.15 [K]. The measurement resolutions of the ultrasonic anemometer was ± 0.001 [m s^{-1}] for horizontal wind, ± 0.0005 [m s^{-1}] for vertical wind, $\pm 0.058^\circ$ for wind direction, and ± 0.002 [K] for temperature. Moreover, the accuracy was ± 0.08 [m s^{-1}] for horizontal wind, ± 0.04 [m s^{-1}] for vertical wind, and $\pm 10^\circ$ for wind direction.

The ultrasonic anemometer data were used to choose three pairs of friction velocity u_* [m s^{-1}] and Obukhov length L [m] values at the upstream of the domain which represented typical thermal stability conditions associated with unstable, neutral, and stable cases. The location for these sensors were chosen so that they would be upstream with the dominant wind direction (not shown). Next, selected dates and times were used, given the pair of friction velocity and Obukhov length, to retrieve mean horizontal wind speed and potential temperature profile data from the SODAR and TANAB for comparison to the CFD

³<https://www.campbellsci.ca>

model results. This procedure provided a consistent approach for model versus observation comparison under the three sets of thermal stability conditions.

2.2 Computational Fluid Dynamics (CFD) Model

The VLES method was developed by Aliabadi et al. (2018b) [7], and it was tested at wind tunnel scale for its predictions of mean momentum components, temperature, and various turbulence statistics [1, 7]. This method is developed for OpenFOAM 4.1. In this method, turbulence at the inlet is generated with a vortex method [7]. This method was initially developed by Sergent (2002) [125] and has been improved by Xie (2016) [147]. The main idea of the vortex method is generation of velocity fluctuations in the form of synthetic eddies derived from mean statistical information about the flow as a function of space (height above ground) and time. An inlet vortex field eliminated the need of a precursor simulation or implementation of a cyclic boundary condition at inlet-outlet faces. The number of vortices, vortex size, the vorticity, and the vortices life time are controlling parameters in this method [85]. The velocity fluctuations are produced by the vortex method on the inlet boundary. The theory is fully developed in the literature [14, 85, 125, 147] and provides the following velocity fluctuation field for a given time step [7]

$$\mathbf{u}(\mathbf{x}) = \frac{1}{2\pi} \sum_{i=1}^N \Gamma_i \frac{(\mathbf{x}_i - \mathbf{x}) \times \mathbf{m}}{|\mathbf{x}_i - \mathbf{x}|^2} \left(1 - e^{-\frac{|\mathbf{x}_i - \mathbf{x}|^2}{2(\sigma_i(\mathbf{x}_i))^2}} \right) e^{-\frac{|\mathbf{x}_i - \mathbf{x}|^2}{2(\sigma_i(\mathbf{x}_i))^2}}, \quad (2.1)$$

where \mathbf{u} [m s^{-1}] is velocity perturbation at the model inlet that is later superimposed on the mean inlet velocity, \mathbf{x} [m] is position vector on the inlet boundary, N [-] is the number of vortices to be inserted at the inlet, i is the index for the current vortex, Γ_i [$\text{m}^2 \text{s}^{-1}$] is the circulation for the current vortex, \mathbf{x}_i [m] is the position vector for the center of the current vortex, \mathbf{m} [-] is unit vector along the stream-wise direction, and $\sigma_i(\mathbf{x}_i)$ [m] is a characteristic length for the radius of current vortex. The velocity fluctuation fields from N [-] vortices are superimposed on the mean velocity field to provide an overall perturbed velocity field at the inlet. In fluid dynamics and turbulence theory, Reynolds decomposition is a mathematical technique used to separate the mean value of a quantity from its fluctuations. For example, for a quantity A , the Reynolds decomposition would be $A = \bar{A} + a$, where \bar{A} denotes the mean value of A and a is the deviation from the mean value due to turbulent fluctuations [94]. In this thesis, Reynolds decomposition is applied to all variables. A power-law profile is assumed for the mean velocity [134] given by

$$\bar{U}(z) = U_{ref} \left(\frac{z}{z_{ref}} \right)^\alpha, \quad (2.2)$$

where z_{ref} [m] is a reference height, U_{ref} [m s⁻¹] is a reference velocity, and α [-] is an exponent parameterized as a function of aerodynamic roughness length. The relationship between exponent α [-] and the characteristic aerodynamic roughness length of the surface z_0 [m] and turbulence intensity profile are given as [7]

$$\alpha = \frac{1}{\ln \left(\frac{z_{ref}}{z_0} \right)}, \quad (2.3)$$

$$I_u(z) = \frac{1}{\ln \left(\frac{z}{z_0} \right)}. \quad (2.4)$$

In atmospheric flows there is a limit to $I_u(z)$ [-] of typically the order of unity [7, 99, 131]. The parameterization of sub-grid turbulence kinetic energy (k_{sgs} [m² s⁻²]) is

$$k_{sgs}(z) = 1.5 [\bar{U}(z)I_u(z)]^2. \quad (2.5)$$

The characteristic size of the inlet vortices can be approximated by the scale of the inlet boundary given by $L_{in} = \frac{2L_zL_y}{L_z+L_y}$ [m] for the energy-containing eddies. L_z [m] and L_y [m] are inlet height and width. The size of the largest energy-containing vortices, i.e. σ_{max} [m], scales with L_{in} [m] as for atmospheric boundary-layer flow simulations the boundary-layer height δ [m] is in the order of L_{in} [m] for economized models. The relation between σ_{max} [m] and L_{in} [m] is established using a constant a_σ [-], to be defined later, as

$$\sigma_{max} = a_\sigma L_{in}. \quad (2.6)$$

The condition of $\Delta < \sigma_{max}$ [147] for the grid spacing Δ [m] should be satisfied in the coarsest region of mesh in a VLES method. This condition enables the VLES to resolve the transport, dynamics, and breakdown of the largest eddies in the flow. The size of energy-containing vortices or eddies is a function of height and must decrease with decreasing height. Energy-containing vortex size is parameterized using the mixing length approach of Mellor and Yamada (1974) [89] such that

$$\frac{1}{\sigma(z)} = \frac{1}{\sigma_{max}} + \frac{1}{\kappa(z + z_0)}, \quad (2.7)$$

where, $\kappa = 0.4$ [-] is the von Kármán constant. This formulation implies that $\sigma(z) \rightarrow \kappa z_0$ as $z \rightarrow 0$ and $\sigma(z) \rightarrow \sigma_{max}$ as $z \rightarrow \infty$. In the synthetic vortex method, $\sigma(z) = \sigma(\mathbf{x})$, so the energy-containing eddy size is represented at each height above ground, and it is incumbent upon the simulation to create the energy cascade, down to the local grid size Δ [m], within a short adaptation distance downstream of the inlet.

A characteristic time for the largest energy-containing vortices or eddies can be approximated using scaling. For the largest energy-containing eddies, the characteristic velocity U_0 [m s⁻¹] can be defined using the power-law and the reference height $U_0 = az_{ref}^\alpha$. For such eddies the length-scale can be found using $\ell_0 = \sigma_{max}$ [m]. The Reynolds number of the largest energy-containing eddies can be calculated with these two scales as $Re_{\ell_0} = U_0 \ell_0 / \nu$ [-]. These provide estimates for the Kolmogorov length-scale $\eta = \ell_0 Re_{\ell_0}^{-3/4}$ [m], Kolmogorov velocity scale $u_\eta = U_0 Re_{\ell_0}^{-1/4}$ [m s⁻¹], and dissipation rate $\epsilon = \nu (u_\eta / \eta)^2$ [m² s⁻³]. The characteristic life time for the largest energy-containing eddies in the flow can be given as [7]

$$\tau_0(\ell_0) = \left(\frac{\ell_0^2}{\epsilon} \right)^{1/3}. \quad (2.8)$$

This time scale is representative of only the largest eddies. Defining a representative time scale for all energy-containing eddies is possible by assuming a constant a_τ [-], to be adjusted later, given by

$$\tau = a_\tau \tau_0(\ell_0). \quad (2.9)$$

At the inlet, a new set of vortices can be sampled after every fixed number of iterations by use of this time scale. An incompressible turbulent flow based on a one-equation SGS model is considered. The dimensionless Navier-Stokes equations are developed and discussed below using a reference length-scale such as the boundary-layer height δ [m], a reference upstream velocity U_0 [m s⁻¹], a reference temperature Θ_0 [K], and a reference passive scalar S_0 [-]. With this model, the transport equations become

$$\frac{\partial \bar{U}_i}{\partial x_i} = 0, \quad (2.10)$$

$$\frac{\partial \bar{U}_i}{\partial t} + \frac{\partial}{\partial x_j} \bar{U}_i \bar{U}_j = -\frac{\partial \bar{P}}{\partial x_i} - \frac{\partial \tau_{ij}}{\partial x_j} + \frac{1}{Re} \frac{\partial^2 \bar{U}_i}{\partial x_j \partial x_j} + Ri \delta_{i3}, \quad (2.11)$$

$$\frac{\partial \bar{\Theta}}{\partial t} + \frac{\partial}{\partial x_i} \bar{U}_i \bar{\Theta} = -\frac{\partial \pi_i}{\partial x_i} + \frac{1}{RePr} \frac{\partial^2 \bar{\Theta}}{\partial x_i \partial x_i}, \quad (2.12)$$

$$\frac{\partial \bar{S}}{\partial t} + \frac{\partial}{\partial x_i} \bar{U}_i \bar{S} = -\frac{\partial \sigma_i}{\partial x_i} + \frac{1}{ReSc} \frac{\partial^2 \bar{S}}{\partial x_i \partial x_i}, \quad (2.13)$$

$$\frac{\partial k_{sgs}}{\partial t} + \bar{U}_i \frac{\partial k_{sgs}}{\partial x_i} = P + B - \epsilon + \frac{\partial}{\partial x_i} \left(\frac{2}{Re_T} \frac{\partial k_{sgs}}{\partial x_i} \right). \quad (2.14)$$

Even though all terms in these equations are explained in detail in other works [1, 3, 77], all the terms are described briefly here after transforming them from dimensionless to dimensional quantities. The over bar notation indicates the spatially-resolved solution for a variable. $\bar{P} = \bar{P}_* + \frac{1}{3}\tau_{ii}$ [m² s⁻²] is the resolved-scale modified kinematic pressure, which is normalized by constant density, where \bar{P}_* [m² s⁻²] is the resolved-scale static kinematic pressure. k_{sgs} [m² s⁻²] is SGS TKE. $\tau_{ij} = \bar{U}_i \bar{U}_j - \bar{U}_i \bar{U}_j = -2\nu_T \bar{S}_{ij}$ [m² s⁻²] is the SGS momentum flux, where $\bar{S}_{ij} = \left(\frac{\partial \bar{U}_i}{\partial x_j} + \frac{\partial \bar{U}_j}{\partial x_i} \right)$ [s⁻¹] is the rate of strain and $\nu_T = C_k k_{sgs}^{1/2} l$ [m² s⁻¹] is turbulent viscosity, in which C_k [-] is a constant and l [m] is the SGS mixing length to be defined later. $\pi_i = \bar{U}_i \bar{\Theta} - \bar{U}_i \bar{\Theta} = \frac{-\nu_T}{Pr_T} \frac{\partial \bar{\Theta}}{\partial x_i}$ [m s⁻¹ K] is the SGS kinematic heat flux, where $Pr_T = 0.85$ [-] is turbulent Prandtl number. In the logarithmic region, Pr_T is expected to be a constant for fluids with molecular Prandtl number of order unity, such as air and water [75, 113]. In this region, Pr_T should be independent of the distances from the wall and can be inferred from the slopes of the normalized mean velocity and temperature profiles [66]. It is known, both theoretically and experimentally, that turbulent transport of heat in the ABL, relative to turbulent transport of momentum, is enhanced under thermally-unstable conditions due to the role of buoyancy. From the extensive laboratory experiments, field experiments, and theoretical work, one expects that the value of Pr_T should range from 0.7 to 0.9 [74]. $Re = \frac{U_0 \delta}{\nu}$ [-] is the Reynolds number, $Re_T = \frac{U_0 \delta}{\nu_T}$ [-] is the SGS model turbulence Reynolds number, $Pr = \frac{\nu}{\alpha}$ [-] is the laminar Prandtl number, in which α [m² s⁻¹] is molecular thermal diffusivity. $Ri = \frac{g \delta \Delta \Theta}{\Theta U_0^2}$ [-] is the bulk Richardson number. The SGS component of the passive scalar transport is modeled using the eddy-viscosity assumption, $\sigma_i = \bar{U}_i \bar{S} - \bar{U}_i \bar{S} = \frac{-\nu_T}{Sc_T} \frac{\partial \bar{S}}{\partial x_i}$ [m s⁻¹], where $Sc_T = 0.85$ [-] is the turbulent Schmidt number. The turbulent Schmidt number Sc_T is a non-dimensional variable, describing the ratio of the turbulent transfer of momentum over the turbulent transfer of atmospheric species [70]. The suggested range of Schmidt number for ABL studies is from 0.5 to 1 [34, 48, 149], with 0.8 being a typical value justified by wind tunnel testing and numerical simulations

[152]. $P = -\tau_{ij}\overline{S}_{ij}$ [$\text{m}^2 \text{s}^{-3}$] is the shear production. $B = -\frac{g\nu_\theta}{\Theta} \frac{\partial \overline{\Theta}}{\partial z}$ [$\text{m}^2 \text{s}^{-3}$] is the buoyant production. $\epsilon = \frac{C_\epsilon k_{sgs}^{3/2}}{l}$ [$\text{m}^2 \text{s}^{-3}$] is the dissipation rate. δ_{ij} [-] is the Kronecker-delta function. By using parametrizations for the remaining quantities, the turbulence model is closed. C_k [-] is taken to be 0.094, and C_ϵ [-] is taken to be 1.048. The length-scale is estimated as a function of local grid size but damped near the walls using van Driest damping functions to prevent excessive dissipation of TKE near the walls [138]. The length-scale, not near the walls where damping functions are used, is formulated as

$$l = C_\Delta (\Delta x \Delta y \Delta z)^{1/3}, \quad (2.15)$$

where C_Δ [-] is a parameter to control l [m] and therefore the SGS model. This SGS model is known as `oneEqnEddy` in OpenFOAM.

The inflow is along the x axis, the y axis is in the span-wise direction, and the z axis is vertical direction above ground. For velocity, the synthetic vortex method is used at the inlet, the no-slip condition is used at the domain bottom, slip condition is used on the domain top, and the zero-gradient condition is used at the outlet. The `mappedField` boundary condition, which is a tool in OpenFOAM to map the desired values to each grid cells, is used to set the potential temperature profile at the inlet. This boundary condition provides a self-contained version of the mapped condition. It does not use information on the patch; instead it holds the data locally [47]. A spatially-uniform fixed value is used for potential temperature on the bottom surface, and zero gradient condition is used on the top and outlet surfaces. The `mappedField` boundary condition is also used to set a fixed value of 1 [-] for the passive scalar at the bottom of the domain on the footprint of the mines. Note that this option was only employed within CFD, while for the Lagrangian Stochastic (LS) model, to be discussed in Section 2.3, five separate area sources were defined. Zero gradient condition is used on the top and outlet surfaces. Airflow enters the domain from the west side, and the outlet of the domain is on the east side. The cyclic boundary condition is assumed for the north and south boundaries for all variables. For the cyclic boundaries, two mapped boundaries are needed for both sides. To make the boundary condition meet this criterion, at the north and south, the domain is expanded from the sides to form two mapped vertical planes.

For SGS TKE, the `atmBoundaryLayerInletK` boundary condition, which assumes that the entire inlet boundary is in the inertial surface layer of ABL, is used at inlet [131]. The friction velocity in this boundary condition is calculated by assuming the log-law, as

$$u_* = \frac{\kappa U_{ref}}{\ln\left(\frac{z_{ref} + z_0}{z_0}\right)}, \quad (2.16)$$

and then computes a uniform SGS TKE as $k_{sgs} = u_*^2 / C_\mu^{1/2}$ [$\text{m}^2 \text{s}^{-2}$], where $C_\mu = 0.09$ [-] is a constant. Much of the TKE is contained in the scales resolved by VLES, so it is expected that k_{sgs} [$\text{m}^2 \text{s}^{-2}$] will sharply drop in the stream-wise direction near the inlet, but it will stabilize in the interior of the domain in the stream-wise direction. Specification of k_{sgs} [$\text{m}^2 \text{s}^{-2}$] in this manner will provide a convenient method to develop the inlet condition for the synthetic vortex method. The zero-gradient condition is used at the outlet as well as the inlet and outlet for the turbulent viscosity.

At the bottom surface (wall) the `nutkAtmRoughWallFunction` boundary condition is used. This condition modifies the turbulent viscosity near the surface such that

$$\nu_T = \nu \left(\frac{\kappa z^+}{\ln \bar{E}} - 1 \right), \quad (2.17)$$

where, $z^+ = u_* z / \nu$ [-] is the non-dimensional wall-normal distance, and $\bar{E} = (z + z_0) / z_0$ [-]. Based on the environmental flow wall function, the chosen wall function for the model is given by [111]

$$U^+ = \frac{1}{\kappa} \ln\left(\frac{z + z_0}{z_0}\right) \approx \frac{1}{\kappa} \ln\left(\frac{z}{z_0}\right), \quad (2.18)$$

where z_0 [m] is characteristic aerodynamic roughness length of the surface, $\kappa = 0.4$ [-] is the von Kármán constant, and U^+ [-] is non-dimensional mean horizontal velocity. For TKE, the following wall function, which is known as `kqRWallFunction` in OpenFOAM, is used [47]

$$k_{sgs} = \frac{u_\tau^2}{C_\mu^{1/2}}, \quad (2.19)$$

where $C_\mu = 0.09$ [-] is a constant. The wall function for temperature used in the current VLES method is inspired from Aliabadi et al. (2018a) [2] that correlates the $\Theta^+ = (\Theta_s - \Theta) \rho c_p u_\tau / q_s$ [-] (where q_s is surface heat flux) and the logarithm of z^+ [-] via a linear relationship as

$$\Theta^+ = \frac{1}{\kappa_\theta} \ln(z^+) + B_\theta, \quad (2.20)$$

where $\kappa_\theta = 0.48$ [-] is the thermal von Kármán constant, and $B_\theta = 3.9$ [-] is a turbulence model constant. However, it is more common to formulate the Θ^+ [-] based on the U^+ [-] as

$$\Theta^+ = Pr_T(U^+ + Pr_f), \quad (2.21)$$

where Pr_T [-] is the turbulent Prandtl number, and Pr_f [-] is described by Jayatillaka (1969) [59]. This wall function is known as `alphatJayatillekeWallFunction` in OpenFOAM. In the VLES method, turbulent Prandtl number near the wall can be different from the turbulent Prandtl number in the interior of the domain. Considering the proposed range of 0.3 to 1 in the literature [66, 74, 75, 149]) a turbulent Prandtl number of $Pr_T = 0.3$ [-] is chosen for the wall treatment in the simulations.

2.2.1 Calculation of the CFD Model Friction Velocity and Obukhov Length at the Reference Height

According to Monin-Obukhov Similarity Theory (MOST) [91], the vertical profiles of wind and temperature in the thermally-neutral atmospheric surface layer follow a logarithmic form, which reduces to zero wind or a fixed surface temperature at ground level. However, when thermal stability is taken into account, the profile can deviate significantly from the standard thermally-neutral logarithmic profile [92, 137]. In MOST, L [m] denotes the Monin-Obukhov length, which defines atmospheric thermal stability, defined as

$$L = -\frac{\bar{\Theta}_{10\text{ m}} u_*^3}{\kappa g \overline{w\theta}}, \quad (2.22)$$

where u_* [m s⁻¹] is the friction velocity, $\bar{\Theta}_{10\text{ m}}$ [K] is the potential temperature at a reference height, $\kappa = 0.4$ [-] is the von Kármán constant, and $\overline{w\theta}$ [m s⁻¹ K] is the turbulent sensible kinematic vertical heat flux.

To compare to observed reference friction velocity and Obukhov length, the values of friction velocity and Obukhov length from the CFD model are calculated. The CFD model computes the resolved (k_{res}) and SGS (k_{sgs}) components of TKE [m² s⁻²] as well as the resolved vertical sensible kinematic turbulent heat flux ($\overline{w\theta}_{res}$ [m s⁻¹ K]). These values are used, combined with scaling formulations of Panofsky et al. (1977) [102], to estimate the total friction velocity and Obukhov length from the model. The friction velocity is related to the total TKE via

$$k_{tot} = k_{res} + k_{sgs} = \frac{u_*^2}{2} \left(\frac{\overline{u^2}}{u_*^2} + \frac{\overline{v^2}}{u_*^2} + \frac{\overline{w^2}}{u_*^2} \right). \quad (2.23)$$

Scaling of terms in the bracket enable calculation of the friction velocity as a function of k_{tot} by rearranging this equation. For thermally-stable and neutral conditions, the terms in the bracket are scaled as

$$\frac{\overline{u^2}}{u_*^2} = b_u^2, \quad \frac{\overline{v^2}}{u_*^2} = b_v^2, \quad \frac{\overline{w^2}}{u_*^2} = b_w^2, \quad (2.24)$$

where $b_{u,v,w}$ [-] is 2.5, 2.0, and 1.25, respectively. For the thermally-unstable conditions, the vertical component of the Equation 2.23 is scaled using

$$\frac{\overline{w^2}}{u_*^2} = b_w^2 \left(1 - 3\frac{z}{h}\right)^{2/3}, \quad (2.25)$$

where $z = 10$ [m] is the reference height and $h = 1000$ [m] is an assumed length scale representing the height of the planetary boundary layer. Further, the horizontal components of Equation 2.23 can be scaled using

$$\frac{\overline{u^2}}{u_*^2} = b_u^2 + \frac{0.35w_*^2}{u_*^2}, \quad (2.26)$$

$$\frac{\overline{v^2}}{u_*^2} = b_v^2 + \frac{0.35w_*^2}{u_*^2}, \quad (2.27)$$

where $w_{*,res}$ [m s^{-1}] is the convective velocity scale (also known as the Deardorff velocity) calculated using h [m], $\overline{w\theta}_{res}$ [m s^{-1} K], and $\overline{\Theta}_{10\text{ m}}$ [K] (the reference potential temperature) as

$$w_{*,res} = \left(\frac{hg\overline{w\theta}_{res}}{\overline{\Theta}_{10\text{ m}}}\right)^{1/3}, \quad (2.28)$$

where g [m s^{-2}] is gravitational acceleration. The non-linearity of the equations above under the thermally-unstable condition requires an iterative solution for u_* . To calculate the Obukhov length, only the resolved vertical sensible kinematic turbulent heat flux ($\overline{w\theta}_{res}$ [m s^{-1} K]) is available. Therefore, only the resolved friction velocity ($u_{*,res}$ [m s^{-1}]) will be used in the L [m] calculation:

$$L_{res} = -\frac{\overline{\Theta}_{10\text{ m}}u_{*,res}^3}{\kappa gw\overline{\theta}_{res}}. \quad (2.29)$$

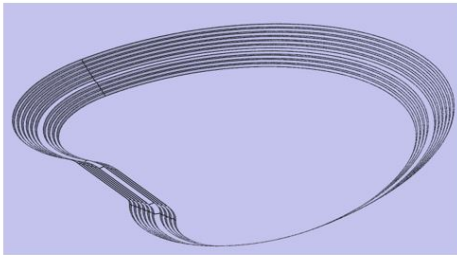
2.2.2 Model Geometry and Domain Size

In the present thesis, two sets of synthetic mine geometries, namely shallow and deep mines, are simulated to demonstrate the importance of mine depths and wall details in determining flow patterns. Figure 2.5 shows the generated shallow and deep mine geometries based on the stepped walls and overall kidney-shape mines. In designing the mine walls, typically the maximum ramp height is 12 [m]. A minimum 1-lane road width would be twice a truck width plus two windrow widths; a minimum 2-lane road would be a 3.5 time of a truck width plus two windrow widths. For a Komatsu 830e haul truck (7.3 [m] wide) this suggests a ramp of 25 [m] wide and 10 [m] tall (single road) or 40 [m] wide and 10 [m] tall (double road). The bench width can vary between 3 to 30 [m] depending on the mine type and the overall slope angle of the wall. For example, for an oil sand mine, the bench face angle can be changed from 20° to 30° resulting in a bench width of approximately 10 [m]. In Table 2.1 the details of mine wall and dimensions are presented. It can be seen that there are two ramps in the deep mine and one ramp in the shallow mine. Adding more ramps are necessary for the deep mine as the trucks should travel deeper on the wall of the mine. The overall slope and bench face angles are sharper for the deep mine than the shallow mine to make possible digging in the deeper layer. Also, the heights of the benches and ramps are higher for the deep mine than the shallow mine.

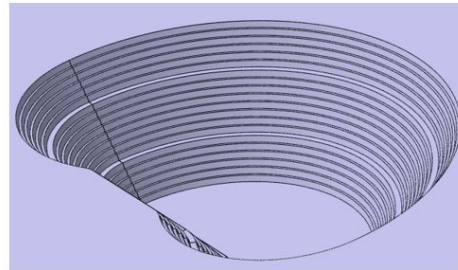
Table 2.1: Dimensions of the stepped shallow and deep mines.

Geometry	Dimension	
	Shallow Mine	Deep Mine
Overall Slope Angle	30°	50°
Bench Face Angle	60°	70°
Mine Depth	100 [m]	500 [m]
Mine Length	1500 [m]	1500 [m]
Mine Width	2000 [m]	2000 [m]
Bench Height	10 [m]	25 [m]
Bench Width	10 [m]	10 [m]
Ramp Height	10 [m]	25 [m]
Ramp Width	25 [m]	25 [m]

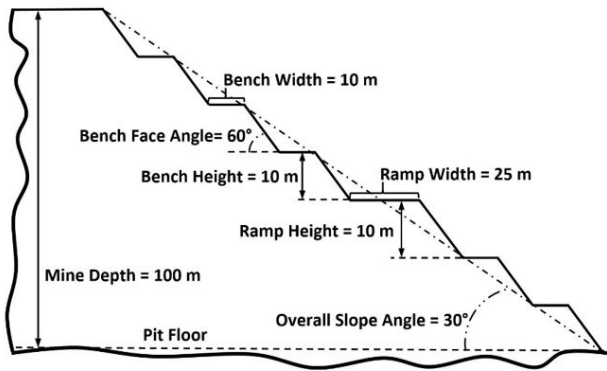
The CFD model should simulate the roughness sub-layer in the atmosphere, which is approximately five times the roughness element height [3, 92]. For example, if the domain height is 200 [m], the deepest mine that can be simulated is 40 [m]. To simulate a 500 [m] deep mine, the domain height should be 2500 [m]. Since a 500-m deep mine is investigated,



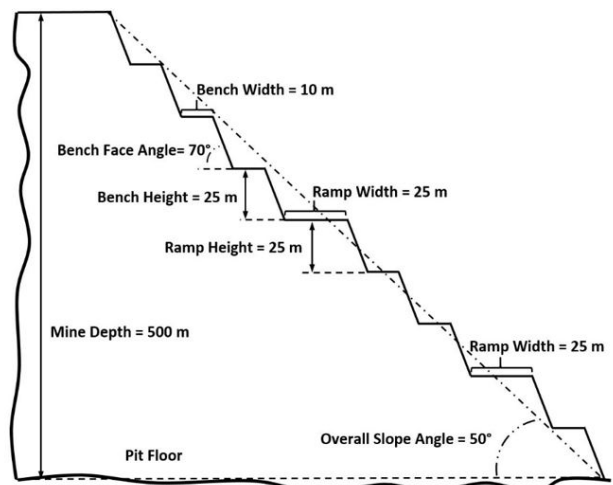
(a)



(b)



(c)



(d)

Figure 2.5: a) Shallow and b) deep synthetic mine geometries, c) shallow and d) deep synthetic mine walls.

the height of the domain is 2500 [m] for all simulations. For both cases, the domain length and width are 10000 [m] and 6000 [m], respectively. The mines' upstream edge is located after the half point in the stream-wise direction. This allows for an adaptation distance such that flow mean and turbulence statistics adopt representative atmospheric conditions before studying transport phenomena over the mines.

2.2.3 Numerical Schemes, Solution Control, Averaging, and Probing

A second-order implicit backward time scheme is used. Gradient schemes are based on second-order Gaussian integration with linear interpolation. All Laplacian schemes are based on corrected Gaussian integration with linear interpolation, which provide unbounded, second-order, and conservative numerical behavior. Divergence schemes are based on Gaussian integration with linear or upwind interpolation, depending on the variable of interest [47].

Throughout all simulations, time-steps are chosen so that the maximum Courant number satisfies $Co = \Delta t |\bar{U}| / \Delta x < 0.1$ [-]. The pressure matrix is preconditioned by the diagonal incomplete Cholesky technique and solved by the preconditioned conjugate gradient solver. Other variables are preconditioned by the diagonal incomplete-lower-upper technique and solved by the preconditioned bi-conjugate gradient solver. The pressure-linked equations (i.e. equations that have a pressure term) are solved by a hybrid method consisting of two algorithms: 1) the pressure-implicit split-operator method and 2) the semi-implicit method [47].

In Table 2.2 the important input variables of the VLES method are presented. The potential temperature difference (top minus bottom) at the inlet for the thermally-unstable and stable conditions are set to -2 [K] and $+5$ [K], respectively. This potential temperature difference is set between the surface up to 100 [m], and after that, the potential temperature is constant to the top of the domain. The filter size parameter (C_Δ) [-] is chosen to be higher for thermally-unstable conditions than the thermally-neutral and stable conditions. A smaller C_Δ [-] causes less turbulence fluctuation near the surfaces, where turbulence is mostly modeled. In the thermally-stable conditions, the atmosphere is more calm than the thermally-unstable conditions and a smaller C_Δ [-] helps the model to represent the thermally-stable condition better. The length-scale and time-scale constants (a_σ [-] and a_τ [-]) are set to 1 and these constants remained fixed for all thermal stability conditions. As

the Turbulence Intensity (TI) decreases, less turbulence is injected in the domain. The TI tends to be higher in thermally-unstable conditions, than in the thermally-stable conditions [3, 54]. In the present simulations, higher TI is chosen for the thermally-unstable conditions ($TI = 0.3$ [-]) than the thermally-neutral or stable conditions ($TI = 0.1$ [-]). Surface roughness is $z_0 = 0.3$ [m] all over the domain, which creates a uniform aerodynamic roughness for all surfaces [111]. To create the desired power-law velocity profile, two parameters (U_{ref} [m s⁻¹] and z_{ref} [m]) are used to define the inlet wind profile. It should be noted that the combination of U_{ref} [m s⁻¹] and z_{ref} [m] affect the velocity profile at the inlet.

After the flow passes over the domain in the stream-wise direction once with a time step of 0.1 [s], the simulations are extended for an additional two flow passes over the domain with a time step of 0.01 [s] to obtain statistical information by time averaging. Note that with a finer time step of 0.01 [s], the solution is extracted at a sampling rate of 0.1 [s] to match the ultrasonic anemometer sampling frequency (10 [Hz]). Note that one pass can be interpreted as the characteristic flow time in the stream-wise direction, and multiple characteristic flow times must be reached before obtaining statistical information about the flow. The smaller time step in Table 2.2 helps extracting more accurate averages for comparison to observations. The averaging period is set to 15 [min].

Table 2.2: CFD input variables for different thermal stability and mine depth simulation cases.

Thermal Stability Conditions	Mine Type	C_Δ [-]	a_σ [-]	a_τ [-]	TI [-]	z_0 [m]	U_{ref} [m s ⁻¹]	z_{ref} [m]	Time Step 1 [s]	Time Step 2 [s]
Unstable ($\Delta\bar{\Theta} = -2$ [K])	Shallow	1	1	1	0.3	0.3	3.5	500	0.1	0.01
	Deep	1	1	1	0.3	0.3	3.5	500	0.1	0.01
Neutral ($\Delta\bar{\Theta} = 0$ [K])	Shallow	0.5	1	1	0.1	0.3	10	100	0.1	0.01
	Deep	0.3	1	1	0.1	0.3	10	100	0.1	0.01
Stable ($\Delta\bar{\Theta} = +5$ [K])	Shallow	0.001	1	1	0.1	0.3	4	20	0.1	0.01
	Deep	0.001	1	1	0.1	0.3	4	20	0.1	0.01

To statistically sample the flow characteristics in order to compare the model results with field measurements, two sets of probes are inserted inside the domain. To analyze the upstream and downstream surface-layer profiles, the first set of probes are used. These are distributed on 10 profiles (P1 to P10), which are located in the central axis at $y = 3000$ [m] to the west and east sides of the mine. Each profile is 100 [m] tall with 5-m probe spacing in the vertical direction. The second set is additional probes on profiles (P11 to P13) inside the mine that extend up to 100 [m] altitude above grade. The probe spacing on these is every 5 [m]. The probing setup can be seen in Figure 2.6.

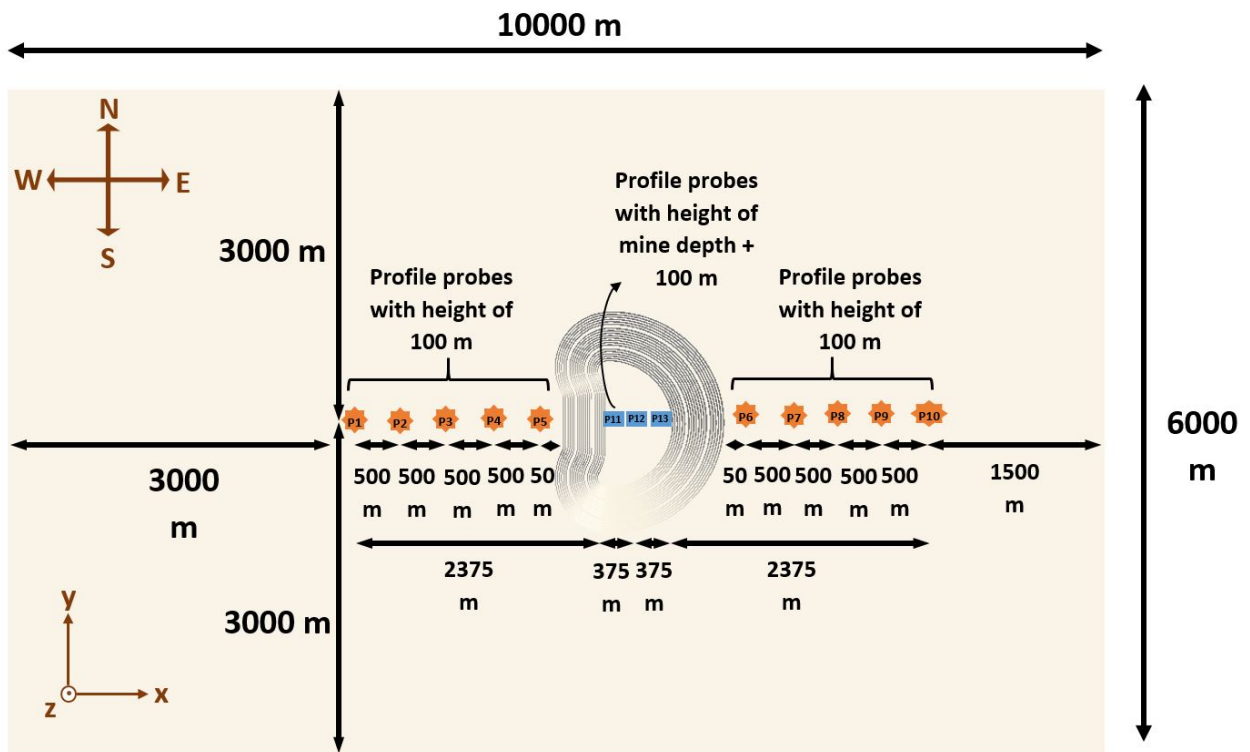
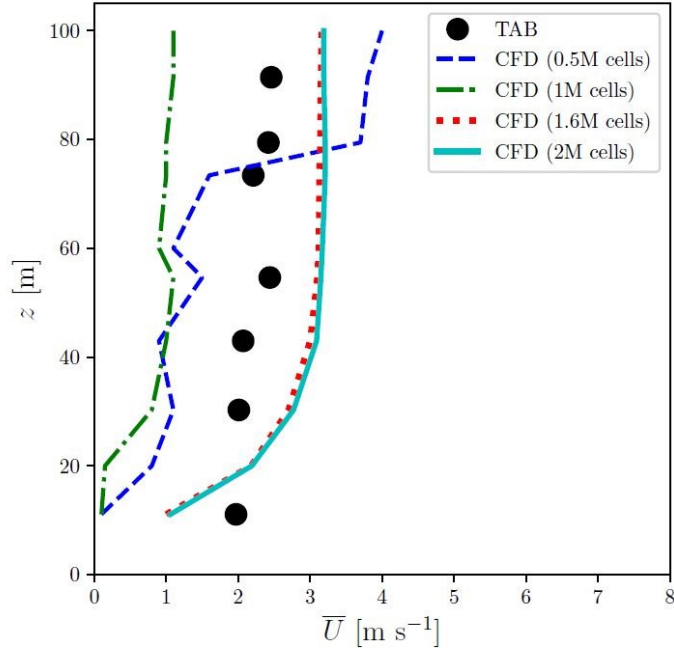


Figure 2.6: Top view of probing locations.

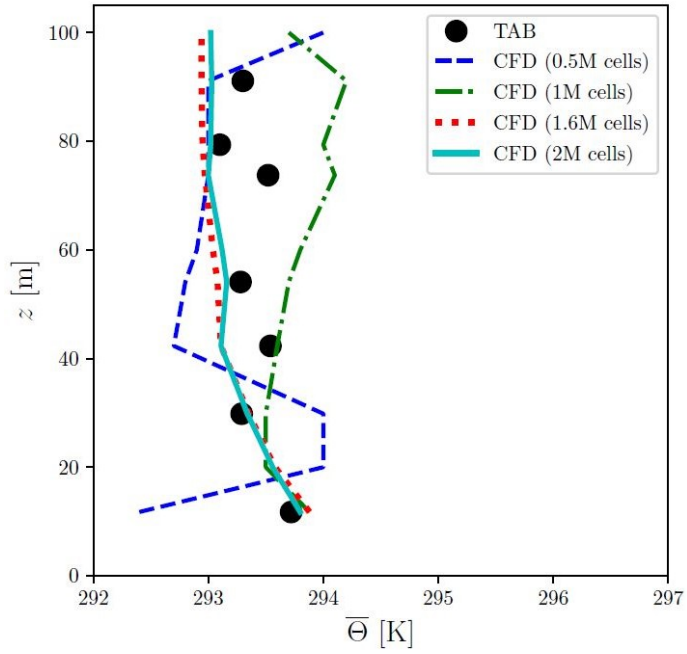
2.2.4 Grid Resolution

The computational grid is generated using the `snappyHexMesh` utility provided in OpenFOAM 4.1. The vertical mesh is refined inside the mine and near the surface to resolve the energy cascade as much as possible close to the ground and inside the mine. The mesh discretization in the vertical direction is set to be 2 [m] from the bottom of the mine to 100 [m] above grade (Vertical Region 1 in Table 2.3); then it increases to 30 [m] up to 1000 [m] above ground (Vertical Region 2 in Table 2.3), and finally, it is set to 75 [m] up to the top of the domain (Vertical Region 3 in Table 2.3). The cells are produced with wall-normal dimensions (z^+ [-]) of between 200 and 2000 adjacent to the surface. The z^+ [-] is the distance in wall units between the centroid of the first cell and the wall. Various upper limits have been reported for the z^+ [-] to satisfy the log-law. Conservative estimates suggest $z^+ < 500-1000$ [-] applicable to smooth and very rough walls with intercept adjustments [17]. Non-conservative upper limits have been shown to exhibit a near log-law behaviour for $z^+ \rightarrow 10000$ [-] [67]. However, it is impossible to satisfy this criterion everywhere when processes of flow separation and attachment occur. The mesh in the horizontal direction is divided into two sections. First, a very fine mesh is generated surrounding the mine area from $x = 2500$ [m] to 9000 [m] that extends to the edges of the domain with a grid spacing of 50 [m] by 50 [m] (Horizontal Region 1 in Table 2.3). Second, a coarse mesh is used near the inlet ($x = 0$ [m] to 2500 [m]) and outlet ($x = 9000$ [m] to 10000 [m]) of the domain, with a grid spacing of 170 [m] by 170 [m] (Horizontal Region 2 in Table 2.3). This kind of mesh is generated to simulate the flow more accurately in the sensitive areas, which is close to the center of the domain and, in the meantime, to avoid high computational cost elsewhere. A sensitivity analysis on the mesh is performed to select the best cell number for each mine type. Four different numbers of mesh elements in horizontal and vertical directions (Table 2.3) are generated for the shallow mine under the thermally-unstable case. For each case, the velocity and potential temperature profiles on P3 (Figure 2.6) are plotted and compared with the observations of Tethered And Navigated Air Blimp (TANAB) (Figure 2.7). By looking at Figure 2.7, it is evident that the profiles associated with 0.5M and 1M cells deviate from the profiles of the observation, while results associated with 1.6M and 2M simulations are closer to the observations.

Table 2.4 shows the Bias = $\frac{\sum_{i=1}^n (M_i - O_i)}{n}$ and Root Mean Square Error (RMSE) = $\sqrt{\frac{\sum_{i=1}^n (M_i - O_i)^2}{n}}$ of mean horizontal velocity and potential temperature profiles predicted by CFD (M_i) in comparison to observed TANAB data (O_i). The Bias and RMSE of the cases with 1.6M and 2M mesh elements are lower than other cases. It is confirmed that the selected mesh



(a)



(b)

Figure 2.7: a) Mean horizontal velocity (\bar{U}) and b) potential temperature ($\bar{\Theta}$) profiles at P3 versus observations with different cell numbers for the thermally-unstable shallow mine simulation; note the Tethered Air Blimp (TAB) is another name for TANAB.

Table 2.3: Different mesh grading options in the horizontal and vertical regions of the simulation domain.

	Horizontal Region 1	Horizontal Region 2	Vertical Region 1	Vertical Region 2	Vertical Region 3
CFD (0.5M cells)	$dx = dy = 500$ [m]	$dx = dy = 200$ [m]	$dz = 20$ [m]	$dz = 80$ [m]	$dz = 150$ [m]
CFD (1M cells)	$dx = dy = 300$ [m]	$dx = dy = 100$ [m]	$dz = 10$ [m]	$dz = 60$ [m]	$dz = 100$ [m]
CFD (1.6M cells)	$dx = dy = 170$ [m]	$dx = dy = 50$ [m]	$dz = 2$ [m]	$dz = 30$ [m]	$dz = 75$ [m]
CFD (2M cells)	$dx = dy = 150$ [m]	$dx = dy = 40$ [m]	$dz = 1.5$ [m]	$dz = 25$ [m]	$dz = 60$ [m]

Table 2.4: Bias (RMSE) for mean horizontal velocity (\bar{U}) and potential temperature ($\bar{\Theta}$) calculated for CFD on profile P3 with different cell numbers versus observations; data reported for the shallow mine case under thermally-unstable condition.

	Bias (RMSE) of \bar{U} [m s ⁻¹]	Bias (RMSE) of $\bar{\Theta}$ [K]
CFD (0.5M cells)	-1.09 (1.17)	-0.49 (0.83)
CFD (1M cells)	-1.33 (1.36)	0.28 (0.34)
CFD (1.6M cells)	0.44 (0.84)	-0.19 (0.33)
CFD (2M cells)	0.51 (0.88)	-0.18 (0.30)

resolutions with 1.6M cells provides better accuracy than the lower resolution simulations, and similar to the 2M cell simulation. Hence, the grid spacing associated with the 1.6M cells is chosen for the rest of the simulations.

2.3 Lagrangian Stochastic (LS) Model

Gas dispersion is calculated from the CFD flow fields using a Lagrangian Stochastic (LS) model. This was in addition to the passive tracer option discussed in Section 2.2. The LS model calculates the x, y, z [m] trajectories of thousands of tracer particles as they travel downwind of the mine sources positioned at five locations along the mine wall. This is a first-order model, in which trajectories are calculated using a Langevin model to increment changes in particle velocities \bar{U} , \bar{V} , and \bar{W} [m s⁻¹] over a model time-step Δt [s]. The LS model details are described by Wilson et al. (2009 and 2010) [142, 143] and only a brief summary is provided here. The Langevin model uses gridded flow statistics calculated by the CFD model: the mean velocities in each coordinate, the velocity variances in the three coordinates $\sigma_{u,v,w}$ [m s⁻¹], and the turbulent kinetic energy dissipation rate ϵ [m² s⁻³]. In the LS simulations the covariance between velocity components are neglected. The LS model time-step is set as a fraction of the effective Lagrangian timescale, calculated as $T_L = 2\sigma_w^2(C_0\epsilon)^{-1}$ [s], with Δt [s] equal to $0.2T_L$ under unstable and neutral conditions, and $0.02T_L$ under stable condition (the value of C_0 is assumed to be 3.59 [-]). As particles move

downwind they may cross the ground surface (i.e. taken as the roughness length z_0 [m]), in which case the particles are reflected back into the flow domain.

To represent gas dispersion, 25000 model particles are released randomly over each source (with the footprint described in Section 2.4.1 and Figure 2.9). These particles travel away from the source in accordance with the flow field, and eventually move downwind of the mine and exit the model domain. A set of concentration receptors are located downwind of the mine pit (Figure 2.9). Each receptor is a volume ($\Delta x, \Delta y, \Delta z = 10, 50, 10$ [m]) where the time-average gas concentration is calculated from the residence time of the LS particles within the volume. The number and location of the receptors depend on the problem being investigated.

2.4 CALifornia PUFF (CALPUFF) Model

The CALPUFF modeling system includes three main components: CALMET, CALPUFF, and CALPOST. It also includes a large set of preprocessing programs designed to interface the model to standard, routinely-available meteorological and geophysical datasets. In the simplest terms, CALMET is a meteorological model that develops hourly wind and temperature fields on a three-dimensional gridded modeling domain. Associated two-dimensional fields such as mixing height, surface characteristics, and dispersion properties are also included in the file produced by CALMET. CALPUFF is a transport and dispersion model that advects and diffuses “puffs” of material emitted from modeled sources, simulating dispersion and transformation processes along the way. In doing so, it typically uses the fields generated by CALMET, or as an option, it may use simpler non-gridded meteorological data much like existing plume models. Temporal and spatial variations in the meteorological fields selected are explicitly incorporated in the resulting distribution of puffs throughout a simulation period. The primary output files from CALPUFF contain either hourly concentrations or hourly deposition fluxes evaluated at selected receptor locations. CALPOST is used to process these files, producing tabulations that summarize the results of the simulation, identifying the highest and second highest 3-hour average concentrations at each receptor, for example. When performing visibility-related modeling, CALPOST uses concentrations from CALPUFF to compute extinction coefficients and related measures of visibility, reporting these for selected averaging times and locations [123].

CALMET is a diagnostic meteorological model that generates mass-consistent wind fields. CALMET follows a three-step process to generate the wind field. The first step

is to interpolate or extrapolate observed wind data to grid points in the domain under study. The second step is to use parameterizations to account for the kinematical effects of terrain, slope flows, and blocking effects. The third step is to adjust wind fields to meet the mass continuity requirement by minimizing the divergence of the flow field. The CALMET model uses a grid system consisting of NZ layers of NX by NY square horizontal grid cells. In CALMET, the horizontal wind components are denoted by \bar{U} [m s^{-1}] and \bar{V} [m s^{-1}], and the vertical wind component is denoted by \bar{W} [m s^{-1}]. The CALMET model operates in a terrain-following vertical coordinate system [123].

The wind field interpolation is based on the inverse square of the weighted distance provided by Equation 2.30, giving more weight to the nearness of the observation points [123]

$$(\bar{U}, \bar{V})'_2 = \frac{\frac{(\bar{U}, \bar{V})_1}{R^2} + \sum_k \frac{(\bar{U}_{obs}, \bar{V}_{obs})_k}{R_k^2}}{\frac{1}{R^2} + \sum_k \frac{1}{R_k^2}}, \quad (2.30)$$

where $(\bar{U}_{obs}, \bar{V}_{obs})_k$ [m s^{-1}] are the observed wind components at stations k , $(\bar{U}, \bar{V})_1$ [m s^{-1}] are the step 1 wind components at a particular grid point, $(\bar{U}, \bar{V})'_2$ [m s^{-1}] are the step 2 wind components, R_k [m] are the distances from observational stations k to the grid point, and R [m] is the user-defined weight parameter for the winds calculated in step 1.

The interpolation scheme allows for the wind field to be heavily weighted by observations in the areas nearby the observational stations. An observation is excluded from interpolation if the distance from the observational station to a particular grid point exceeds a maximum radius of influence. Three separate maximum radii of influence parameters should be specified: over land surface ($RMAX1$ [km]), which reflects the limiting influence of terrain features on the interpolation at the surface, over land aloft ($RMAX2$ [km]), which account for the fact that the effects of terrain decrease with height, and over water ($RMAX3$ [km]), with a large value to ensure that all over-water grid points are within the radius of influence of at least one observation. The interpolation scheme allows for the wind field to be heavily weighted in the vicinity of the observational stations, while the step 1 wind field dominates the interpolated wind field in regions with no observational data. A pair of relative weighting values ($R1$ and $R2$ [km]) are given to the step 1 wind field. $R1$ [km] defines the radius applied to the surface layer of the wind field and $R2$ [km] describes the radius applied to the layers above the surface layer. The R [km] parameters define the radius around the location of interest at which the step 1 wind field and the observation data have similar influence during the calculation of the step 2 wind field. This radius is used to define a linear decay of station

influence on the surrounding wind field with increasing distance from the station location. The R [km] and $RMAX$ [km] values should be chosen based on topography and land use conditions. Domains with wind fields that change rapidly with distance should have smaller R [km] and $RMAX$ [km] values than domains with relatively homogeneous wind fields [123].

To determine the thermal stability conditions in CALMET, the sensible heat flux Q_h [$W\ m^{-2}$] is calculated by solving the energy balance Equation 2.31 [92, 93]

$$Q_* + Q_f = Q_h + Q_e + Q_g, \quad (2.31)$$

where Q_* , Q_f , Q_h , Q_e , Q_g [$W\ m^{-2}$] are the net radiation flux, the anthropogenic heat flux, sensible heat flux, latent heat flux, and storage/soil heat flux, respectively. The Anthropogenic heat flux is particularly important when energy intensive industry or dense urban environments are present [6]. The sensible heat term permits application of MOST, in which the friction velocity u_* [$m\ s^{-1}$] and Monin-Obukhov length L [m] are calculated to predict vertical profiles of wind speed. MOST can determine the stability conditions according to Table 2.5 [122].

Table 2.5: Monin-Obukhov Length classification for atmospheric stability [122].

Condition	Monin-Obukhov Length [m]
Extremely Unstable	$-100 \leq L < 0$
Unstable	$-500 \leq L < -100$
Neutral	$ L > 500$
Stable	$50 \leq L < 500$
Extremely Stable	$0 \leq L < 50$

A vertical extrapolation of the surface wind observations is performed by MOST to calculate $U(z)$ based on $U(z_1)$ [$m\ s^{-1}$] for wind speeds at the CALMET layers at heights z_1 and z [m] [123]

$$U(z) = U(z_1) \frac{\left[\ln \left(\frac{z}{z_0} \right) + \Psi_m \left(\frac{z}{L} \right) \right]}{\left[\ln \left(\frac{z_1}{z_0} \right) + \Psi_m \left(\frac{z_1}{L} \right) \right]}. \quad (2.32)$$

where Ψ_m [-] is the stability correction function based on the Dyer relations [29, 36, 92]. The stability correction functions are given by Equations 2.33, 2.34, and 2.35 for stable ($L > 0$ [m]), neutral ($L \sim 0$ [m]), and unstable ($L < 0$ [m]) conditions, respectively [123]

$$\Psi_m \left(\frac{z}{L} \right) = 4.8 \left(\frac{z}{L} \right), \quad (2.33)$$

$$\Psi_m \left(\frac{z}{L} \right) = 0, \quad (2.34)$$

$$\Psi_m \left(\frac{z}{L} \right) = -2 \ln \left[\frac{1+x}{2} \right] - \ln \left[\frac{1+x^2}{2} \right] + 2 \tan^{-1}(x) - \frac{\pi}{2}, \quad (2.35)$$

$$x = \left[1 - \left(16 \frac{z}{L} \right) \right]^{\frac{1}{4}}. \quad (2.36)$$

The intermediate step 2 wind field resulting from the addition of observational data into the step 1 wind field is subject to smoothing in order to reduce discontinuities in the wind field. The smoothing Equation used in CALMET is

$$(\overline{U}_{i,j})'' = 0.5 \overline{U}_{i,j} + 0.125 [\overline{U}_{i-1,j} + \overline{U}_{i+1,j} + \overline{U}_{i,j-1} + \overline{U}_{i,j+1}], \quad (2.37)$$

$$(\overline{V}_{i,j})'' = 0.5 \overline{V}_{i,j} + 0.125 [\overline{V}_{i-1,j} + \overline{V}_{i+1,j} + \overline{V}_{i,j-1} + \overline{V}_{i,j+1}], \quad (2.38)$$

where $(\overline{U}_{i,j})''$ and $(\overline{V}_{i,j})''$ [m s^{-1}] are horizontal components of the wind at grid point (i, j) after smoothing. The initial vertical velocity is determined from the incompressible mass conservation equation 2.39,

$$\frac{d\overline{U}''}{dx} + \frac{d\overline{V}''}{dy} + \frac{d\overline{W}_1}{dz} = 0, \quad (2.39)$$

where \overline{W}_1 is the vertical velocity in terrain-following coordinates, and \overline{U}'' and \overline{V}'' are the horizontal wind field components after smoothing.

After accounting for the kinematical effects of terrain, slope flows, and blocking effects, at the end of each step, the continuity equation is verified throughout the entire domain, ensuring a minimum divergence of the winds in each cell, as shown by Equation 2.40 [123]

$$\frac{d\overline{U}}{dx} + \frac{d\overline{V}}{dy} + \frac{d\overline{W}}{dz} < \epsilon, \quad (2.40)$$

where \overline{U} [m s^{-1}] and \overline{V} [m s^{-1}] are the horizontal wind components, \overline{W} [m s^{-1}] is the vertical velocity, and ϵ [s^{-1}] is the maximum allowable divergence.

The prepared terrain and wind field by CALMET are imported into CALPUFF. CALPUFF

is a transport and dispersion model that advects and diffuses puffs of material emitted from modeled sources, simulating dispersion and transformation processes along the way. CALPUFF is used for analyzing emissions from industrial sites [60], investigating air quality issues in urban areas [55], evaluating the health impacts of pollutants [100, 128], identifying the main sources of particulate matter [146], assessing the odor impacts on air quality [9, 109, 129], and studying dispersion patterns under different meteorological and land use conditions [120].

CALPUFF may also use simpler non-gridded meteorological data from existing plume models. Temporal and spatial variations in the meteorological fields selected are explicitly incorporated in the resulting distribution of puffs throughout the simulation domain and period. In CALPUFF, the equation for distribution of a puff is given as [123]

$$C = \frac{Q}{2\pi\sigma_x\sigma_y} \beta \exp\left[\frac{-d_a^2}{2\sigma_x^2}\right] \exp\left[\frac{-d_c^2}{2\sigma_y^2}\right], \quad (2.41)$$

$$\beta = \frac{2}{(2\pi)^{1/2}\sigma_z} \sum_{n=-\infty}^{\infty} \exp\left[\frac{-(H + 2nh)^2}{2\sigma_z^2}\right], \quad (2.42)$$

where, C [$\mu\text{g m}^{-3}$] and Q [μg] are the ground-level concentration and the pollutant mass in the puff. σ_x [m] and σ_y [m] are the standard deviations of the Gaussian distribution in the along- and cross-wind directions and σ_z [m] is the standard deviation of the Gaussian distribution in the vertical direction. d_a [m] and d_c [m] are the distance from the puff center to the receptor in the along- and cross-wind directions. β [m^{-1}] is the vertical term of the Gaussian equation. H [m] and h [m] are the effective height above the ground of the puff center and the mixed-layer height.

The primary output files from CALPUFF contain either concentrations or deposition fluxes evaluated at selected receptor locations [123].

2.4.1 Simulation Approach

At the first step, the wind field predicted by CFD [68] for each of the six different cases, are assumed as the real flow field over the synthetic open-pit mining area to be the input of the LS model. The concentration field produced by the CFD-LS model is used as the validation dataset for the CALPUFF plume distribution predictions. The wind field produced by the CFD model is used as the validation dataset for the flow field predicted by CALMET.

Figure 2.8 shows the generated shallow and deep kidney-shape mine geometries visualized

by CALPUFF View software version 8.6.0.

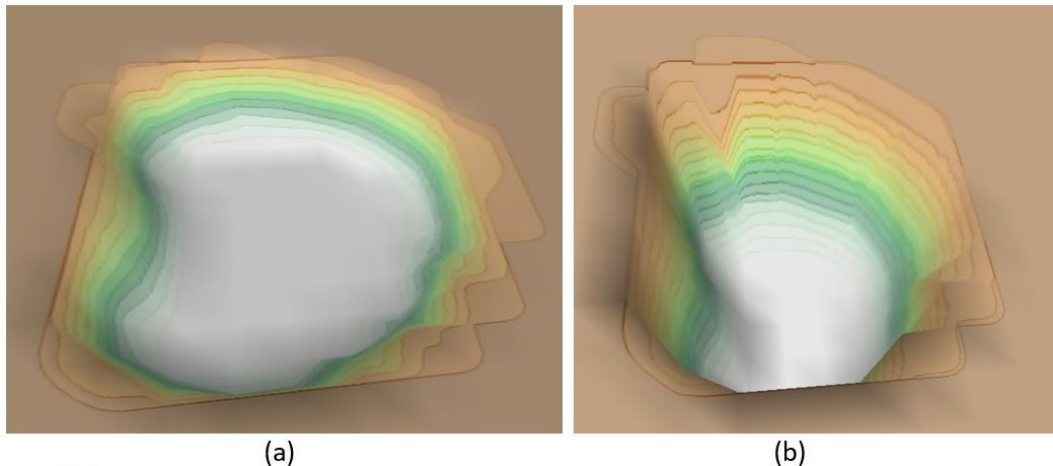


Figure 2.8: a) Shallow and b) deep synthetic mine geometries generated by CALPUFF View.

The terrain is generated with CALMET’s geophysical processor with the horizontal resolution of 250 [m] by 250 [m] with a user-defined land use. The surface roughness is set to be $z_0 = 0.3$ m, appropriate for the modified land within the boreal forest of northern Canada [68, 111], all over the domain, which creates a uniform aerodynamic roughness for all surfaces. The domain is divided into 11 vertical layers (0, 20, 40, 60, 80, 100, 200, 600, 800, 1000, 1200, and 1300 [m] above surface). The vertical layers are more dense below 100 [m], which is the area close to the surface. This part of the boundary layer is more important than upper layers for investigation of the plume distribution near the ground. The meteorological and gas sampling grid cells have a horizontal resolution of 250 [m] by 250 [m]. The same horizontal resolution is used in the LS simulations. Each emitting source releases pollutants at a rate of 1 [kg s⁻¹] from a volume of length, width, and height of 100 [m] by 100 [m] by 2 [m], with a total emission rate of 5 [kg s⁻¹] from all sources. CALPUFF is set to use properties of the methane gas as the pollutant. All of the sources are located at 50 [m] and 250 [m] above the pit’s bottom for shallow and deep mines, respectively. The exact location of sources and emission rates (blue squares in Figure 2.9) are presented in Table 2.6.

CALMET uses station data and/or prognostic data such as WRF or MM5 to produce the wind field. In the present simulations, only the station data option is chosen in CALMET. By choosing the station data, CALMET needs to have the meteorological data in the format of surface and upper air stations. As the simulations are inside a synthetic domain, there are no real meteorological surface and upper air stations for the simulations. The wind speed, wind direction, potential temperature, and pressure predicted by CFD are used to generate the

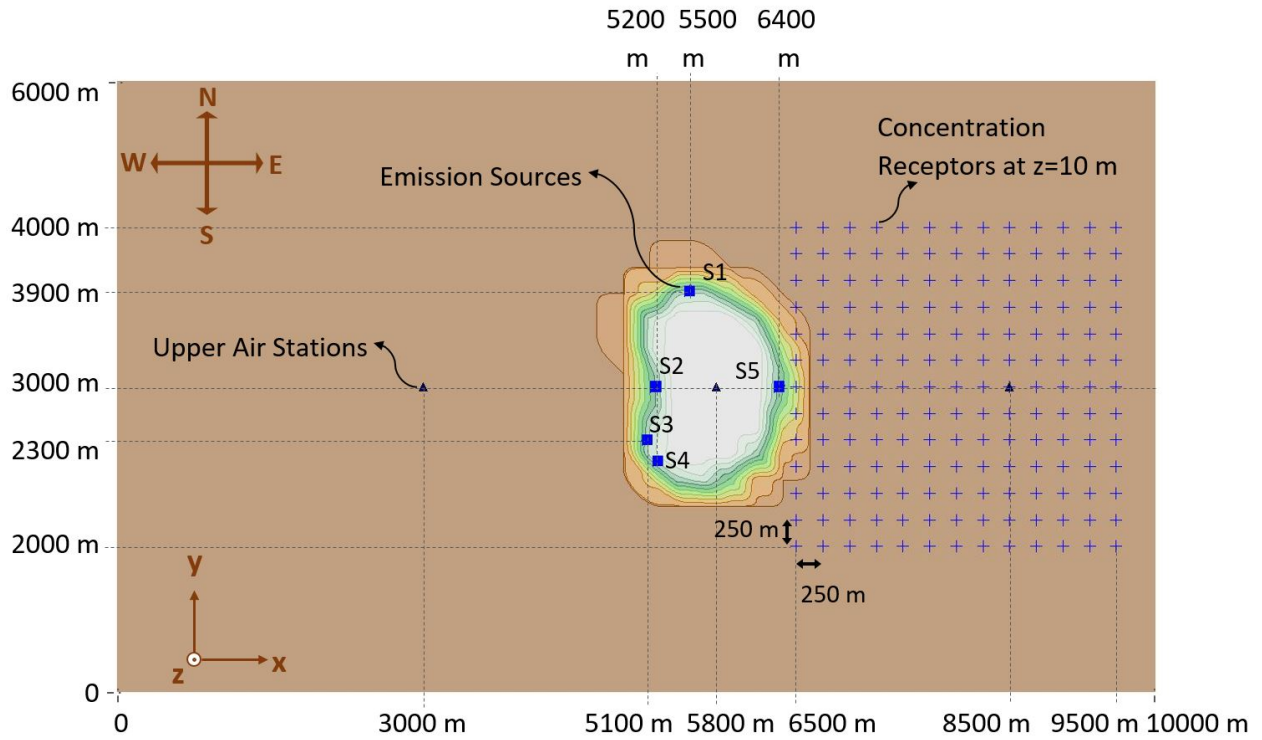


Figure 2.9: Location of emission sources, discrete receptors, and upper air stations in the CALPUFF domain.

Table 2.6: Emission rate and location for the center of emission sources (S1 to S5) for shallow and deep cases. The z value for shallow and deep cases are 50 and 250 [m] from bottom of the pit, respectively, in a terrain-following coordinate system.

Sources	Locations (x, y) [m]	Emission Rate [kg s^{-1}]
S1	(5500, 3900)	1
S2	(5200, 3000)	1
S3	(5100, 2500)	1
S4	(5200, 2300)	1
S5	(6400, 3000)	1

required data for the surface and upper air stations in CALMET. The wind field data at 10 [m] and 1300 [m] above the surface in the terrain-following coordinates are extracted from the CFD model to be used as the surface and upper air stations, respectively. No precipitation and cloud cover are assumed for the simulations. For all the six set of simulations, three upper air stations are considered and located in a terrain-following coordinates at $(x$ [m], y [m], z [m]) of (3000, 3000, 1300)-west station, (5800, 3000, 1300)-mine station, and (8500, 3000, 1300)-east station, which can be seen with blue triangles in Figure 2.9. Radius of influence of terrain features, which is a function of the dominant scale of the terrain is suggested by Scire et al. (2000) [123] to be 5 to 10 times of the grid spacings wide and large enough to cover topographical changes in the domain. In the present simulations, as the mines width are 2 [km] and the grid spacing is 250 [m], the radius of influence of terrain features is set to be 2 [km] for all the cases. $RMAX1$, $RMAX2$, $R1$, and $R2$ are different from case to case and defined based on the number and location of surface stations inside the domain in a way that the combination of all surface stations radii of influences cover the domain completely.

One hundred sixty nine (169) discrete concentration receptors at 10 [m] above the ground in a terrain-following coordinate system, outside and downstream of the mine (from 6500 [m] to 9500 [m] in x -direction and 2000 [m] to 4000 [m] in y -direction) were placed to record the methane concentration for the model validation purposes (blue pluses in Figure 2.9). The discrete receptors are distributed homogeneously in the horizontal direction by a distance of 250 [m] by 250 [m] from each other. The location and number of the discrete receptors in CALPUFF and CFD-LS simulations are exactly the same. Note that in the LS model the number of particles in unit volume are related to the corresponding methane concentration in CALPUFF. For the wind field validation purposes, 26 points outside the mine at 10 [m] above the surface and 15 points inside the mine at 10 [m] above the surface are selected (red dots in Figure 2.10). Also, two vertical columns of receptors from 10 [m] above the surface up to the top of the domain are defined at $(x=5800$ [m], $y=3000$ [m]) and downstream at $(x=8500$ [m], $y=3000$ [m]) to record data in the vertical direction for the purpose of wind field validation throughout the depth the ABL (yellow stars in Figure 2.10).

The simulations investigate the effects of the number of surface stations on the generated wind field. The number of surface stations is changed inside and outside of the mine from a high resolution case with 24 and 95 surface stations inside and outside the mine, respectively, to a low resolution case with only one surface station outside the mine. The seven cases with defined surface stations are summarized in Table 2.7. Case C1 is called the high resolution

case as it has the highest number of surface stations inside and outside of the mine, and case C6 is called the operational case as the number of surface stations inside and outside of the mine are close to industrial monitoring practices for wind measurements. For each simulation scenario the wind and concentration fields are compared with the CFD-LS results.

Table 2.7: The number of surface stations inside and outside the mine for meteorological forcing of the CALMET model.

Case No.	Number of surface stations	
	Inside Mine	Outside Mine
C1 (High Resolution Case)	24	95
C2	24	12
C3	8	4
C4	1	95
C5	1	12
C6 (Operational Case)	1	
C7	0	1

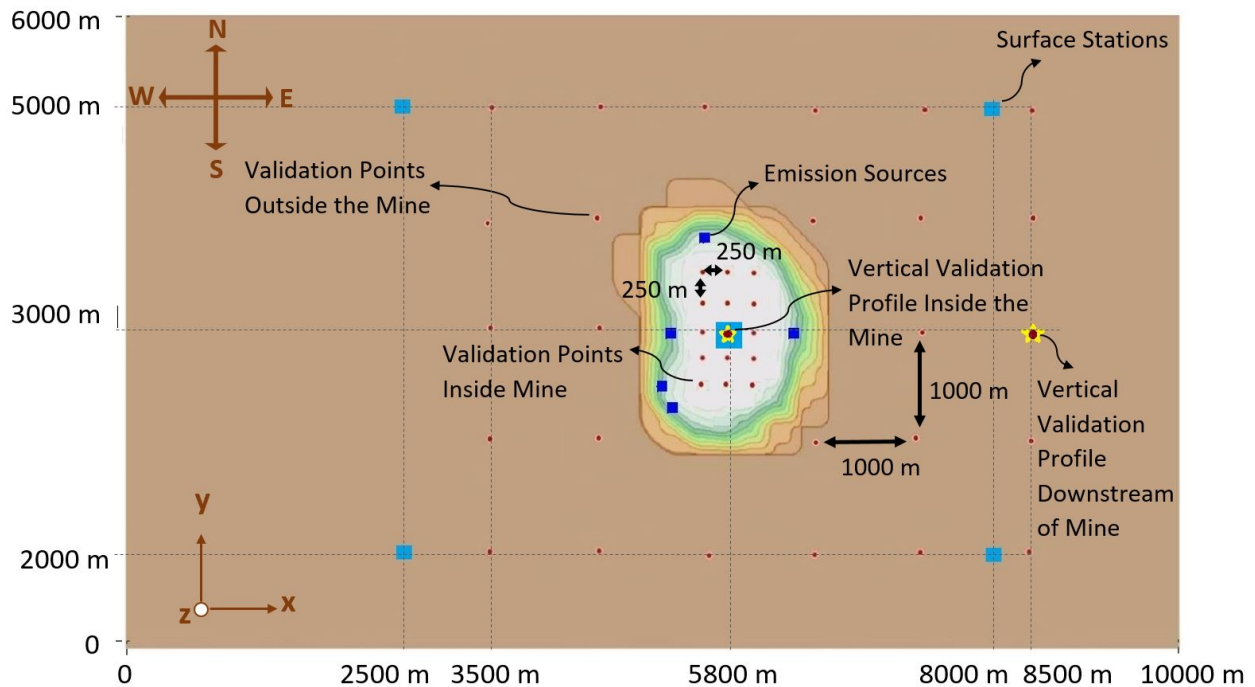


Figure 2.10: Arrangement of surface and upper air stations associated with the operational case C6; location of the validation points for wind field modeling using CALPUFF.

The operational case C6 is pursued further to investigate the effects of changing the location of surface stations. For this purpose, the locations of the surface stations outside

the mine at upstream and downstream sides are changed in the x -direction for four additional cases. The x -location of the four cases are $x = 1000, 8000$ [m], $x = 3000, 7000$ [m], $x = 3000, 8000$ [m], and $x = 3000, 9000$ [m]. The results of the simulations are compared with the concentration and wind fields from the CFD-LS results.

The effects of changing the location of concentration receptors outside the mine are studied for the operational case C6. For this purpose, seven arrays of discrete receptors at $x=6500, 7000, 7500, 8000, 8500, 9000,$ and 9500 [m] (from the east edge of the mine to the end of the computational domain) are selected to compare the concentration at each array with CFD-LS concentration at the same location of receptors at 10 [m] above surface.

Table 2.8 shows the summary of measurement and model development activities that supported this thesis.

Table 2.8: The field measurement and model development activities that supported this thesis.

Task	Performed/Developed by
SODAR	Author
TANAB-SODAR	AIR laboratory members and author
Ultrasonic Anemometers	University of Alberta
VLES at Tunnel Scale	AIR laboratory members
VLES at Field Scale	Author
CALPUFF View	Lakes Environmental Software

2.5 Statistical Analysis

Quantitative comparisons between the simulation (M_i) and reference (O_i) datasets are performed by determining the Bias and Root Mean Square Error (RMSE) defined by

$$Bias = \frac{\sum_{i=1}^n (M_i - O_i)}{n}, \quad (2.43)$$

$$RMSE = \sqrt{\frac{\sum_{i=1}^n (M_i - O_i)^2}{n}}, \quad (2.44)$$

where n is the number of data accounted for in the error statistic calculation. Because wind direction is a circular variable, differences of wind direction between the simulation results and the validation data set are reported as a positive number less than 180° by calculating the Mean Absolute Error (MAE) (instead of Bias) [31, 95]

$$MAE = \frac{\sum_{i=0}^n |M_i - O_i|}{n}. \quad (2.45)$$

To assess the spatial distribution of the predicted concentration field, another statistic is used. The fraction of receptor points that predict the concentration within a factor of two of the reference dataset is termed *FAC2* and defined by Hanna et al. (1993) and Wang et al. (2008) [53, 139]

$$FAC2 = \text{fraction of data for which } 0.5 \leq C_M/C_O \leq 2, \quad (2.46)$$

The *FAC2* statistical metric helps decide if an air pollution dispersion model provides acceptable results. For example, for modeling of air pollution dispersion over complex terrain (e.g. urban areas), Hanna and Chang (2011) [52] suggest that a model performance in complex urban environments is acceptable if *FAC2* is greater than about 30%. This is a more relaxed cutoff than suggested for models of dispersion over homogeneous terrain. Likewise, *FAC5* or *FAC10* can be defined as the fraction of receptor points that predict the concentration within a factor of five or ten of the reference dataset, respectively.

Chapter 3

Results and Discussion

In this chapter, first, the CFD results are validated and verified against observations of wind speed and temperature. In the next step the spatial variability of fields and surface-layer profiles are presented. Then the comparison of the CALPUFF simulation results against the CFD-LS model is presented by visualization of the plume for both models. The results of different CALPUFF weather station setups as well as investigation of the effect of the number and location of met stations are presented. Finally, the concentration agreement versus downwind receptor locations and implications are presented.

3.1 CFD

3.1.1 Comparison Against Observations

Table 3.1 shows the values selected for friction velocity u_* [m s^{-1}] and Obukhov length L [m] from the observation to compare the CFD simulations to field observations taken at the actual mine site. The predictions of the CFD model are shown for profile P3 as a representative upstream location that is far enough from the inlet (for flow to adapt to surface layer characteristics) and far enough from the edge of the mine (for flow not to be influenced by the structure of the flow in the mine). Overall, the agreement between CFD results and the field observations is better for the shallow mine in comparison to the deep mine. The lower level of agreement for the deep mine is due to more complex flow patterns and will be investigated further in the subsequent analysis.

Figures 3.1, 3.2, and 3.3 show the upstream vertical profiles of mean horizontal wind speed and potential temperature as measured by the observations and predicted by CFD

Table 3.1: Friction velocity and Obukhov length: observed and predicted by CFD on profile P3; data reported for shallow and deep mine cases; data reported under various thermal stability conditions.

Mine Type		Observed	CFD (P3)
Thermally-unstable			
Shallow	$u_{*,10\text{ m}}$ [m s^{-1}]	0.25	0.29
	$L_{10\text{ m}}$ [m]	-11.00	-11.60
Deep	$u_{*,10\text{ m}}$ [m s^{-1}]	0.25	0.33
	$L_{10\text{ m}}$ [m]	-11.00	-27.18
Thermally-neutral			
Shallow	$u_{*,10\text{ m}}$ [m s^{-1}]	0.46	0.46
	$L_{10\text{ m}}$ [m]	-	-
Deep	$u_{*,10\text{ m}}$ [m s^{-1}]	0.46	0.52
	$L_{10\text{ m}}$ [m]	-	-
Thermally-stable			
Shallow	$u_{*,10\text{ m}}$ [m s^{-1}]	0.12	0.26
	$L_{10\text{ m}}$ [m]	9.00	9.36
Deep	$u_{*,10\text{ m}}$ [m s^{-1}]	0.12	0.23
	$L_{10\text{ m}}$ [m]	9.00	31.45

simulations under the thermally-unstable, neutral, and stable conditions, respectively. Note that for the thermally-neutral case, the potential temperature is uniform everywhere in the domain, so it is not plotted. Table 3.2 shows the Bias and RMSE of mean horizontal wind speed and potential temperature calculated for CFD versus observations. It must be noted that both the TANAB and SODAR instruments sampled the atmosphere over finite times, typically about 30-60 [min] for each record [96]. The finite temporal averaging has resulted in some scatter in the observation data for each profile. Therefore, these profiles should be studied for their bulk estimates of potential temperature and wind speed. Obtaining smooth profiles from these measurements would have required analysis of larger datasets for temporal averaging over multiple records meeting the same pair of friction velocity and Obukhov length values. However, due to the limited dataset, this was not possible. Nevertheless, the bulk measures of the atmospheric variables serve as a basis for the evaluation of the CFD model.

For the thermally-unstable case (Figure 3.1), the agreement between observations and CFD in potential temperature profiles can be examined using Bias (RMSE) for the shallow and deep mines as 0.04 (0.18) and -0.11 (0.17) [K], respectively, corresponding to profiles P1 to P3. The agreement in the horizontal wind speed profiles can be reported using Bias

(RMSE) for the shallow and deep mines as 0.35 (0.70) and 0.60 (0.78) [m s^{-1}], respectively, by taking the average of error statistics using the TANAB and SODAR datasets as corresponding to profiles P1 to P3. From the plots, wind speed profile P5 in the deep mine case deviates from the rest of the profiles. Profile P5 is the closest profile to the mine, and it is the most affected by modification of the flow structure in the mine (mainly circulation of flow). The alteration of the flow structure in the mines will be discussed in subsequent sections in detail. For the thermally-neutral case (Figure 3.2), the agreement in the horizontal wind speed profiles predicted by CFD versus the observations can be reported using Bias (RMSE) for the shallow and deep mines as 0.21 (0.71) and 0.19 (0.53) [m s^{-1}], respectively, corresponding to profiles P1 to P3. It can be seen that the presence of the mines and the alteration of the flow structure in the cavity influences the horizontal wind speed profiles closer to the mines (P3-P5). For the thermally-stable case (Figure 3.3), the agreement between observations and CFD in potential temperature profiles can be reported using Bias (RMSE) for the shallow and deep mines as 0.28 (0.35) and 0.13 (0.25) [K], respectively, corresponding to profiles P1 to P3. The agreement in the CFD wind speed profiles versus the observations can be reported using Bias (RMSE) for the shallow and deep mines as 0.60 (1.23) and 0.80 (1.10) [m s^{-1}], respectively, by taking the average of error statistics using the TANAB and SODAR datasets as corresponding to profiles P1 to P3. It appears that CFD overpredicts wind speed in the lower portion of the surface layer. Similar to the thermally-unstable case, in the thermally-stable case the horizontal wind speed profile P5 for the deep mine case is affected more significantly by the structure of the flow in the mine compared to the shallow mine case, so it deviates from other profiles.

Focusing on the CFD results, on average, the Biases for wind speed and the potential temperature upstream of the mine are under 0.70 [m s^{-1}] and 0.2 [K], respectively, which imply that the model has the skill to simulate the mean wind speed and potential temperature in the surface layer reasonably well. The thermally-unstable cases have the lowest Bias and RMSE compared to the thermally-neutral and stable cases. The relative success of LES in simulating convective boundary layers versus thermally-stable boundary layers has been noted in previous studies. In thermally-stable boundary layers, the buoyancy forces caused by thermal stratification have a stabilizing effect on the boundary layer by suppressing turbulent transport specially in the vertical direction [137]. The damping of turbulent motions by thermal stratification results in generally low turbulence levels along with small-scale eddies populating the boundary layer [58]. Most of the successful LES studies of ABL have been conducted on convective boundary layers, which have large energy-containing eddies in the

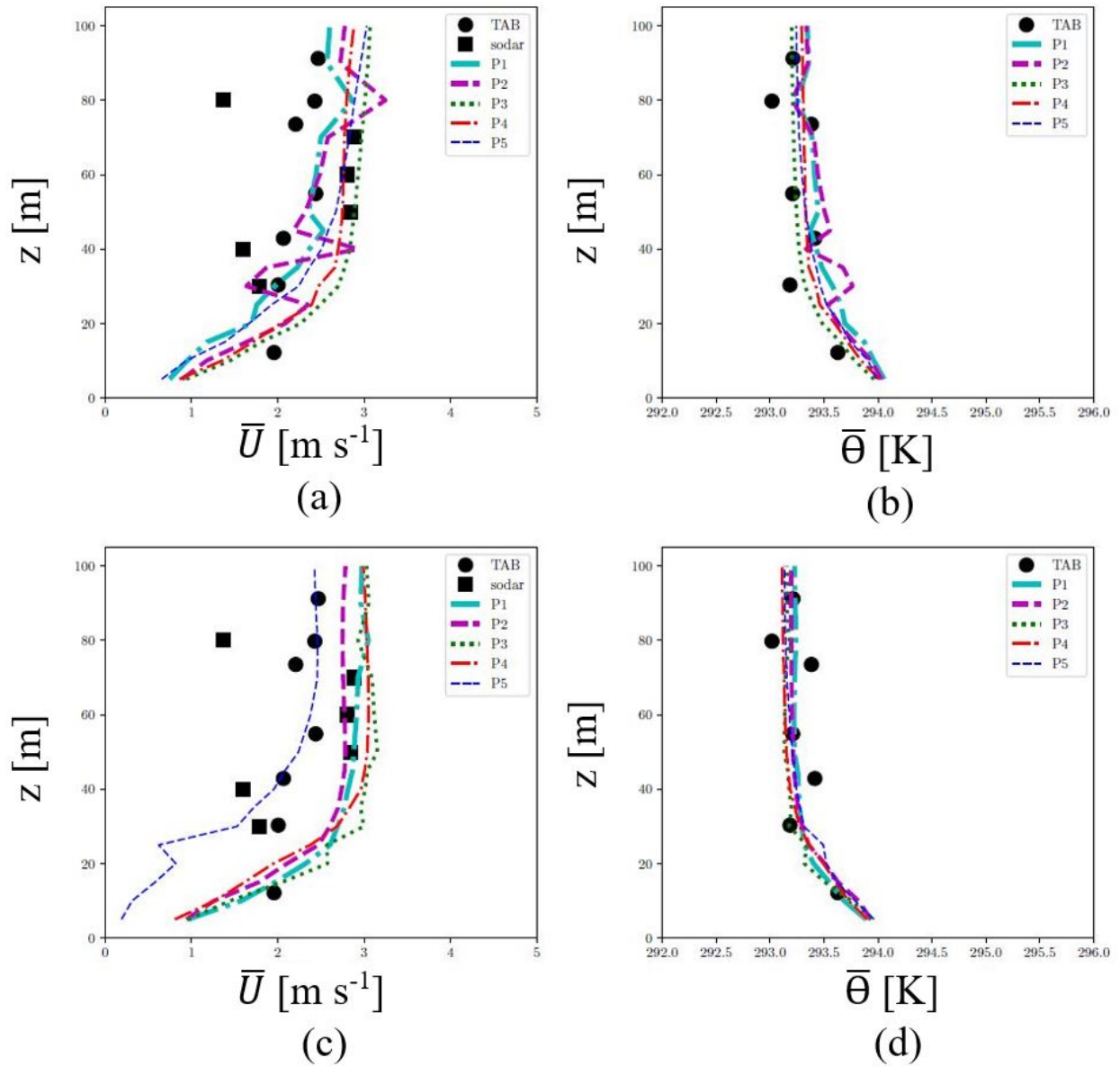


Figure 3.1: Mean horizontal wind speed (\bar{U}) and potential temperature ($\bar{\theta}$) profiles predicted by CFD (P1 to P5) and measured using observations (TANAB (TAB), SODAR) for thermally-unstable shallow (a and b) and deep (c and d) mine cases.

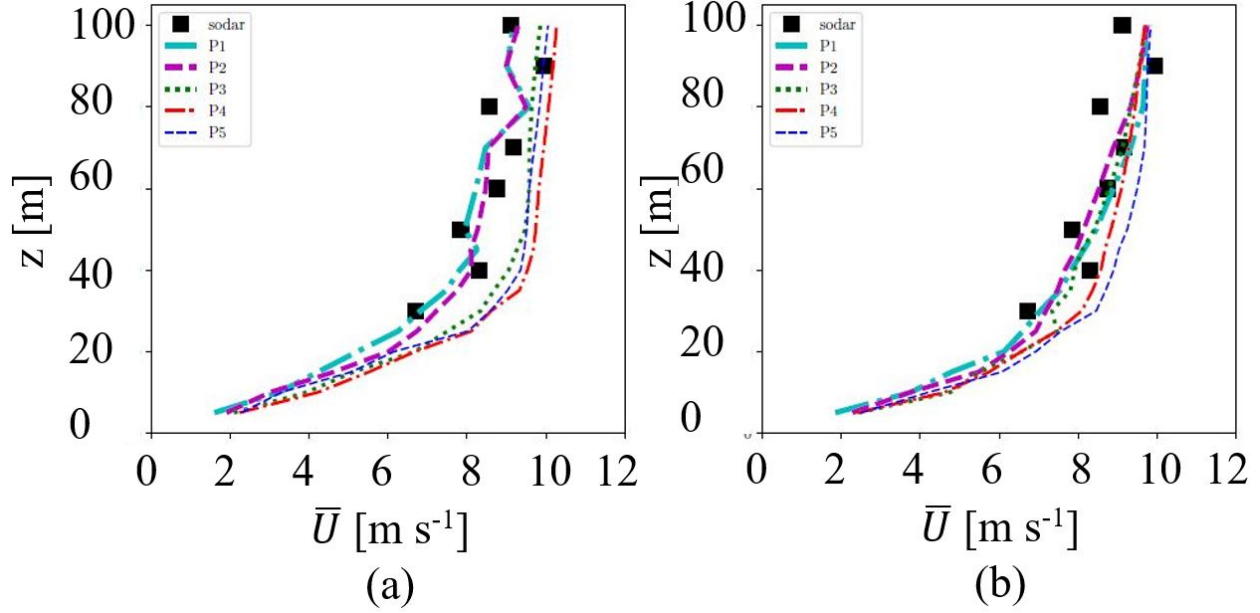


Figure 3.2: Mean horizontal wind speed (\bar{U}) profiles predicted by CFD (P1 to P5) and measured using observations (SODAR) for thermally-neutral shallow (a) and deep (b) mine cases.

order of the size of the boundary layer height [42, 49, 121]. The success of these LES studies is mainly attributed to the dominance of the large-scale turbulent structures in the convective boundary layer [105, 121]. On the other hand, LES of stable boundary layers requires higher grid resolutions and more accurate SGS models to simulate the relatively small boundary-layer turbulence scales reasonably well [58]. This requirement may not be satisfied in practical simulations, possibly explaining the lower level of agreement for the thermally-stable cases simulated here.

3.1.2 Spatial Variability of Fields

Figure 3.4 shows the spatial variability of the wind velocity vectors and magnitude contours. The plots are shown for a vertical slice of the domain through the center of the mine ($y = 3000$ [m]). Skimming flow typically occurs over deep cavities with walls packed close to one another with a small horizontal space between them. Such depressions tend to trap stable vortices and contain pockets of “isolated air”. In such cases, the surface tends to act as if it were aerodynamically smooth [104]. In the skimming flow regime, the fluid flows down the stepped face of the depression as a coherent stream, and mainly skimming over the steps

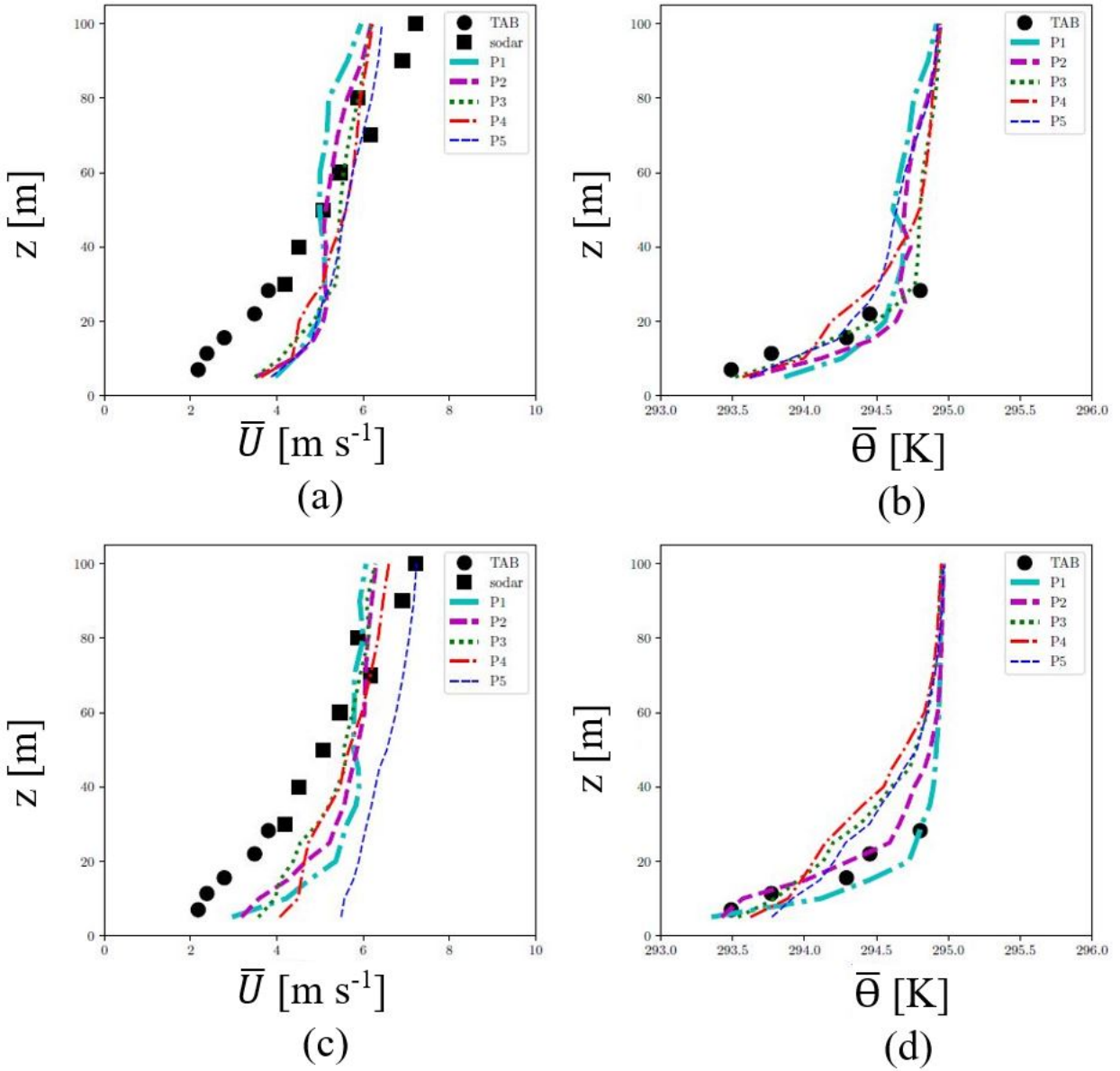


Figure 3.3: Mean horizontal wind speed (\bar{U}) and potential temperature ($\bar{\theta}$) profiles predicted by CFD (P1 to P5) and measured using observations (TANAB (TAB), SODAR) for thermally-stable shallow (a and b) and deep (c and d) mine cases.

Table 3.2: Bias (RMSE) for mean horizontal wind speed (\bar{U}) and potential temperature ($\bar{\Theta}$) calculated for CFD versus observations; data reported for shallow and deep mine cases; data reported under various thermal stability conditions.

Mine Type	Ref. data	P1	P2	P3	P _{avg}
Thermally-unstable					
Shallow	\bar{U} (TAB) [m s ⁻¹]	0.00 (0.42)	0.12 (0.48)	0.41 (0.57)	0.18 (0.49)
	\bar{U} (SODAR) [m s ⁻¹]	0.37 (0.79)	0.44 (0.97)	0.79 (1.00)	0.53 (0.92)
	$\bar{\Theta}$ (TAB) [K]	0.08 (0.18)	0.12 (0.22)	-0.08 (0.15)	0.04 (0.18)
Deep	\bar{U} (TAB) [m s ⁻¹]	0.45 (0.56)	0.27 (0.45)	0.50 (0.68)	0.41 (0.56)
	\bar{U} (SODAR) [m s ⁻¹]	0.80 (1.01)	0.63 (0.89)	0.93 (1.09)	0.79 (1.00)
	$\bar{\Theta}$ (TAB) [K]	-0.11 (0.17)	-0.11 (0.17)	-0.11 (0.17)	-0.11 (0.17)
Thermally-neutral					
Shallow	\bar{U} (SODAR) [m s ⁻¹]	-0.21 (0.56)	-0.02 (0.53)	0.86 (1.03)	0.21 (0.71)
Deep	\bar{U} (SODAR) [m s ⁻¹]	0.25 (0.55)	0.09 (0.52)	0.22 (0.52)	0.19 (0.53)
Thermally-stable					
Shallow	\bar{U} (TAB) [m s ⁻¹]	1.69 (1.71)	1.77 (1.79)	1.54 (1.56)	1.40 (1.69)
	\bar{U} (SODAR) [m s ⁻¹]	-0.41 (0.88)	-0.20 (0.69)	0.00 (0.73)	-0.20 (0.77)
	$\bar{\Theta}$ (TAB) [K]	0.33 (0.44)	0.33 (0.37)	0.18 (0.25)	0.28 (0.35)
Deep	\bar{U} (TAB) [m s ⁻¹]	1.69 (1.75)	1.29 (1.30)	1.22 (1.25)	1.40 (1.43)
	\bar{U} (SODAR) [m s ⁻¹]	0.25 (0.92)	0.26 (0.78)	0.12 (0.60)	0.21 (0.77)
	$\bar{\Theta}$ (TAB) [K]	0.36 (0.39)	0.04 (0.09)	-0.01 (0.28)	0.13 (0.25)

and cushioned by the recirculating fluid trapped between the faces of the depression. Also, the energy dissipation in the flow appears to be enhanced by the momentum transfer to the recirculating fluid [108]. In the current simulations, the skimming flow over the mine is only predicted under the thermally-neutral condition. In this case flow circulations are predicted inside the mine, but they do not influence the flow structure outside the mine significantly. This is in agreement with another CFD study of a deep mine under thermally-neutral conditions by Flores et al. (2014) [39] (their Figure 3a).

Under thermally-unstable or stable conditions many complexities in the flow structure are noted by the present simulations. Under the thermally-unstable conditions, flow circulations are observed for both the shallow and deep mines although the circulation pattern is more effective for the deep mine. Further the circulation pattern inside the mine influences the flow structure outside the mine, in agreement with CFD study of Flores et al. (2014) [39] (their Figure 3e). Such flow patterns result from topographical changes in the land, as they were simulated using the Weather Research Forecasting (WRF) model by Nahian et al. (2020) [95] (their Figure 7f) in a mine field comparable to the shallow mine. Under thermally-stable conditions similar circulations were simulated by Nahian et al. (2020) [95] (their Figure 7e) and observed in a real earth depression comparable to the deep mine by Clements et al. (2003) [26] (their Figure 11). Under the thermally-stable conditions, the wind speed inside the shallow mine is reduced compared to the surroundings. This is in agreement with simulations of Nahian et al. (2020) [95] (their Figure 7e). The meteorological conditions of such depressions are understood to be influenced by modified topography, loss of advective momentum transfer with the surrounding atmosphere, and reduced turbulent sensible heat flux at the bottom of the mine [26, 140]. Under the thermally-stable conditions, the wind speed inside the deep mine is enhanced compared to the surroundings due to the formation of a standing wave. This is in agreement with observations in a real earth depression comparable to the deep mine by Lehner et al. (2016) [73] (their Figures 2 and 10). They observed that the flow across the deep earth depression generates a deep wave in the lee side of the depression, transporting warm air from aloft down into the depression, while typically producing only a small disturbance to the stable air mass in other parts of the depression. This wave further causes a rising structure of air from the bottom of the depression upward into the atmosphere even beyond the surface layer above grade (> 200 [m]).

Figure 3.5 shows the spatial variability of the passive scalar field according to thermal stability conditions and mine depth. The dispersion patterns are a direct consequence of flow fields shown in the previous figure. Again, only under the thermally-neutral condition,

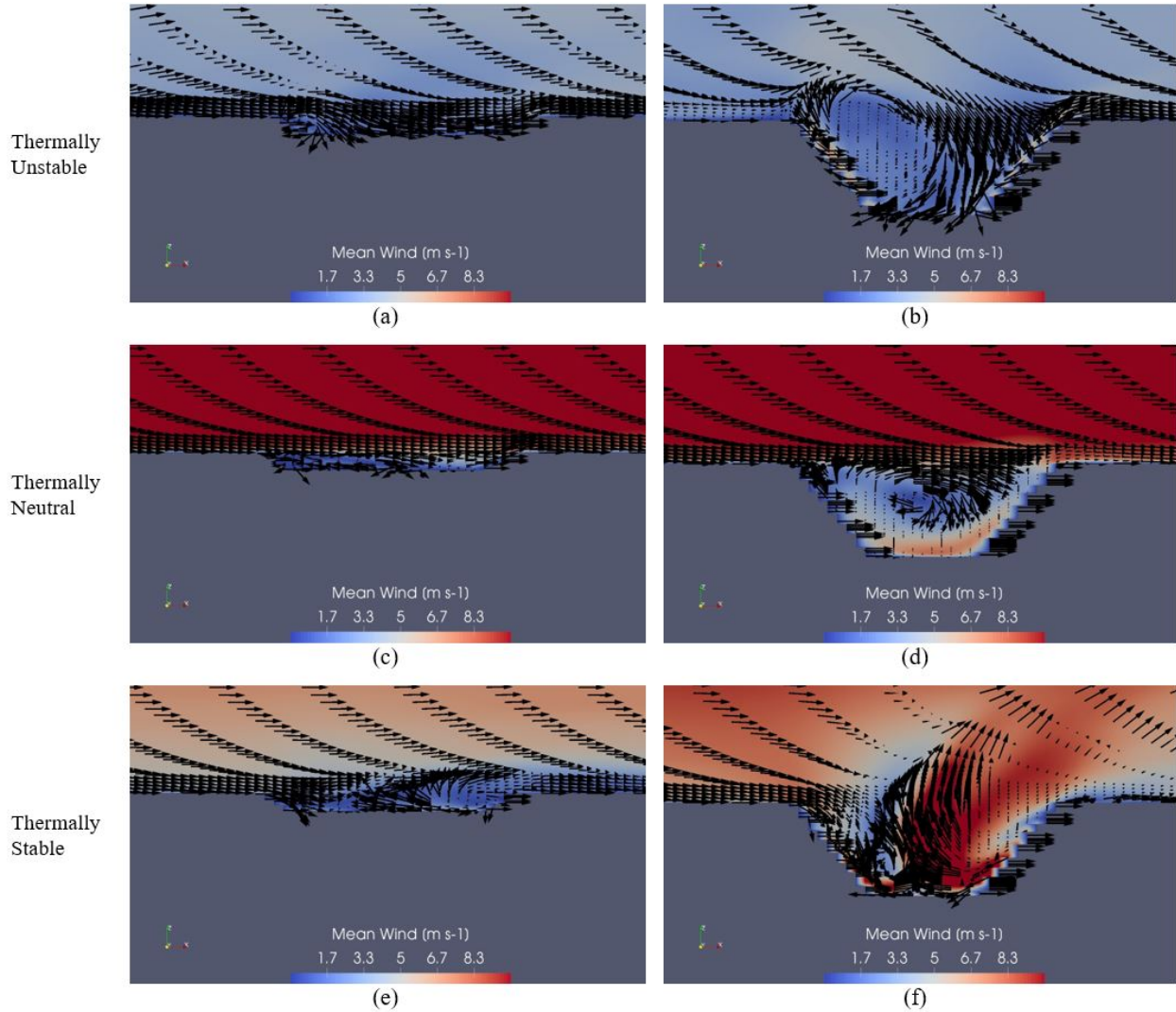


Figure 3.4: Wind field velocity vectors and magnitude contours for thermally-unstable (a and b), thermally-neutral (c and d), and thermally-stable (e and f) cases for the shallow (a, c, e) and deep (b, d, f) mines.

skimming flow is predicted, where the passive scalar circulates inside the mine and then exits downstream as a vertically thin plume confined to elevations below the top of the surface layer (< 200 [m]), which is in agreement with the CFD study of Flores et al. (2014) [39] (their Figure 7a).

For the thermally-unstable case, propagation of the passive scalar upstream and upward is predicted. In the thermally-unstable case due to turbulent vertical mixing downstream of the mine, the plume exits the mine as a thick layer reaching altitudes up to and beyond 1000 [m] within the ABL. In the deep plume at the downwind edge of the mine, due to the large standing vortex in the mine that transports tracer to large heights, the plume rise is more significant for the deep mine than the shallow mine. Simulations of Flores et al. (2014) [39] (their Figure 7e) reveal similar dispersion patterns, in comparison to the neutral case, where the plume rise in the atmosphere is more significant. Aircraft observations of Gordon et al. (2015) [46] for a real mine representing the shallow mine here also revealed that under thermally-unstable conditions, the plume can rise up to a significant portion of the ABL.

For the thermally-stable case, the plume dispersion phenomenon is different for the shallow and deep mines. For the shallow mine, a thin vertically shallow plume is predicted downstream of the mine, which is confined within the surface layer, in agreement with WRF simulations of Nambiar et al. (2020) [97] (their Figure 7) for a real mine comparable to the shallow mine in this study. However for the deep mine, a vertical rise of the plume is predicted at the center of the mine as a direct consequence of the standing wave. In contrast to the thermally-neutral case, this causes a deep plume within a substantial portion of the ABL downstream of the mine.

Figure 3.6 shows the horizontal pattern of the passive scalar and velocity fields over a horizontal slice at 10 [m] above grade (not terrain following). In fact Figures 3.4 to 3.6 show the complex three dimensionality of the flow field in the present simulations, which reveal the value of CFD simulations in helping understand atmospheric transport. The wind speed at 10 [m] above grade is much lower under thermally-unstable condition than the thermally-neutral and stable conditions. Lower wind speeds under unstable conditions are likely due to the presence of a well-mixed convective surface layer, characterized by a near-constant distribution of wind speed with height due to strong vertical mixing [62]. The high wind speed under stable conditions may be due to sharp vertical gradients in the wind speed in the surface layer, which is typically due to suppressed vertical mixing and has been well documented in the literature [84, 98]. The top view of the wind velocity vectors and passive scalar field show distinct spatial patterns. Horizontal wind circulations inside the mine can

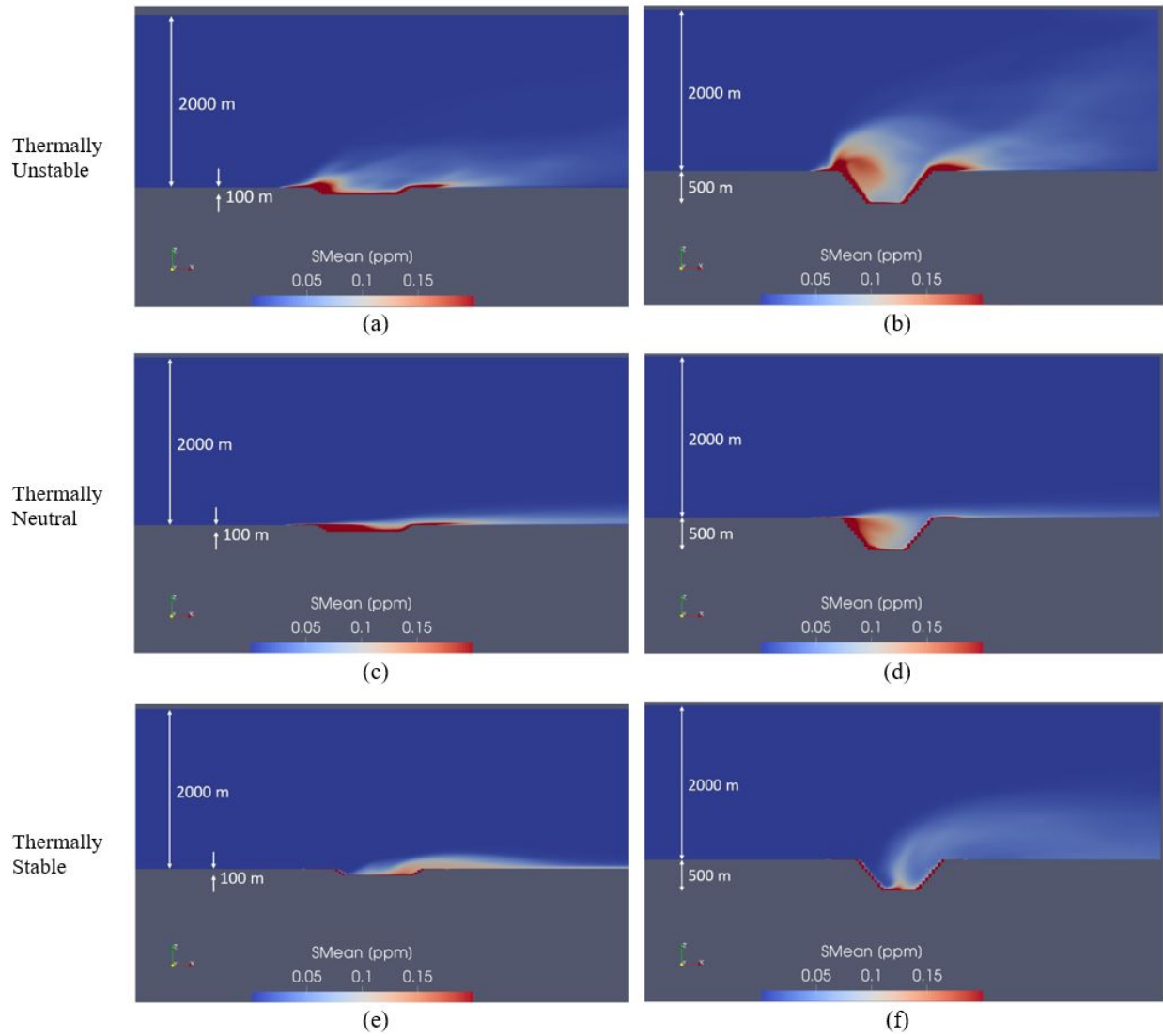


Figure 3.5: Passive field contours for thermally-unstable (a and b), thermally-neutral (c and d), and thermally-stable (e and f) cases for the shallow (a, c, e) and deep (b, d, f) mines.

be noted under all configurations but are particularly accentuated with the deep mine under the thermally-stable case. Such horizontal circulations were also noted by Nahian et al. (2020) [95] for an enclosed earth depression using WRF simulations (their Figures 7e and 7f). Under the thermally-unstable and neutral cases, large passive scalar values appear as a ring surrounding the mine edge in all directions, possibly due to strong vertical mixing, vertical circulations, and slope flows along the mine walls. However, under the thermally-stable case, such rings are not formed, but the plume is displaced out of the mine via the standing wave in the downstream direction. This transport mechanism is more noticeable for the shallow mine since the wave for the deep mine transports the plume higher in the surface layer, so that it would not be probed at 10 [m] above grade. Another interesting note is the asymmetric structure of the flow and passive scalar fields in the span-wise direction despite the symmetry of the topography in that direction. Such a feature was also noted by Flores et al. (2014) [39], who showed the asymmetry of plume dispersion for a symmetric circular mine (their Figures 6 and 7).

3.1.3 Surface-Layer Profiles

Figure F.1 shows the profiles of normalized mean x -component wind velocity outside (P3 to P10) and inside (P11 to P13) the shallow and deep mines. For this normalization the friction velocity at 10 [m] altitude on P3 is chosen. The velocity component increases downstream of the mine in the lower portion of the surface layer ($z < 50$ [m]), in agreement with the observations of Nahian et al. (2020) [95] (their Figure 5a), who measured enhanced up-slope winds over the edge of a mine comparable to the shallow mine. Examining the profiles inside the mine (P11 to P13), it can be seen that for the shallow mine, back flows (or circulations) occur under most thermal stability conditions, where $\overline{U}_x < 0$ [m s⁻¹] on one or more of such profiles. Such circulations have been also predicted by Nahian et al. (2020) [95] (their Figure 7e). On the other hand, back flow is predicted to enhance for the deep mine case. Similar back flow conditions were predicted by simulations of Flores et al. (2014) [39] in a deep mine under the thermally-neutral and unstable conditions (their Figures 3a and 3e).

Figure F.2 shows the profiles of normalized mean z -component of the wind velocity outside (P3 to P10) and inside (P11 to P13) the shallow and deep mines. The most notable mean advective flow in the vertical direction is associated with the deep mine under the thermally-stable conditions. The vertical motion is best described by the standing wave formation. Here on the lee side of the mine (P11) warm air is transported from aloft toward

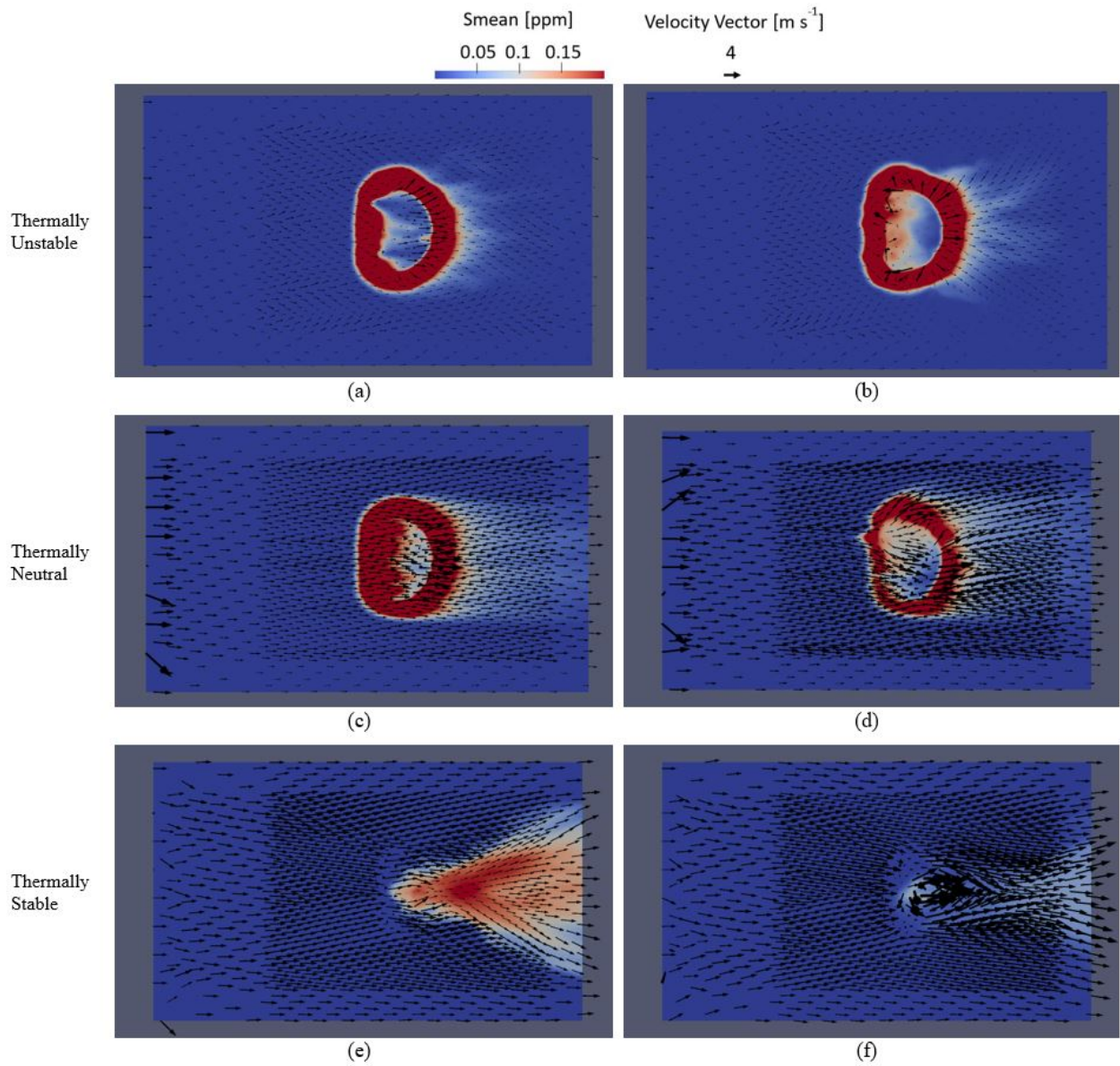


Figure 3.6: Wind field velocity vectors and passive scalar contours for thermally-unstable (a and b), thermally-neutral (c and d), and thermally-stable (e and f) cases for the shallow (a, c, e) and deep (b, d, f) mines on a horizontal cross section at 10 [m] above grade.

the bottom of the mine ($\overline{U}_z < 0$ [m s⁻¹]), while the rising flow due to this standing wave is notable on the center of the mine (P12), wind side of the mine (P13), and downstream of the mine (P6) ($\overline{U}_z > 0$ [m s⁻¹]). A similar flow structure was observed by Lehner et al. (2016) [73] (their Figures 2b and 10) associated with a natural earth depression comparable to the deep mine. Clements et al. (2003) [26] and Lehner et al. (2016) [73] characterized the wave in such a way that areas of strong wind are remained relatively confined, with comparatively weak wind speeds above the descending flow and quiescent conditions in the center of the mine below the wave crest (Figure 10 in Lehner et al. (2016) [73]).

Figure F.3 shows the change in potential temperature profiles from the surface outside (P3 to P10) and inside (P11 to P13) the shallow and deep mines. In the upstream of the mine, the thermally-unstable ($\partial\overline{\Theta}/\partial z < 0$ [K m⁻¹]), neutral ($\partial\overline{\Theta}/\partial z \sim 0$ [K m⁻¹]), and stable ($\partial\overline{\Theta}/\partial z > 0$ [K m⁻¹]) conditions can be distinguished near the surface ($z < 25$ [m]). However, inside and downstream of the mine the profiles of the mean potential temperature become more uniform, particularly under the thermally-stable conditions. This is indicative of turbulent and advective mixing in these regions, which result in more uniform distribution of potential temperature in the vertical direction. The tendency of the formation of the isothermal layer is hypothesized to be due to air circulations and mixing inside the mine and air incursions across the depression edge [141]. Particularly during the thermally-stable conditions, similar potential temperature profiles were observed by Nahian et al. (2020) [95] (their Figure 5b), Clements et al. (2003) [26] (their Figures 5, 8, and 9), Whiteman et al. (2008) [141] (their Figure 10), and Lehner et al. (2016) [73] (their Figure 8).

The normalized mean passive scalar mixing ratio profiles outside (P3 to P10) and inside (P11 to P13) the shallow and deep mines are presented in Figure F.4. In agreement with Figure 3.5, under thermally-unstable and neutral cases the flow structure in the mine causes a back flow so that the passive scalar is transported upstream, and it is detected on P5. The back flow is the direct consequence of flow circulation inside the mine closer to the lee side, where $\overline{U}_x < 0$ [m s⁻¹] on P11 in Figure F.1. Under the thermally-stable conditions, however, no propagation of the passive scalar is predicted upstream. On the downstream side of the mine several features can be noted. Under the thermally-neutral case, simulations for both the shallow and deep mines show a thin passive scalar plume limited to the lower part of the surface layer ($z < 25$ [m]) on P6, which is diluted on the subsequent profiles. This is the artifact of the skimming flow. Under the thermally-unstable case, the deep mine simulations show greater level of mixing so that the plume reaches higher in the surface layer on P6. For both the shallow and deep mines the plume is diluted on the subsequent profiles due

to enhanced mixing downstream of the mines. The most interesting feature is the structure of the plume downstream of the mines under the thermally-stable conditions. In agreement with Figure 3.5, for the shallow mine, the plume is predicted to rise at a short distance downstream of the mine ($\overline{U}_z > 0$ [m s⁻¹] on P6 in Figure F.2) to cover the majority of the surface layer on P6; however, on subsequent profiles, subsiding flow occurs ($\overline{U}_z < 0$ [m s⁻¹] on P8 and P9 in Figure F.2) that cause the plume to be detected only on the lower portion of the surface layer ($z < 25$ [m]) on P8 and P9. For the deep mine, and due to the standing wave transporting the plume above the surface layer downstream of the mine, no indication of the plume is noted on P6 to P10, possibly due to advective transport and turbulent mixing that result in displacement and dilution of the plume upward, respectively.

The profiles of normalized turbulent sensible kinematic vertical heat flux outside (P3 to P10) and inside (P11 to P13) the shallow and deep mines are presented in Figure F.5. Upstream of the mine, the positive heat flux can be noted for the thermally-unstable case and negative heat flux for the thermally-stable case (P3 to P5), which are typical of surface layers over flat and homogeneous lands. Most notably, the mines influence the magnitude and sign of the heat flux under the thermally-stable case. For the shallow mine, it is observed that the magnitude of the negative heat flux is enhanced near the top of the surface layer on profiles P11 and P12. This could be due to formation of a shear layer and enhanced turbulence at this height. The heat flux on the downstream side becomes positive, possibly due to the subsiding of warm air into the mine and its rise downstream. For the deep mine, the presence of the standing wave and its influence on the heat flux can be noted on profile P12. Near the bottom of this profile, the heat flux is positive, due to the subsidence of warm air from aloft that reaches the wave bottom and contributes to an overall warming due to vertical turbulent exchange. Near the top of this profile, the heat flux is negative, due to interaction of the wave crest with cold stream of air above with an overall cooling due to vertical turbulent exchange.

Figures F.6, F.7, and F.8 show the normalized resolved, SGS, and total TKE, i.e. k_{res} , k_{sgs} , and k_{tot} [m² s⁻²], respectively, outside (P3 to P10) and inside (P11 to P13) the shallow and deep mines. Note that the total kinetic energy is the sum of the resolved and SGS parts, i.e. $k_{tot} = k_{res} + k_{sgs}$ [m² s⁻²]. The percentage of k_{res} out of k_{tot} [m² s⁻²] is a critical parameter to evaluate the capability of an LES method to simulate fluctuating eddies and their role in transport phenomena [110]. In economized VLES methods equipped with wall functions, it is acceptable to model a great fraction of k_{tot} [m² s⁻²] near the walls, while typically greater than 60-80% of k_{tot} [m² s⁻²] shall be resolved away from the walls [7]. This

condition is met by the model, where above $z = 25$ [m], most of k_{tot} [$\text{m}^2 \text{s}^{-2}$] is resolved. This pattern can be seen from Figures F.6 and F.7. The fraction of k_{tot} [$\text{m}^2 \text{s}^{-2}$] resolved on profile P8 is calculated, as the flow field is fully developed at this location downstream of the mine where the effects of the mine and thermal stability conditions have been experienced by the flow. For this profile, on average for all three stability conditions for the shallow mine, between 65 and 75% of k_{tot} [$\text{m}^2 \text{s}^{-2}$] is resolved in elevations from $z = 25$ [m] to $z = 50$ [m]. Examining locations above $z = 50$ [m], the simulation results show that even a greater portion of k_{tot} [$\text{m}^2 \text{s}^{-2}$] is resolved. The average fraction of k_{tot} [$\text{m}^2 \text{s}^{-2}$] resolved for the deep mine in all thermal stability conditions is about 90% above $z = 25$ [m].

Focusing on the profiles in Figure F.8, it is noted that in both shallow and deep mine cases, higher levels of k_{tot} [$\text{m}^2 \text{s}^{-2}$] exist inside the pit compared to the outside. This can be an artifact for the presence of sloped flow, circulations, shear layer, and other complex flow phenomena that generate turbulence. Furthermore, the stepped walls of the mine contribute to increasing the surface roughness and turbulence. The enhancement of k_{tot} [$\text{m}^2 \text{s}^{-2}$] inside earth depressions have also been predicted by Silvester et al. (2009) [127] and Aliabadi et al. (2017, 2019, 2021) [3–5]. A higher amount of k_{tot} [$\text{m}^2 \text{s}^{-2}$] is predicted in the deep mine compared to the shallow mine, possibly due to more abrupt topographical changes and enhancement of circulations. Downstream of the shallow mine, and under the thermally-unstable conditions, a local peak for k_{tot} [$\text{m}^2 \text{s}^{-2}$] is predicted on profiles P7 to P9 at about $z = 25$ [m], which is indicative of a shear layer and a local low-level jet caused by topography.

Figure F.9 shows the profiles of normalized advective plus turbulent flux of the passive scalar in the x -direction ($\overline{US} + \overline{us}$) [m s^{-1}] outside (P3 to P10) and inside (P11 to P13) the shallow and deep mines. Under the thermally-unstable and neutral conditions, the back flow caused by the flow circulation in the mines results in a positive flux upstream of the mines on P5 below $z = 15$ [m] in both cases. Inside the deep mine, the formation of a circulation of plume under the thermally-unstable conditions is evident. The circulation pushes the passive scalar toward the mine wall and causes the passive scalar to exit from the lee side (P11) and wind side (P13) of the deep mine. A similar pattern of particle movements inside a deep mine has been predicted by Flores et al. (2014) [39] (their Figures 7c and 7e). The downstream profiles under the thermally-unstable conditions show a thin plume under $z = 40$ [m] for both shallow and deep mines (P6). These results are in agreement with those of Flores et al. (2014) [39], who also showed that in a deep mine, the plume height after the pit is higher under thermally-unstable conditions than the thermally-neutral conditions (their Figures 7a and 7e). Again, due to the standing wave formed for the deep mine under the

thermally-stable condition, no notable flux can be predicted downstream of the mine in the surface layer. The flux is rather distributed over a significant portion of the boundary layer.

Figure F.10 shows the profiles of normalized advective plus turbulent flux of the passive scalar in the z -direction ($\overline{WS} + \overline{ws}$) [m s^{-1}] outside (P3 to P10) and inside (P11 to P13) the shallow and deep mines. The most notable feature here is the impact of the standing wave on the flux for the deep mine under the thermally-stable condition. Here a large component of the vertical flux is predicted at the center of the mine on profile P12. This is due to the rising structure of air that transports the passive scalar vertically out of the mine.

The flow complexities noted here warrant a closer investigation of diagnostic meteorological models based on the Gaussian plume dispersion paradigm. It is expected that the Gaussian plume models yield dispersion results substantially different from those predicted using this CFD analysis, particularly if they attempt to predict dispersion transport over complex terrain with topographical unevenness.

3.2 CALPUFF-CFD-LS

3.2.1 Plume Visualization for CALPUFF and CFD-LS Models

Figure 3.7 shows the contour plots of surface gas concentration for the shallow mine under the three thermal stability conditions, using the CALPUFF case C6 (i.e., four surface stations outside and one inside the mine). Contrasting the two plumes under the unstable condition, it is noted that CALPUFF has enhanced the horizontal dispersion of material downwind of the mine relative to CFD-LS. While the CFD-LS simulations suggest three distinct plume “fingers” immediately downwind of the mine (these fingers roughly correspond to the y -grouping of the sources), in CALPUFF the individual source plumes quickly merge to a single broad plume. Such differences were elucidated in other studies [78, 135]. Under thermally-neutral conditions, the lateral dispersion of tracer in both CFD-LS and CALPUFF is reduced compared to the unstable conditions. With CALPUFF, three plume fingers downwind of the mine can be seen. Under the thermally-stable condition, lateral dispersion is reduced even further. The most striking feature in the stable condition is the large area of zero-concentration downwind of the mine in the CFD-LS model results, and the counter-intuitive trend toward increasing surface concentration with increasing distance downwind of the mine (over at least part of the domain). This behavior was also seen in the earlier study of Kia et al. (2021) [68], and linked to plume rise from the mine.

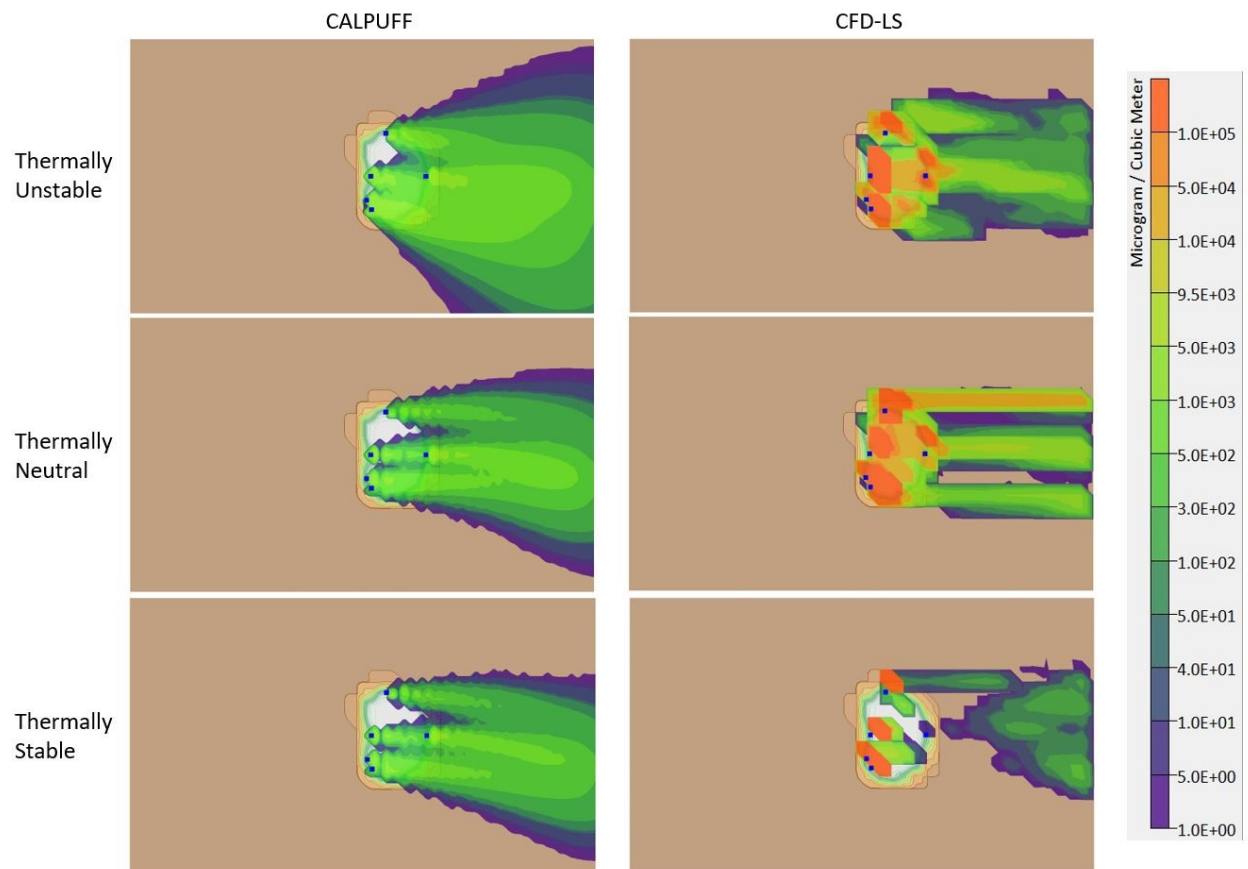


Figure 3.7: Contour plots of surface tracer concentration for the shallow mine case, as predicted from CALPUFF case C6 (left) and CFD-LS (right).

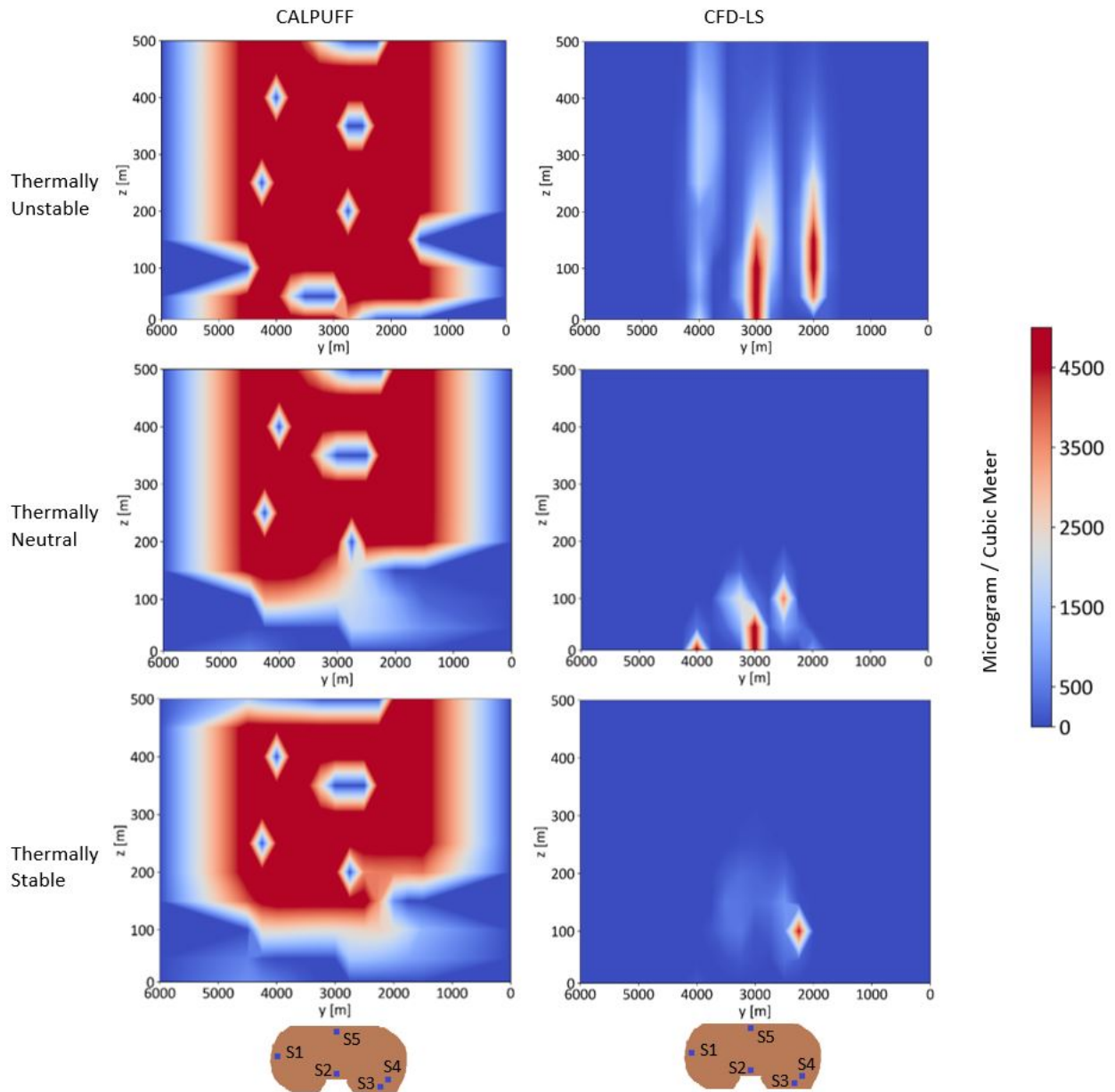


Figure 3.8: Contour plots showing a vertical slice of tracer concentration downwind of the shallow mine ($x=7000$ [m]), as predicted with CALPUFF case C6 (left) and CFD-LS (right). The distribution of sources in the mine is shown below the plots for reference.

Figure 3.8 shows a vertical slice of the CFD-LS and CALMET plumes at a location approximately 500 [m] downwind of the mine ($x = 7000$ [m]). These vertical slices consistently show that CALPUFF simulates a wider plume than does CFD-LS, mirroring what it is noted in the horizontal slices in Figure 3.7. The CALPUFF plumes are also more dispersed in the vertical direction. In the unstable condition, the CFD-LS slice shows the three surface level plume fingers noted in Figure 3.7 exist aloft too. It is interesting that two of the three fingers are elevated, having maximum concentration levels above the surface (this would be unexpected for a ground level source in simple terrain). The unstable CALPUFF plume does not replicate these details. The CFD-LS and CALPUFF plumes are particularly different for the stable condition. The CFD-LS plume slice shows a concentrated “filament” centered at $y = 2220$ [m], $z = 100$ [m], while the CALPUFF plume is dramatically more dispersed. Looking at both the horizontal and vertical CFD-LS plume slices for the stable condition (Figures 3.7 and 3.8), it is speculated that the gas plume from the five mine sources is very concentrated and elevated as it passes over the downwind edge of the mine. The elevated plume explains the absence of surface-level gas just downwind of the mine (a concentration “shadow”). From that initial elevation at the mine edge, the plume slowly mixes down to the surface, resulting in an increase in concentration with increasing distance from the mine. This behavior is not seen in the CALPUFF plume.

3.2.2 Different CALPUFF Weather Station Setups

The CALPUFF plume simulations depend on the setting of the input weather stations, as the number and location of these stations impact the CALMET calculated wind fields. In this section several possible settings of the surface weather stations (Table 2.7) are considered. These cover a range of implementations that could be used in a model application. In the following discussion it is assumed that the CFD-LS model gives the true concentration and wind fields in the various open-pit situations, and it is evaluated what the impact of the CALMET settings are in terms of the statistical agreement between the CALPUFF and CFD-LS concentration and wind fields.

3.2.2.1 Effect of the Number of Met Stations

Figure 3.9 shows the Bias [$\mu\text{g m}^{-3}$] and RMSE [$\mu\text{g m}^{-3}$] of the surface gas concentrations calculated by CALPUFF downwind of the mine. The main conclusions which can be drawn from these figures is the degree to which surface weather station settings impact the accuracy

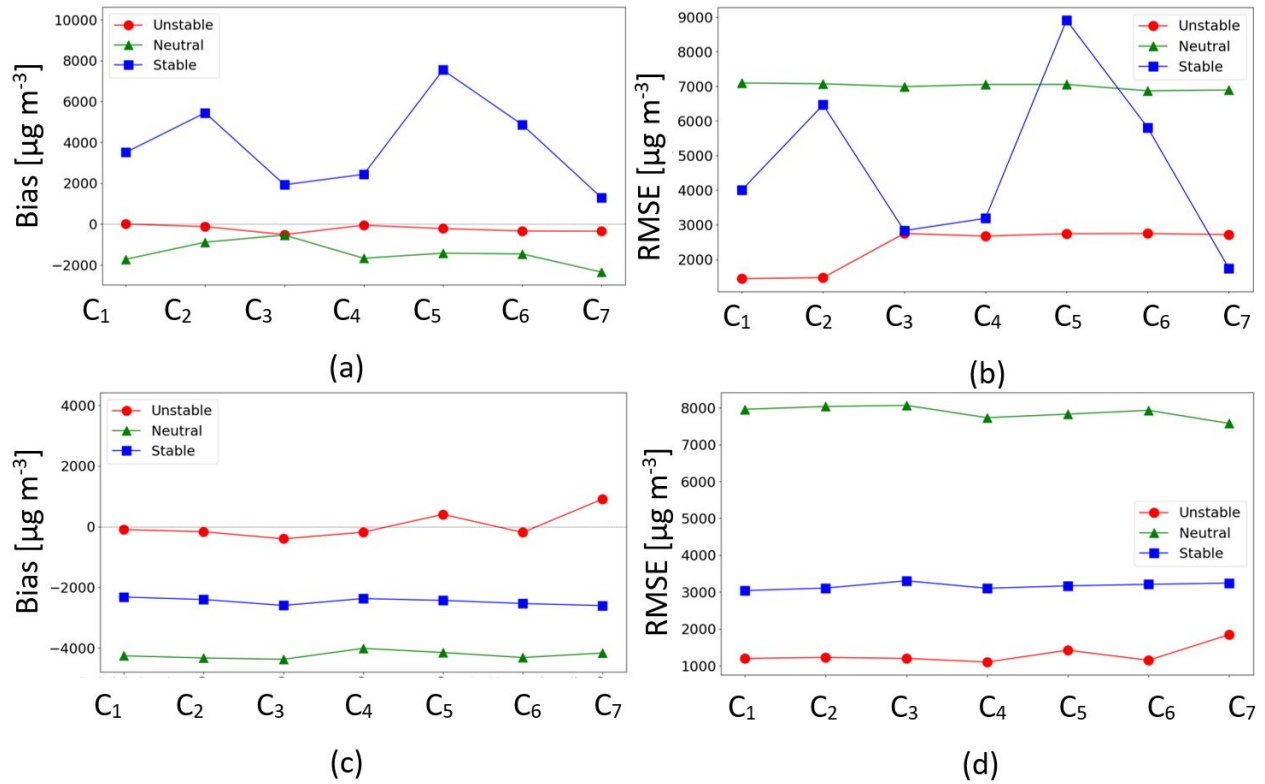


Figure 3.9: Bias [$\mu\text{g m}^{-3}$] and RMSE [$\mu\text{g m}^{-3}$] of the tracer concentrations outside of the mine, comparing CALPUFF predictions against CFD-LS over different number of surface station setting cases and thermal stability conditions of the shallow (a and b) and deep (c and d) mine configurations.

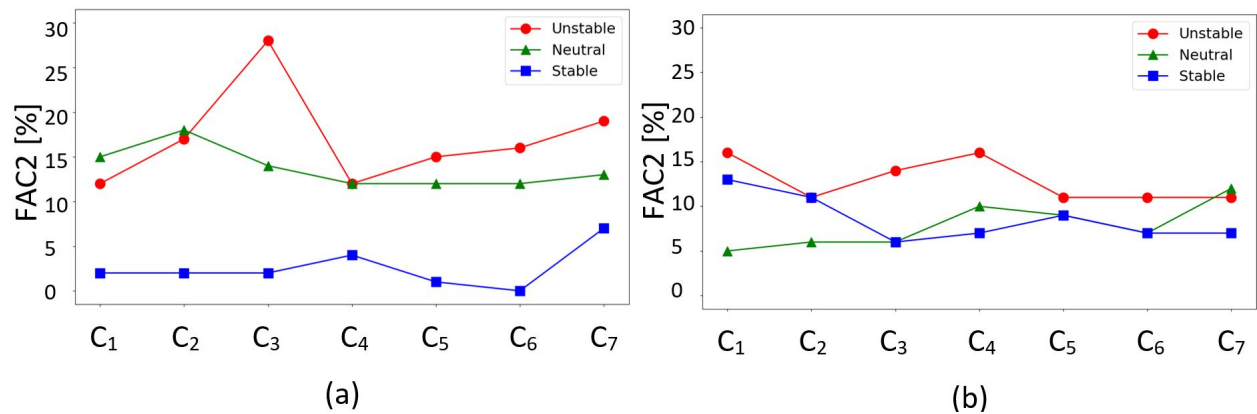


Figure 3.10: FAC2 [%] of the surface tracer concentrations predicted by CALPUFF against the CFD-LS values over the different number of CALPUFF surface station settings and thermal stability conditions for the shallow (a) and deep (b) mine configurations.

of the CALPUFF simulations, and whether it can be identified what conditions would lead to more accurate simulations. One of the hypotheses was that the case having the greatest number of input weather stations (“high resolution” case C1) would provide more accurate predictions. Across the two mines and three stability conditions, there was no clear evidence that the high resolution case C1 gave better predictions in terms of Bias [$\mu\text{g m}^{-3}$]. In terms of RMSE [$\mu\text{g m}^{-3}$], only in the shallow-mine unstable condition did we find that the higher resolution cases (C1 and C2) had lower errors than the other cases. Another hypothesis was that having more weather stations in the mine pit allows a better representation of the flow complexity in CALPUFF, which would result in a better concentration predictions (e.g., case C3 would be better than cases C5 or C6). Having more weather stations in the mine did improve CALPUFF performance in the shallow-mine stable condition, as both the Bias [$\mu\text{g m}^{-3}$] and RMSE [$\mu\text{g m}^{-3}$] values of case C3 were lower than for cases C4-C6. Earlier we discussed the interesting and counter intuitive plume characteristics in the shallow-mine stable condition (elevated and compact plume as it exited the mine), and perhaps this explains why the improvement in the performance of CALPUFF is seen when we added more weather stations in the mine in this case. However, in the five other situations, there is little to recommend to increase the number of weather stations in the mine. Another hypothesis was that the least accurate CALPUFF predictions would occur when only a single weather station was used (case C7). The most surprising result illustrated in Figure 3.9 is that there was no general degradation in CALPUFF performance when only a single weather station is used. Only in the deep mine configuration and under unstable condition did we see a clear decline in performance. In total, we did not observe large sensitivities in CALPUFF performance based on the number of the input weather stations.

Figure 3.10 shows the calculated *FAC2* percentage of receptor concentrations from the various CALPUFF runs. This statistic gives the fraction of receptors (downwind of the mine) where the CALPUFF calculated concentration is within a factor of two of the CFD-LS result. The clearest conclusion one can draw from Figure 3.10 is that for the large majority of downwind locations, the CALPUFF predictions are more than a factor of two different from CFD-LS. In fact this is also true if we look at *FAC10* (not shown), in which the majority of receptors have a concentration that is more than a factor of 10 different from CFD-LS. There are two other conclusions that we can draw from Figure 3.10. In the simulations, the trend was for CALPUFF to overestimate the surface concentrations. Tomasi et al. (2019) [135] compared CALPUFF and LS model concentration predictions for a tracer release study in mountainous terrain. They found a similar trend where CALPUFF overestimated both

the LS model calculations and the actual tracer observations. In addition, the shallow mine configuration under the unstable condition was the only scenario showing sensitivity to the CALPUFF weather station settings. Only in this configuration and condition did we find a case (C3) that gave a large increase in *FAC2* percentage compared with other cases. This is a case with a moderate number of receptors inside the mine.

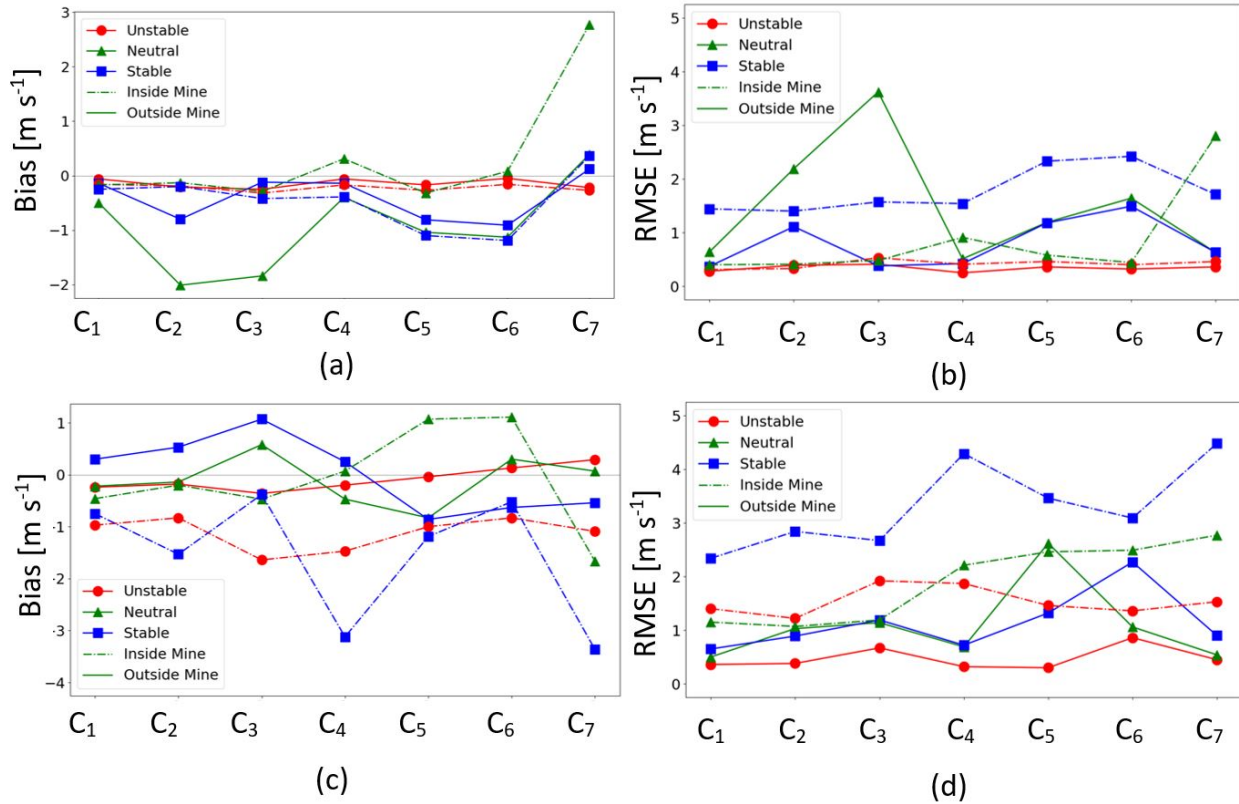


Figure 3.11: Bias [m s⁻¹] and RMSE [m s⁻¹] of horizontal wind speed inside and outside of the mine at 10 [m] above surface, comparing CALMET predictions against CFD-LS over different number of surface station cases and thermal stability conditions of the shallow (a and b) and deep (c and d) mine configurations.

The focus is now shifted to look at how well the wind fields calculated in CALMET recreate the CFD flow fields. Figure 3.11 shows the calculated Bias [m s⁻¹] and RMSE [m s⁻¹] of horizontal wind speeds at discrete receptors located 10 [m] above the surface both inside and outside of the mine. These particular receptors were not used by CALMET to calculate the wind fields. Under the unstable condition, Bias [m s⁻¹] and RMSE [m s⁻¹] values lower than 2 [m] s⁻¹ are achieved for both inside/outside of the mines and shallow/deep mines. However, the error statistics were higher for the neutral and stable conditions, in agreement

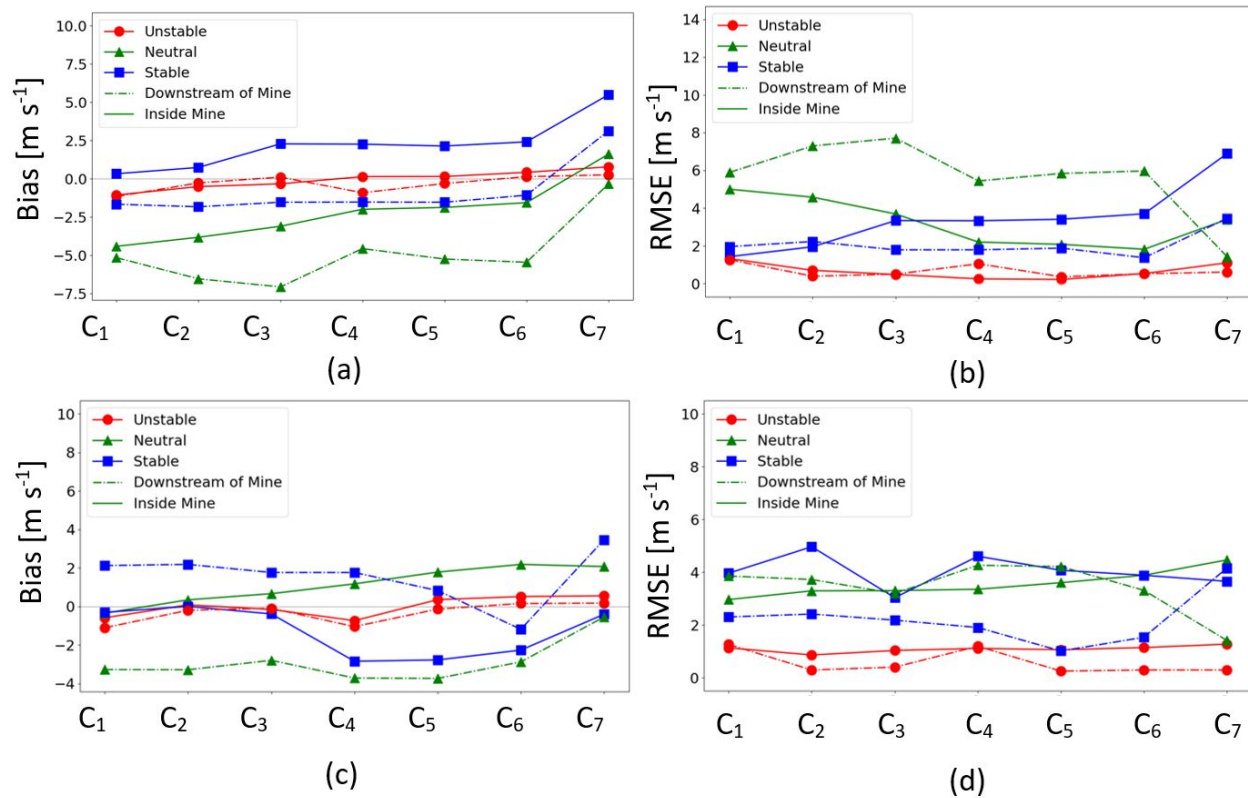


Figure 3.12: Bias [m s⁻¹] and RMSE [m s⁻¹] of horizontal wind speed on vertical boundary-layer profiles inside and downstream of the mine predicted by CALMET against CFD-LS over different number of surface station cases and thermal stability conditions of the shallow (a and b) and deep (c and d) mine configurations.

with a study by Cox et al. (2005) [27] (their Figure 2), who examined evaluation of three diagnostic wind models with data from 26 field experiments. Cases C4 and C6 show the effect of changing the number of surface stations outside the mine (by keeping the number of stations inside the mine constant). The effects are more clear particularly for the stable condition, where for the shallow mine, the wind speed Bias [m s^{-1}] and RMSE [m s^{-1}] are decreased by increasing the number of surface stations from four outside the mine (case C6) to 95 outside the mine (case C4). This may be attributed to a more successful wind field interpolation when more observed station data are included. The Bias [m s^{-1}] for the shallow mine does not change for other stability conditions, as far as changing the number of stations outside the mine is concerned. The same trend for reduction of error statistics is not as clear for the deep mine, suggesting that the CALMET model has difficulties in predicting the wind field, even considering the inclusion of more surface station observations. The operational case C6 demonstrates the same level of accuracy compared to the high resolution case C1.

Figure 3.12 shows the calculated Bias [m s^{-1}] and RMSE [m s^{-1}] from CALMET against CFD-LS for wind speed on vertical profiles of receptors inside and downstream of the mine for different number of surface station cases for shallow and deep mine configurations under different thermal stability conditions. Overall, the error statistics are lower for the unstable condition than for the others. Further, increasing the number of stations help reduce error statistics for the stable condition. This may be attributed to complexity of the flow structure, such as the formation of standing vortices, with skimming flow under the neutral condition and waves under the stable condition (Figures 7 and 8 in the study of Kia et al. (2021) [68]), which the CALMET model does not predict.

Overall, Figures 3.11 and 3.12 show that the CALMET model can simulate wind components at 10 [m] above surface better than the entire boundary layer since the Bias [m s^{-1}] and RMSE [m s^{-1}] error statistics are lower at 10 [m] above surface. This is consistent with previous evaluations in other studies [23, 27, 139]. This may be due to the fact that the wind field is only forced by observations at 10 [m] above surface and not vertical profiles of wind, which have been shown to deviate from the logarithmic profiles in the surface layer theory (e.g. Figure 10 in Nambiar et al. (2020) [96] and Figure 5 in Nahian et al. (2020) [95]).

Figure 3.13 shows the calculated MAE [Degree] of wind direction inside and outside of the mine by CALMET against CFD-LS for the receptors at 10 [m] above surface, for the different number of surface station cases and for the shallow and deep mines under different thermal stability conditions. The outside mine areas show lower MAE than the inside mine under all stability conditions. The higher MAE inside the mine reflects the more complex flow in

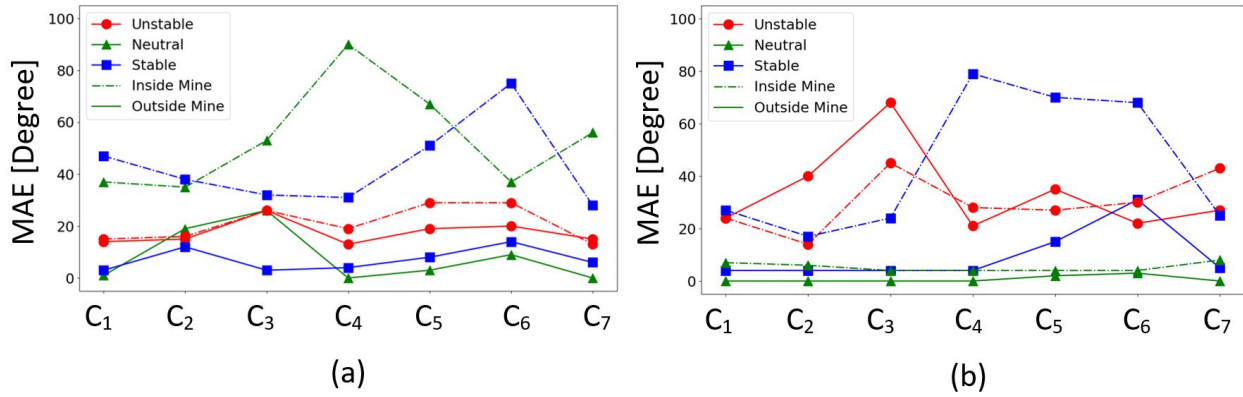


Figure 3.13: MAE [Degree] of horizontal wind direction at 10 [m] above surface inside and outside the mine predicted by CALMET against CFD-LS over different number of surface station cases and thermal stability conditions of the shallow (a) and deep (b) mine configurations.

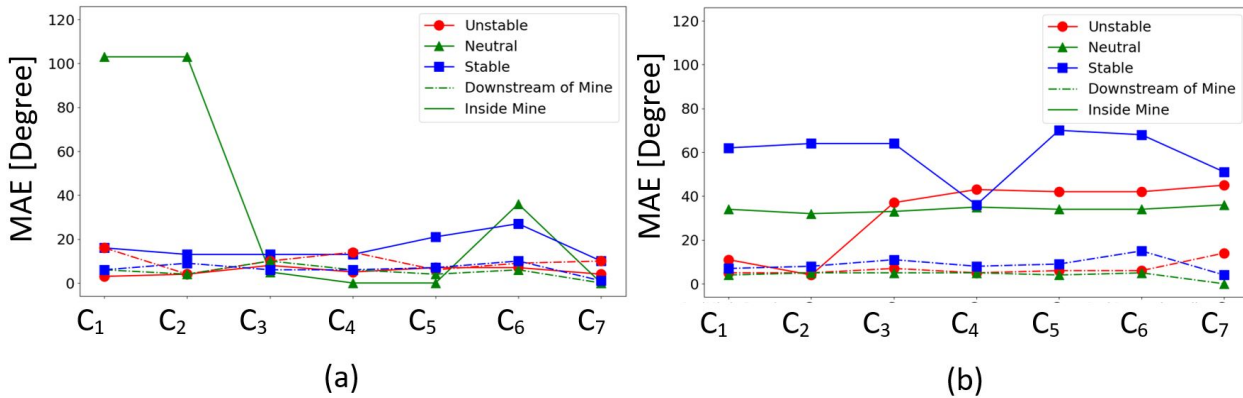


Figure 3.14: MAE [Degree] of wind direction on boundary-layer profiles inside and downstream of the mine predicted by CALMET against CFD-LS over different number of surface station cases under different thermal stability conditions of the shallow (a) and deep (b) mine configurations.

the pit compared with the surrounding flat terrain. This is in agreement with the study of Nahian et al. (2020) [95] who predicted horizontal wind circulations inside a shallow mine pit under all stability conditions (their Figure 7). On another note, wind direction prediction by CALMET provides better results under neutral and unstable conditions than the stable condition, which is in agreement with the study by Cox et al. (2005) [27] (their Figure 3). It appears that changing the number of forcing stations does not drastically change the error statistics for wind direction.

Figure 3.14 shows the calculated MAE [Degree] of wind direction on vertical profiles inside and downstream of the mine by CALMET against CFD-LS for different number of surface station cases for shallow and deep mines under different thermal stability conditions. Similar conclusions can be drawn here as was done for Figure 3.13. However, there are subtle differences. In the configuration of the shallow mine, the MAE [Degree] for wind direction is approximately 20° lower on boundary-layer profiles than near the surface. This may be due to the fact that the effect of topography on wind direction is reduced at higher altitudes. As far as the deep mine is concerned, the influence of the topography on wind direction is present at higher altitudes. For instance, under the stable condition, a standing wave was generated by the deep mine and manifested itself on a substantial portion of the boundary layer in the study of Kia et al. (2021) [68] (their Figures 7 and 8). Overall, comparing Figures 3.13 and 3.14 show better wind direction prediction on the vertical profiles than near the surface.

Overall, the presented results of concentration and wind field predictions show similar error statistics for the high resolution case C1 and the operational case C6, which demonstrate that increasing the number of surface stations in a diagnostic model does not necessarily result in increased accuracy in the wind and dispersion predictions. This outcome is in agreement with a study by Wang et al. (2008) [139]. It appears that interpolation and extrapolation of the wind field by CALMET in this topographically complex environment alone cannot reproduce the complexity predicted by prognostic models such as CFD-LS.

3.2.2.2 Effect of the Location of Met Stations

Here we consider the accuracy of the CALPUFF concentration calculations relative to the location of the forcing weather stations. Tables 3.3 and 3.4 show the Bias [$\mu\text{g m}^{-3}$], RMSE [$\mu\text{g m}^{-3}$], and $FAC2$ [%] of the CALPUFF concentration predictions at the receptors downwind of the mine (at height $z = 10$ [m]) for case C6 for the shallow and deep mines. Under the three thermal stability conditions, the error statistics do not change significantly as the surface

station locations are changed. It should be noted that the prediction of plume concentration under the stable and neutral conditions deviate further from the CFD-LS model than under the unstable conditions.

Table 3.3: Bias [$\mu\text{g m}^{-3}$] (RMSE [$\mu\text{g m}^{-3}$]) of the tracer concentration outside of the mine, predicted by CALPUFF against CFD-LS for different locations of surface stations and thermal stability conditions for case C6 of the shallow and deep mines.

Surface station locations	Bias [$\mu\text{g m}^{-3}$] (RMSE [$\mu\text{g m}^{-3}$]) of receptors' concentration outside of the mine					
	Shallow			Deep		
	Unstable	Neutral	Stable	Unstable	Neutral	Stable
$x = 1000, 8000$ [m]	-339 (2749)	-1483 (6871)	5656 (6665)	-195 (1153)	-4347 (7948)	-2557 (3210)
$x = 3000, 7000$ [m]	-361 (2745)	-1250 (6891)	6256 (7093)	-178 (1283)	-4307 (7921)	-2568 (3223)
$x = 3000, 8000$ [m]	-339 (2748)	-1463 (6871)	4863 (5806)	-193 (1152)	-4314 (7930)	-2535 (3211)
$x = 3000, 9000$ [m]	-326 (2749)	-1496 (6851)	5494 (6663)	-221 (1148)	-4347 (7954)	-2553 (3202)

Table 3.4: *FA*C2 percentage of the tracer concentration, predicted by CALPUFF against CFD-LS for different locations of surface stations and thermal stability conditions for case C6 of the shallow and deep mines.

Surface station locations	<i>FA</i> C2 [%] of receptors' concentration					
	Shallow			Deep		
	Unstable	Neutral	Stable	Unstable	Neutral	Stable
$x = 1000, 8000$ [m]	16	12	0	11	7	7
$x = 3000, 7000$ [m]	17	13	0	11	8	9
$x = 3000, 8000$ [m]	19	12	0	11	7	7
$x = 3000, 9000$ [m]	15	12	0	12	8	9

Tables 3.5 and 3.6 show the Bias [m s^{-1}] and RMSE [m s^{-1}] of wind speed prediction at different receptors at 10 [m] above surface inside and outside of the mine and on vertical profiles inside and downstream of the mine by CALMET against CFD-LS for different locations of surface stations and thermal stability conditions for case C6 of the shallow and deep mines. The error statistics change in most of the situations by less than 10% and 25% for near surface and on vertical profiles of the boundary layer, respectively. The tables show that the wind speed prediction is not substantially affected by the location of the surface stations.

Tables 3.7 and 3.8 show the MAE [degree] of horizontal wind direction at 10 [m] above surface inside and outside of the mine and on vertical profiles inside and downstream of the mine predicted by CALPUFF versus CFD-LS for different locations of surface stations and thermal stability conditions for case C6 of the shallow and deep mines. Again, the tables

Table 3.5: Bias [m s^{-1}] (RMSE [m s^{-1}]) of horizontal wind speed inside and outside of the mine at 10 [m] above surface predicted by CALMET against CFD-LS for different locations of surface stations and thermal stability conditions for case C6 of the shallow and deep mines.

Receptor locations	Surface station locations	Bias [m s^{-1}] (RMSE [m s^{-1}]) of horizontal wind speed					
		Shallow			Deep		
		Unstable	Neutral	Stable	Unstable	Neutral	Stable
Inside mine	$x = 1000, 8000$ [m]	-0.15 (0.40)	0.03 (0.44)	-2.12 (2.42)	-0.83 (1.36)	1.17 (2.50)	-0.48 (2.99)
	$x = 3000, 7000$ [m]	-0.15 (0.40)	-0.16 (0.55)	-1.83 (2.56)	-0.50 (1.37)	1.17 (2.50)	-0.68 (3.03)
	$x = 3000, 8000$ [m]	-0.16 (0.40)	0.08 (0.44)	-2.12 (2.42)	-0.83 (1.36)	1.11 (2.49)	-0.52 (3.09)
	$x = 3000, 9000$ [m]	-0.15 (0.40)	0.04 (0.43)	-2.13 (2.42)	-0.86 (1.38)	1.10 (2.50)	-0.48 (2.99)
Outside mine	$x = 1000, 8000$ [m]	-0.16 (0.35)	-1.19 (1.66)	-1.30 (1.80)	-0.09 (0.30)	0.79 (1.22)	-0.66 (1.26)
	$x = 3000, 7000$ [m]	-0.08 (0.31)	-1.14 (1.61)	-0.86 (1.32)	-0.15 (0.46)	0.28 (1.05)	-0.97 (1.46)
	$x = 3000, 8000$ [m]	-0.05 (0.32)	-1.13 (1.64)	-0.91 (1.49)	0.13 (0.86)	0.30 (1.06)	-0.63 (2.27)
	$x = 3000, 9000$ [m]	-0.05 (0.39)	-1.40 (1.90)	-1.13 (1.70)	0.01 (0.46)	0.25 (1.00)	-0.49 (1.09)

Table 3.6: Bias [m s^{-1}] (RMSE [m s^{-1}]) of wind speed on vertical boundary-layer profiles inside and downstream of the mine, predicted by CALMET versus CFD-LS for different locations of surface stations and thermal stability conditions for case C6 of the shallow and deep mines.

Receptor locations	Surface station locations	Bias [m s^{-1}] (RMSE [m s^{-1}]) of wind speed on vertical boundary-layer profiles					
		Shallow			Deep		
		Unstable	Neutral	Stable	Unstable	Neutral	Stable
Inside mine	$x = 1000, 8000$ [m]	0.26 (0.33)	-1.55 (1.89)	2.35 (3.61)	0.53 (1.14)	2.16 (3.85)	-2.27 (3.89)
	$x = 3000, 7000$ [m]	0.38 (0.47)	-1.62 (1.88)	2.37 (3.63)	0.53 (1.17)	2.14 (3.83)	-2.29 (3.91)
	$x = 3000, 8000$ [m]	0.42 (0.53)	-1.56 (1.82)	2.41 (3.70)	0.51 (1.14)	2.18 (3.88)	-2.27 (3.88)
	$x = 3000, 9000$ [m]	0.29 (0.39)	-1.48 (1.79)	2.41 (3.70)	0.47 (1.07)	2.17 (3.81)	-2.29 (3.87)
Downstream mine	$x = 1000, 8000$ [m]	-0.06 (0.40)	-5.4 (5.90)	-1.17 (1.48)	0.14 (0.30)	-2.64 (3.05)	-1.27 (1.62)
	$x = 3000, 7000$ [m]	0.25 (0.63)	-5.94 (6.36)	-1.70 (1.90)	0.19 (0.39)	-2.28 (2.91)	-1.73 (2.15)
	$x = 3000, 8000$ [m]	0.14 (0.52)	-5.45 (5.97)	-1.07 (1.37)	0.15 (0.29)	-2.88 (3.31)	-1.19 (1.53)
	$x = 3000, 9000$ [m]	-0.08 (0.37)	-5.36 (5.90)	-1.14 (1.49)	0.10 (0.26)	-2.00 (3.30)	-1.10 (1.43)

show that the wind direction prediction is not substantially affected by the location of the surface stations.

Table 3.7: MAE [Degree] of horizontal wind direction at 10 [m] above surface inside and outside of the mine predicted by CALMET against CFD-LS for different locations of surface stations and thermal stability conditions for case C6 of the shallow and deep mines.

Receptor locations	Surface station locations	MAE [Degree] of horizontal wind direction					
		Shallow			Deep		
		Unstable	Neutral	Stable	Unstable	Neutral	Stable
Inside mine	$x = 1000, 8000$ [m]	29	37	80	30	4	68
	$x = 3000, 7000$ [m]	29	38	61	30	4	69
	$x = 3000, 8000$ [m]	29	37	75	30	4	68
	$x = 3000, 9000$ [m]	29	37	79	30	4	68
Outside mine	$x = 1000, 8000$ [m]	21	14	18	23	4	28
	$x = 3000, 7000$ [m]	22	8	11	22	2	26
	$x = 3000, 8000$ [m]	20	9	14	22	3	31
	$x = 3000, 9000$ [m]	23	17	13	23	3	37

Table 3.8: MAE [Degree] of wind direction on boundary-layer profiles inside and downstream of the mine, predicted by CALMET against CFD-LS for different locations of surface stations and thermal stability conditions for case C6 of the shallow and deep mines.

Receptor locations	Surface station locations	MAE [Degree] of horizontal wind direction					
		Shallow			Deep		
		Unstable	Neutral	Stable	Unstable	Neutral	Stable
Inside mine	$x = 1000, 8000$ [m]	7	36	27	42	35	67
	$x = 3000, 7000$ [m]	7	36	25	6	35	67
	$x = 3000, 8000$ [m]	7	36	27	42	34	68
	$x = 3000, 9000$ [m]	8	36	26	42	35	68
Downstream of mine	$x = 1000, 8000$ [m]	6	6	10	6	5	16
	$x = 3000, 7000$ [m]	9	5	8	6	3	33
	$x = 3000, 8000$ [m]	9	6	10	6	5	15
	$x = 3000, 9000$ [m]	6	7	5	5	4	35

3.2.2.3 Concentration Agreement vs Downwind Receptor Location

Figure 3.15 shows how the Bias [$\mu\text{g m}^{-3}$] and RMSE [$\mu\text{g m}^{-3}$] of the CALPUFF surface concentration predictions vary with distance downwind of the mine. For this comparison the concentration receptors are grouped by their x position. CALPUFF case C6 is used for the comparison. The predictions under all stability conditions show relatively large errors for the receptors close to the mine ($x = 6500$ [m]). Beyond this distance there is a trend toward

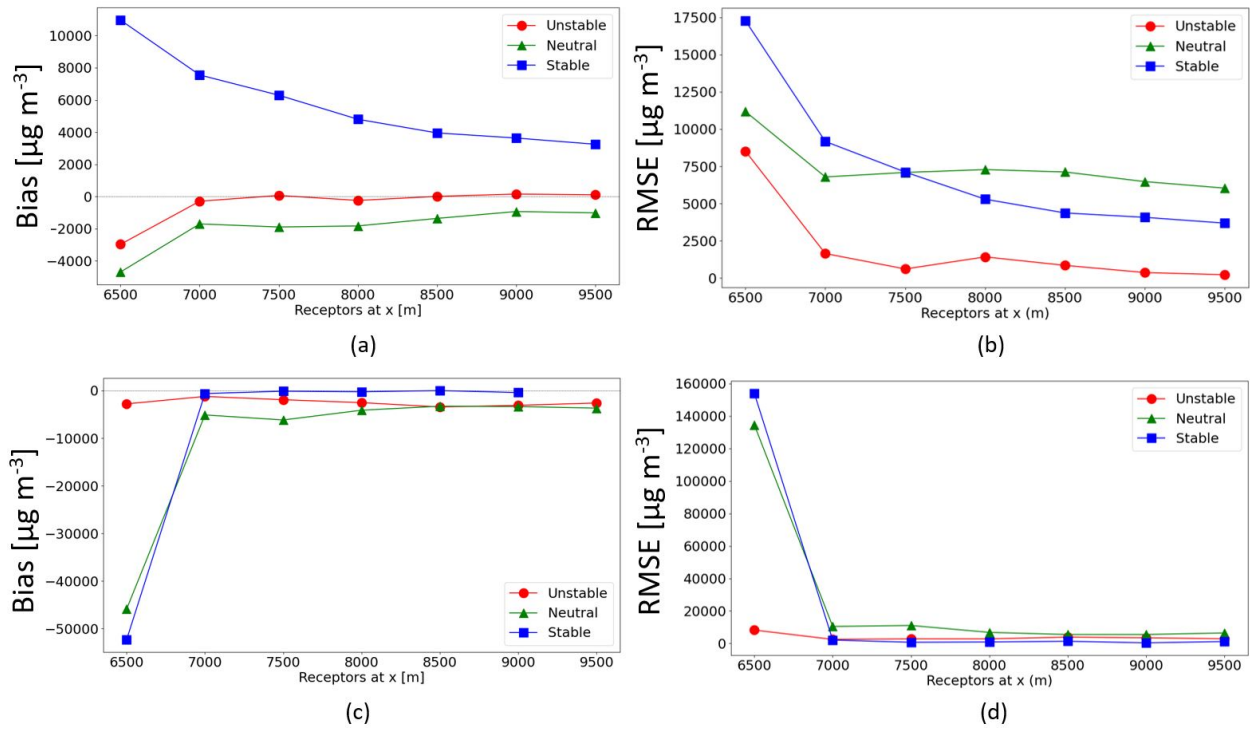


Figure 3.15: Bias [$\mu\text{g m}^{-3}$] and RMSE [$\mu\text{g m}^{-3}$] of the tracer concentration predicted by CALPUFF against CFD-LS over different receptor locations in the stream-wise direction at 10 [m] above surface under different thermal stability conditions of the shallow (a and b) and deep (c and d) mines for case C6.

reduced Bias [$\mu\text{g m}^{-3}$] and RMSE [$\mu\text{g m}^{-3}$] with increasing distance from the mine. This trend exists in all of the configurations (deep and shallow mines) and conditions (thermal stabilities). Perhaps it is no surprise that the CFD-LS and CALPUFF predictions would be most different close to the mine. The mine-pit clearly creates localized flow complexity that would have more of an impact on the plume close to the mine, and would diminish with increasing distance as the ambient ABL becomes re-established. As CALPUFF does not fully replicate the mine-induced complexity indicated by CFD-LS, this should be manifested in near-mine concentrations that are different than CFD-LS.

3.3 Implications

If the CFD model accurately represents the flow complexity in real open-pit mines, then it can be concluded that diagnostic modeling of pollutant dispersion from these mines should be performed with caution. In none of the configurations (mine depths), conditions (thermal stabilities), or cases (CALPUFF setups) studied was there good agreement between the CFD-LS and CALPUFF predictions of surface concentration downwind of the mine (i.e. they differed by more than a factor of two for the majority of downwind receptors). Over the studied short-range of downwind distances, the computed *FAC2* statistic for gas concentration was usually far less than 30%, which deemed CALPUFF's performance unacceptable according to Hanna and Chang's (2011) [52] criterion. In fact even the *FAC10* scores were generally lower than this threshold (i.e. in less than 30% of the downwind locations was CALPUFF within a factor of 10 of the CFD-LS concentrations). One reason for the discrepancy between the two models is that the diagnostically determined flow field (CALMET), which calculates a flow field by interpolating from a limited set of input wind observations, did not reproduce the complexity of the wind flow in the open-pit environments, as indicated by the CFD. It is also likely that the Gaussian modeling approach used in CALPUFF is unable to capture the fine spatial details of the mine plume, which was a pronounced feature of the CFD-LS simulations. Tomasi et al. (2019) [135] showed that CALPUFF simulation tends to generate very uniform patterns, which are not much influenced by the complex topography nor by the complexity of the flow field. They mentioned the poor performance of CALPUFF is associated with its own Gaussian formulation, which prevents the model from capturing the large degree of spatial inhomogeneity in the concentration plume over complex terrain. This capability can be improved by using the Lagrangian approach which is grid-free, and at all scales, it follows the motion of individual plume parcels [45].

Earlier we discussed the potential advantages of an IDM approach for calculating gas (or particulate) emission rates from open-pit mines. What does this work imply about that potential? The results suggest caution. While it is believed that CFD-LS could provide the basis for an accurate IDM calculation, this complex modeling system is unlikely to provide for practical IDM calculations in topographically-complex terrain. The CFD simulations took many days of computation on a computer cluster with 100 CPUs, as well as substantial expertise, to produce results for a single half-hour period. If IDM is to be broadly usable it will likely be paired with more practical diagnostic models like CALPUFF. However, in the specific mine situation (source configuration, ambient wind conditions), a downwind concentration measurement which is interpreted through a diagnostic model simulation to estimate an emission rate would give an emission rate far different from that based on CFD-LS. In the large majority of downwind locations the two models would give emission rates differing by more than a factor of 10. If one accepts that the CFD-LS model provides a more accurate representation of atmospheric transport in complex terrain than diagnostic models, then one would infer that an IDM approach based on a diagnostic model would be unreliable for open-pit mines. However, one should be cautious about overgeneralizing. Would different gas source configurations give different outcomes? For example, would an emission source that covers the total pit surface lead to a more dispersed plume that would be better represented by a diagnostic model? Would non-stationary wind conditions (e.g, mesoscale wind fluctuations) also create a more dispersed plume and increase the accuracy of a diagnostic model simulation? It also seems likely that an IDM emission calculation based on a concentration measurement taken further from the mine (further than the 3 [km] range studied here) would show greater agreement with the more sophisticated CFD-LS model. A more appropriate conclusion based on this work is that IDM combined with diagnostic dispersion models should be approached with caution in complex terrain.

Chapter 4

Conclusions, Limitations, and Recommendations

Atmospheric modeling methods help better investigate gas and particulate transport from complex terrains such as open-pit mines. Prognostic and diagnostic models are common tools to perform Atmospheric Boundary Layer (ABL) transport simulations with model-specific advantages and disadvantages. The main and original contributions of this work were 1) to investigate the atmospheric transport phenomena over a synthetic open-pit mine, for various mine depths and thermal-stability conditions, using a prognostic and novel Computational Fluid Dynamics-Lagrangian Stochastic (CFD-LS) model based on the Very Large-Eddy Simulation (VLES) paradigm; 2) to compare such results with predictions of the diagnostic CALifornia PUFF (CALPUFF) model; and 3) to consider the prospects of Inverse Dispersion Modeling (IDM) calculations of emission estimates from such complex topographies given the findings. Such investigations filled an important gap in the scientific literature, which often overlooks the roles of complex topography and thermal-stability conditions when modeling atmospheric transport phenomena over open-pit mines using either prognostic or diagnostic tools.

4.1 Conclusions

In the first part of this study atmospheric flow and transport were simulated using CFD inside and surrounding two synthetic open-pit mines of different depths under different thermal stability conditions. A VLES method was used, which was capable of resolving the turbulent fluctuations in the interior of the domain while modelling transport phenomena near walls

using wall functions. The main objective was to investigate the effects of mine depth and thermal stability on the flow structure and dispersion of a fugitive passive scalar released from the surface of the mines. Six simulations were conducted for two mine depths: a shallow (~ 100 [m]) and a deep (~ 500 [m]) mine; and three thermal stability conditions aimed at matching the friction velocity u_* [m s^{-1}] and Obukhov length L [m] from an observation dataset: thermally-unstable ($u_* = 0.25$ [m s^{-1}], $L = -11$ [m]), thermally-neutral ($u_* = 0.46$ [m s^{-1}]), and thermally-stable ($u_* = 0.12$ [m s^{-1}], $L = 9$ [m]) conditions. The CFD model was evaluated against field observations within the surface layer upstream of the mines to gain confidence in its predictions.

For the shallow mine, the following predictions were made. Under thermally-unstable conditions substantial mixing and rising of the passive scalar plume occurred downstream of the mine so that the plume was diluted and had a depth that reached a large portion of the ABL. Under the thermally-neutral condition, skimming flow was predicted, and the plume rise was limited to the surface layer downstream of the mine. Substantial circulation of flow inside the mine was predicted under both thermally-unstable and neutral conditions. Under the thermally-stable condition, less flow circulation was predicted inside the mine, and the plume rise was limited to the surface layer downstream of the mine.

For the deep mine under thermally-unstable conditions, substantial mixing and rising of the passive scalar plume occurred downstream of the mine, so that the plume was diluted and covered within a greater portion of the ABL than the other thermal stability cases. Also, under thermally-neutral conditions, the skimming flow was predicted, restricting the plume to the surface layer downstream of the mine. In the stable case, a standing wave formed, which brought warm air from aloft upstream of the mine into the bottom of the mine, and a rising flow structure transported the passive scalar upward from the center of the mine into the ABL above the surface layer.

In the second part of this study atmospheric transport phenomena were simulated using CALPUFF and CFD-LS models inside and surrounding the same two synthetic open-pit mines of different depths under different thermal stability conditions. The main aim of the study was to investigate how well the two models compare when predicting wind and concentration fields associated with the dispersion of area-fugitive sources of gas emissions from the mine.

The VLES method was used to supply the flow fields for both the CALPUFF and CFD-LS models. The VLES results were used directly as a comparison dataset for the wind field predicted by the CALPUFF (CALMET) model. The LS model generated the

gas concentration field as a comparison dataset for gas concentration field predicted by the CALPUFF model.

Six simulations were conducted for two mine depths: a shallow (~ 100 m) and a deep (~ 500 m) mine; and three thermal stability conditions. For the shallow and deep mines, the following conclusions were made. In most of the configurations (mine depth) and conditions (thermal stabilities) studied, the concentration estimates were insensitive to the number of meteorological stations, suggesting there is no benefit to adding multiple stations in a CALPUFF modeling effort. One surface station inside the mine and four surface stations outside the mine can be sufficient. Changing the location of the surface meteorological stations does not influence the prediction of flow and concentration field substantially. The results suggest that the accuracy of the CALPUFF concentration predictions do depend on location. While there is no location in the modelling domain where the CALPUFF predictions were in good agreement with CFD-LS, there were locations where the two models strongly disagreed, and locations where the disagreement was less. In general, concentration at the downwind edge of the mine was poorly predicted in CALPUFF. This is not surprising, as wind complexity within the mine is not well represented by the CALMET diagnostic model.

Overall the CALPUFF surface concentration predictions downwind of the mines are in poor agreement with the CFD-LS predictions. The reasons for this are mainly attributed to the complex structure of the flow under such conditions, such as horizontal and vertical wind circulations in the mine, formation of standing waves, and plume rise, which the CALPUFF model cannot predict. It is suggested that the disagreements between the two models are mainly caused by diagnostic modeling of the wind field, versus prognostic modeling, although inaccuracies in the Gaussian puff model may also be possible, which were not investigated in this study.

Diagnostic modeling of wind field and gas dispersion finds many applications in air quality studies and quantification of area-fugitive emission fluxes. There are many examples of successful IDM emission measurements based on these types of models, but the majority have taken place in reasonably simple terrain. The evidence provided in this thesis shall caution practitioners when using diagnostic tools for investigation of atmospheric transport phenomena related to open-pit mines with complex topography. While the CFD-LS model results are not certain, the findings here can provide guidelines on applicability or appropriate setup for CALPUFF for complex terrains.

4.2 Limitations

Despite the advantages, the VLES method has some limitations for real investigations that require further research. This model cannot simulate very low wind speed conditions, which is a characteristic of some thermally-stable boundary layers at nighttime. This application would require further research and development for the model. The inlet boundary conditions for the model need to be carefully adapted for each atmospheric state. The model cannot incorporate horizontal variations of meteorological fields at the mesoscale (wind direction change, meandering, etc.) so there are limitations on the scale at which the model can be used successfully. To be used at larger scales, the model may be coupled or nested with the Weather Research and Forecasting (WRF) model for the appropriate specification of inlet and boundary conditions.

Meso-scale models such as WRF are operationally simulated with low horizontal resolutions at 2-4 [km], which in the present work is the same order as the horizontal dimensions of the mine. This is probably not high enough to resolve the impact of the mine terrain. Such models would be unlikely to represent important features of the wind field associated with the mine, such as vertical and horizontal circulations inside the mine pit. High resolution meso-scale simulations with horizontal grid spacings down to 50-200 [m] can be performed using the LES method to capture these complex features; however, this kind of high-resolution modeling is still beyond reach for operational purposes. It is yet to be seen how and if high-resolution meso-scale models will be successfully utilized to supply reliable wind field data to the CALPUFF model toward more successful simulations at the scale of typical open-pit mines.

4.3 Recommendations

Various future recommendations can be provided to improve this work. One of the main drivers of pollutant transport is the wind field, but wind patterns for open-pit mines are not studied in great detail observationally. As the meso-scale models can provide wind field at each grid location of the domain in horizontal and vertical directions, it is suggested to use high-resolution meso-scale models to be coupled with CALMET. It can possibly improve the flow field prediction, which may result in better plume dispersion predictions and increased CALPUFF efficiency. Most commonly, wind patterns at open-pit mines are observed by deploying few surface stations or at most one SO_Nic Detection And Ranging (SODAR)

sensor, which is only capable of resolving the vertical profiles of wind. These sensors cannot resolve the full three-dimensionality of the flow at high spatio-temporal resolution. More recently, advanced LIght Detection And Ranging (LIDAR) sensors for wind assessment have been developed that are capable of observing slope flows, waves, and wind circulations, both horizontally and vertically. Such datasets can provide ground truth for high resolution wind field models based on prognostic and diagnostic paradigms.

The investigation of CALPUFF in this work is not exhaustive. For instance, the investigation of the parameterization of the Gaussian puff model was left out of this study. Also many investigations of parameterizations in the wind field model in CALPUFF, considering cloud cover, and radiation can be attempted. In addition, the effect of the horizontal and vertical spatial resolution for forcing the wind field in CALPUFF can be pursued further. Such in depth investigations can be attempted in the future.

All considered, the availability of computational power to predict the wind field and dispersion phenomena using prognostic modeling, such as CFD, high-resolution meso-scale models, or other models, offer a new paradigm for improving wind field and dispersion modeling associated with complex terrains, such as those encountered in open-pit mining areas.

References

- [1] AHMADI-BALOUTAKI, M., AND ALIABADI, A. A. A Very Large-Eddy Simulation Model Using a Reductionist Inlet Turbulence Generator and Wall Modelling for Stable Atmospheric Boundary Layers. *Fluid Dynamics* 56, 3 (2021), 413–432.
- [2] ALIABADI, A. A. *Theory and applications of turbulence: A fundamental approach for scientists and engineers*. Amir A. Aliabadi Publications, Guelph, Ontario, Canada, 2018.
- [3] ALIABADI, A. A., KRAYENHOFF, E. S., NAZARIAN, N., CHEW, L. W., ARMSTRONG, P. R., AFSHARI, A., AND NORFORD, L. K. Effects of roof-edge roughness on air temperature and pollutant concentration in urban canyons. *Bound.-Lay. Meteorol.* 164, 2 (2017), 249–279.
- [4] ALIABADI, A. A., MORADI, M., AND BYERLAY, R. A. E. The budgets of turbulence kinetic energy and heat in the urban roughness sublayer. *Environ. Fluid Mech.* 21, 4 (2021), 843–884.
- [5] ALIABADI, A. A., MORADI, M., CLEMENT, D., LUBITZ, W. D., AND GHARABAGHI, B. Flow and temperature dynamics in an urban canyon under a comprehensive set of wind directions, wind speeds, and thermal stability conditions. *Environ. Fluid Mech.* 19, 1 (2019), 81–109.
- [6] ALIABADI, A. A., MORADI, M., MCLEOD, R. M., CALDER, D., AND DERNOVSEK, R. How Much Building Renewable Energy Is Enough? The Vertical City Weather Generator (VCWG v1.4.4). *Atmosphere* 12, 7 (2021), 882.
- [7] ALIABADI, A. A., VERIOTES, N., AND PEDRO, G. A Very Large-Eddy Simulation (VLES) model for the investigation of the neutral atmospheric boundary layer. *J. Wind Eng. Ind. Aerodyn.* 183 (2018), 152–171.
- [8] ARREGOCÉS, H., ROJANO, R., RESTREPO, G., AND ANGULO, L. Using CALPUFF to determine the environmental impact of a coal mine open pit. *WIT Trans. Ecol. Environ.* 207 (2016), 55–66.
- [9] BADACH, J., KOLASIŃSKA, P., PACIOREK, M., WOJNOWSKI, W., DYMERSKI, T., GEBICKI, J., DYMNIĆKA, M., AND NAMIEŚNIK, J. A case study of odour nuisance

- evaluation in the context of integrated urban planning. *J. Environ. Manag.* 213 (2018), 417–424.
- [10] BAI, M., SUTER, H., LAM, S. K., FLESCH, T. K., AND CHEN, D. Comparison of slant open-path flux gradient and static closed chamber techniques to measure soil N₂O emissions. *Atmos. Meas. Tech.* 12, 2 (2019), 10951102.
- [11] BAKLANOV, A. A. Numerical modelling of atmosphere processes in mountain cirques and open pits. *WIT Trans. Ecol. Envir.* 9 (1995), 8.
- [12] BAKLANOV, A. A. Application of CFD methods for modelling in air pollution problems: Possibilities and gaps. *Environ. Monit. Assess.* 65, 1-2 (2000), 181–189.
- [13] BARAY, S., DARLINGTON, A., GORDON, M., HAYDEN, K. L., LEITHEAD, A., LI, S. M., LIU, P. S. K., MITTERMEIER, R. L., MOUSSA, S. G., O'BRIEN, J., STAEBLER, R., WOLDE, M., WORTHY, D., AND MCLAREN, R. Quantification of methane sources in the Athabasca Oil Sands Region of Alberta by aircraft mass balance. *Atmos. Chem. Phys.* 18, 10 (2018), 7361–7378.
- [14] BENHAMADOUCHE, S., JARRIN, N., ADDAD, Y., AND LAURENCE, D. Synthetic turbulent inflow conditions based on a vortex method for large-eddy simulation. *Prog. Comput. Fluid Dy.* 6, 1-3 (2006), 50–57.
- [15] BHOWMICK, T. Three dimensional computational fluid dynamics models of fugitive dust dispersion in high-latitude open-pit mines. Master's thesis, University of Alaska Fairbanks, USA, 2015.
- [16] BHOWMICK, T., BANDOPADHYAY, S., AND GHOSH, T. Three-dimensional CFD modeling approach to approximate air pollution conditions in high-latitude open-pit mines. *WIT Trans. Built. Env.* 168 (2015), 741–753.
- [17] BLOCKEN, B., STATHOPOULOS, T., AND CARMELIET, J. CFD simulation of the atmospheric boundary layer: Wall function problems. *Atmos. Environ.* 41, 2 (2007), 238–252.
- [18] BREEDT, H. J., CRAIG, K. J., AND JOTHIPRAKASAM, V. D. Monin-Obukhov similarity theory and its application to wind flow modelling over complex terrain. *J. Wind Eng. Ind. Aerod.* 182 (2018), 308–321.
- [19] BRÉS, G. A., AND COLONIUS, T. Three dimensional instabilities in compressible flow over open cavities. *J. Fluid Mech.* 599 (2008), 309–339.
- [20] BRUTSAERT, W. Land-surface water vapor and sensible heat flux: Spatial variability, homogeneity, and measurement scales. *Water Resour. Res.* 34, 10 (1998), 2433–2442.

- [21] BYERLAY, R. A. E., NAMBIAR, M. K., NAZEM, A., NAHIAN, M. R., BIGLAR-BEGIAN, M., AND ALIABADI, A. A. Measurement of land surface temperature from oblique angle airborne thermal camera observations. *Int. J. Remote Sens.* 41, 8 (2020), 3119–3146.
- [22] CASSIANI, M., STOHL, A., AND BRIOUDE, J. Lagrangian stochastic modelling of dispersion in the convective boundary layer with skewed turbulence conditions and a vertical density gradient: Formulation and implementation in the FLEXPART model. *Bound.-Lay Meteorol.* 154, 3 (2015), 367–390.
- [23] CHANG, J. C., FRANZESE, P., CHAYANTRAKOM, K., AND HANNA, S. R. Evaluations of CALPUFF, HPAC, and VLSTRACK with two mesoscale field datasets. *J. Appl. Meteorol.* 42, 4 (2003), 453–466.
- [24] CHENG, W., AND LIU, C.-H. Large-eddy simulation of turbulent transports in urban street canyons in different thermal stabilities. *J. Wind. Eng. Ind. Aerod.* 99, 4 (2011), 434–442.
- [25] CHOUDHURY, A., AND BANDOPADHYAY, S. The effect of overall pit slope and pit geometry on the dispersion of pollutants in a hypothetical Arctic open-pit mine. *Natural Resources & Engineering* 1, 1 (2016), 26–34.
- [26] CLEMENTS, C. B., WHITEMAN, C. D., AND HOREL, J. D. Cold-air-pool structure and evolution in a mountain basin: Peter Sinks, Utah. *J. Appl. Meteorol.* 42, 6 (2003), 752–768.
- [27] COX, R. M., SONTOWSKI, J., AND DOUGHERTY, C. M. An evaluation of three diagnostic wind models (CALMET, MCSCIPUF, and SWIFT) with wind data from the Dipole Pride 26 field experiments. *Meteorol. Appl.* 12, 4 (2005), 329–341.
- [28] CUI, H., YAO, R., CHEN, L., LV, M., XIN, C., AND WU, Q. Field study of atmospheric boundary layer observation in a hilly Gobi Desert region and comparison with the CALMET/CALPUFF model. *Atmos. Environ.* 235 (2020), 117576.
- [29] DYER, A. J. A review of flux-profile relationships. *Bound.-Lay. Meteorol.* 7, 3 (1974), 363–372.
- [30] FATTAL, E., DAVID-SAROUSI, H., KLAUSNER, Z., AND BUCHMAN, O. An urban Lagrangian stochastic dispersion model for simulating traffic particulate-matter concentration fields. *Atmosphere* 12, 5 (2021), 580.
- [31] FERNÁNDEZ-GONZÁLEZ, S., MARTÍN, M. L., GARCÍA-ORTEGA, E., MERINO, A., LORENZANA, J., SÁNCHEZ, J. L., VALERO, F., AND RODRIGO, J. S. Sensitivity analysis of the WRF model: Wind-resource assessment for complex terrain. *J. Appl. Meteorol. Clim.* 57, 3 (2018), 733–753.

- [32] FERRERO, E., AND MACCARINI, F. Concentration fluctuations of single particle stochastic Lagrangian model assessment with experimental field data. *Atmosphere* 12, 5 (2021), 589.
- [33] FLESCH, T. K., MCGINN, S. M., CHEN, D., WILSON, J. D., AND DESJARDINS, R. L. Data filtering for inverse dispersion emission calculations. *Agr. Forest Meteorol.* 198 (2014), 1–6.
- [34] FLESCH, T. K., PRUEGER, J. H., AND HATFIELD, J. L. Turbulent Schmidt number from a tracer experiment. *Agr. Forest Meteorol.* 111, 4 (2002), 299–307.
- [35] FLESCH, T. K., WILSON, J. D., HARPER, L. A., AND CRENNNA, B. P. Estimating gas emissions from a farm with an inverse-dispersion technique. *Atmos. Environ.* 39, 27 (2005), 4863–4874.
- [36] FLESCH, T. K., WILSON, J. D., HARPER, L. A., CRENNNA, B. P., AND SHARPE, R. R. Deducing ground-to-air emissions from observed trace gas concentrations: A field trial. *J. Appl. Meteorol.* 43, 3 (2004), 487–502.
- [37] FLESCH, T. K., WILSON, J. D., AND YEE, E. Backward-Time Lagrangian Stochastic Dispersion Models and Their Application to Estimate Gaseous Emissions. *J. Appl. Meteorol.* 34, 6 (1995), 1320–1332.
- [38] FLORES, F., GARREAUD, R., AND MUÑOZ, R. C. CFD simulations of turbulent buoyant atmospheric flows over complex geometry: Solver development in OpenFOAM. *Comput. Fluids* 82 (2013), 1–13.
- [39] FLORES, F., GARREAUD, R., AND MUÑOZ, R. C. OpenFOAM applied to the CFD simulation of turbulent buoyant atmospheric flows and pollutant dispersion inside large open pit mines under intense insolation. *Comput. Fluids* 90 (2014), 72–87.
- [40] FOKEN, T., AUBINET, M., AND LEUNING, R. The eddy covariance method. In *Eddy covariance*, M. Aubinet, T. Vesala, and D. Papale, Eds. Springer, Dordrecht, 2012, pp. 1–19.
- [41] GAO, Z., DESJARDINS, R. L., AND FLESCH, T. K. Comparison of a simplified micrometeorological mass difference technique and an inverse dispersion technique for estimating methane emissions from small area sources. *Agr. Forest Meteorol.* 149, 5 (2009), 891–898.
- [42] GAVRILOV, K. A., MORVAN, D., ACCARY, G., LYUBIMOV, D. V., MERADJI, S., AND BESSONOV, O. A. Numerical modeling of coherent structures attendant on impurity propagation in the atmospheric boundary layer over a forest canopy. *Fluid Dyn.* 46, 1 (2011), 138–147.

- [43] GHOREISHI-MADISEH, S. A., SASMITO, A. P., HASSANI, F. P., AND AMIRI, L. Performance evaluation of large scale rock pit seasonal thermal energy storage for application in underground mine ventilation. *Appl. Energ.* 185 (2017), 1940–1947.
- [44] GIAIOTTI, D., OSHUROK, D., AND SKRYNYK, O. The Chernobyl nuclear accident ^{137}Cs cumulative depositions simulated by means of the CALMET/CALPUFF modelling system. *Atmos. Pollut. Res.* 9, 3 (2018), 502–512.
- [45] GIOVANNINI, L., FERRERO, E., KARL, T., ROTACH, M. W., STAQUET, C., TRINI CASTELLI, S., AND ZARDI, D. Atmospheric pollutant dispersion over complex terrain: Challenges and needs for improving air quality measurements and modeling. *Atmosphere* 11, 6 (2020), 646.
- [46] GORDON, M., LI, S.-M., STAEBLER, R., DARLINGTON, A., HAYDEN, K., O'BRIEN, J., AND WOLDE, M. Determining air pollutant emission rates based on mass balance using airborne measurement data over the Alberta oil sands operations. *Atmos. Meas. Tech.* 8, 9 (2015), 3745–3765.
- [47] GREENSHIELDS, C. J. OpenFOAM: The open source CFD toolbox, user guide, version 4.0. Tech. rep., OpenFOAM Foundation Ltd., London, 2016.
- [48] GUALTIERI, C., ANGELOUDIS, A., BOMBARDELLI, F., JHA, S., AND STOESSER, T. On the values for the turbulent Schmidt number in environmental flows. *Fluids* 2, 2 (2017), 17.
- [49] HAN, B. S., BAIK, J.-J., PARK, S.-B., AND KWAK, K.-H. Large-eddy simulations of reactive pollutant dispersion in the convective boundary layer over flat and urban-like surfaces. *Bound.-Lay. Meteorol.* 172, 2 (2019), 271–289.
- [50] HAN, X., LIU, D., XU, C., AND SHEN, W. Z. Similarity functions and a new $k - \varepsilon$ closure for predicting stratified atmospheric surface layer flows in complex terrain. *Renew. Energ.* 150 (2020), 907–917.
- [51] HAN, Y., STOELLINGER, M., AND NAUGHTON, J. Large-eddy simulation for atmospheric boundary layer flow over flat and complex terrains. *J. Phys. Conf. Ser.* 753 (2016), 032044.
- [52] HANNA, S. R., AND CHANG, J. Setting Acceptance Criteria for Air Quality Models. In *Air Pollution Modeling and its Application XXI*, D. G. Steyn and S. Trini Castelli, Eds. Springer, Dordrecht, 2011.
- [53] HANNA, S. R., CHANG, J., AND STRIMAITIS, D. Hazardous gas model evaluation with field observations. *Atmos. Environ.* 27, 15 (1993), 2265–2285.
- [54] HANSEN, K. S., BARTHELMIE, R. J., JENSEN, L. E., AND SOMMER, A. The impact of turbulence intensity and atmospheric stability on power deficits due to wind turbine wakes at Horns Rev wind farm. *Wind Energy* 15, 1 (2012), 183–196.

- [55] HOLNICKI, P., KALUSZKO, A., NAHORSKI, Z., STANKIEWICZ, K., AND TRAPP, W. Air quality modeling for Warsaw agglomeration. *Arch. Environ. Prot.* 43, 1 (2017), 48–64.
- [56] HORST, T. The footprint for estimation of atmosphere-surface exchange fluxes by profile techniques. *Bound.-Lay. Meteorol.* 90, 2 (1999), 171–188.
- [57] HU, X.-M., XUE, M., KLEIN, P. M., ILLSTON, B. G., AND CHEN, S. Analysis of urban effects in Oklahoma city using a dense surface observing network. *J. Appl. Meteorol. Clim.* 55, 3 (2016), 723–741.
- [58] HUANG, J., AND BOU-ZEID, E. Turbulence and vertical fluxes in the stable atmospheric boundary layer. Part I: A large-eddy simulation study. *J. Atmos. Sci.* 70 (2013), 1513–1527.
- [59] JAYATILLAKA, C. L. V. The influence of Prandtl number and surface roughness on the resistance of the laminar sublayer to momentum and heat transfer. *Prog. Heat Mass Transfer* 1 (1969), 193–329.
- [60] JITTRA, N., PINTHONG, N., AND THEPANONDH, S. Performance evaluation of AERMOD and CALPUFF air dispersion models in industrial complex area. *Air, Soil Water Res.* 8 (2015), ASWR–S32781.
- [61] JOSEPH, G. M. D., LOWNDES, I. S., AND HARGREAVES, D. A computational study of particulate emissions from Old Moor Quarry, UK. *J. of Wind Eng. Ind. Aerod.* 172 (2018), 68–84.
- [62] KAIMAL, J. C., WYNGAARD, J. C., HAUGEN, D. A., COTÉ, O. R., IZUMI, Y., CAUGHEY, S. J., AND READINGS, C. J. Turbulence structure in the convective boundary layer. *J. Atmos. Sci.* 33, 11 (1976), 2152–2169.
- [63] KANG, W., AND SUNG, H. J. Large-scale structures of turbulent flows over an open cavity. *J. Fluid. Struct.* 25, 8 (2009), 1318–1333.
- [64] KATO, M., AND HANAFUSA, T. Wind tunnel simulation of atmospheric turbulent flow over a flat terrain. *Atmos. Environ.* 30, 16 (1996), 2853–2858.
- [65] KATTA, A. K., DAVIS, M., AND KUMAR, A. Development of disaggregated energy use and greenhouse gas emission footprints in Canada’s iron, gold, and potash mining sectors. *Resour. Conserv. Recy.* 152 (2020), 104485.
- [66] KAYS, W. M. Turbulent Prandtl number. Where are we? *J. Heat Trans.-T. ASME* 116, 2 (1994), 284–295.
- [67] KAYS, W. M., AND CRAWFORD, M. E. *Convective heat and mass transfer*, 3rd ed. McGraw-Hill Inc., New York, 1993.

- [68] KIA, S., FLESCH, T. K., FREEMAN, B. S., AND ALIABADI, A. A. Atmospheric transport over open-pit mines: The effects of thermal stability and mine depth. *J. Wind Eng. Ind. Aerod.* 214 (2021), 104677.
- [69] KIM, H. G., PATEL, V., AND LEE, C. M. Numerical simulation of wind flow over hilly terrain. *J. Wind. Eng. Ind. Aerod.* 87 (2000), 45–60.
- [70] KOELTZSCH, K. The height dependence of the turbulent Schmidt number within the boundary layer. *Atmos. Environ.* 34, 7 (2000), 1147–1151.
- [71] KUMAR, V., KLEISSL, J., MENEVEAU, C., AND PARLANGE, M. B. Large-eddy simulation of a diurnal cycle of the atmospheric boundary layer: Atmospheric stability and scaling issues. *Water Resour. Res.* 42 (2006), W06D09.
- [72] LABOIS, M., AND LAKEHAL, D. Very-Large Eddy Simulation (V-LES) of the flow across a tube bundle. *Nucl. Eng. Des.* 241, 6 (2011), 2075–2085.
- [73] LEHNER, M., WHITEMAN, C. D., HOCH, S. W., CROSMAN, E. T., JEGLUM, M. E., CHERUKURU, N. W., CALHOUN, R., ADLER, B., KALTHOFF, N., ROTUNNO, R., HORST, T. W., SEMMER, S., BROWN, W. O. J., ONCLEY, S. P., VOGT, R., GRUDZIELANEK, A. M., CERMAK, J., FONTEYNE, N. J., BERNHOFER, C., PITACCO, A., AND KLEIN, P. The METCRAX II field experiment: A study of downslope windstorm-type flows in Arizona’s Meteor Crater. *B. Am. Meteorol. Soc.* 97, 2 (2016), 217–235.
- [74] LI, D. Turbulent Prandtl number in the atmospheric boundary layer—where are we now? *Atmos. Res.* 216 (2019), 86–105.
- [75] LI, D., KATUL, G. G., AND ZILITINKEVICH, S. S. Revisiting the turbulent Prandtl number in an idealized atmospheric surface layer. *J. Atmos. Sci.* 72, 6 (2015), 2394–2410.
- [76] LI, S. W., HU, Z. Z., CHAN, P. W., AND HU, G. A study on the profile of the turbulence length scale in the near-neutral atmospheric boundary for sea (homogeneous) and hilly land (inhomogeneous) fetches. *J. Wind. Eng. Ind. Aerod.* 168 (2017), 200–210.
- [77] LI, X.-X., BRITTER, R. E., KOH, T. Y., NORFORD, L. K., LIU, C.-H., ENTEKHABI, D., AND LEUNG, D. Y. C. Large-eddy simulation of flow and pollutant transport in urban street canyons with ground heating. *Bound.-Lay. Meteorol.* 137, 2 (2010), 187–204.
- [78] LI, Y., AND GUO, H. Comparison of odor dispersion predictions between CFD and CALPUFF models. *T. ASABE* 49, 6 (2006), 1915–1926.

- [79] LIAO, W., WANG, S., LIU, C., GAO, Z., AND FLESCHE, T. K. Measuring Ammonia emissions from vegetable greenhouses with an inverse dispersion technique. *Agr. Forest Meteorol.* 278 (2019), 107653.
- [80] LIGGIO, J., LI, S.-M., STAEBLER, R. M., HAYDEN, K., DARLINGTON, A., MITTERMEIER, R. L., O'BRIEN, J., MCLAREN, R., WOLDE, M., WORTHY, D., AND VOGEL, F. Measured Canadian oil sands CO₂ emissions are higher than estimates made using internationally recommended methods. *Nat. Commun.* 10, 1 (2019), 1863.
- [81] LIN, C., OOKA, R., KIKUMOTO, H., SATO, T., AND ARAI, M. CFD simulations on high-buoyancy gas dispersion in the wake of an isolated cubic building using steady RANS model and LES. *Build. Environ.* 188 (2021), 107478.
- [82] LUHAR, A. K., AND RAO, K. S. Lagrangian stochastic dispersion model simulations of tracer data in nocturnal flows over complex terrain. *Atmos. Environ.* 28, 21 (1994), 34173431.
- [83] MAHRT, L., AND VICKERS, D. Boundary-layer adjustment over small-scale changes of surface heat flux. *Bound.-Lay. Meteorol.* 116, 2 (2005), 313–330.
- [84] MAHRT, L., AND VICKERS, D. Extremely weak mixing in stable conditions. *Bound.-Lay. Meteorol.* 119, 1 (2006), 19–39.
- [85] MATHEY, F., COKLJAT, D., BERTOGLIO, J. P., AND SERGENT, E. Assessment of the vortex method for large-eddy simulation inlet conditions. *Prog. Comput. Fluid Dy.* 6, 1-3 (2006), 58–67.
- [86] MAURER, V., KALTHOFF, N., WIESER, A., KOHLER, M., MAUDER, M., AND GANTNER, L. Observed spatiotemporal variability of boundary-layer turbulence over flat, heterogeneous terrain. *Atmos. Chem. Phys.* 16, 3 (2016), 1377–1400.
- [87] MEDEIROS, L. E., AND FITZJARRALD, D. R. Stable boundary layer in complex terrain. Part I: Linking fluxes and intermittency to an average stability index. *J. Appl. Meteorol. Clim.* 53, 9 (2014), 2196–2215.
- [88] MEDEIROS, L. E., AND FITZJARRALD, D. R. Stable boundary layer in complex terrain. Part II: Geometrical and sheltering effects on mixing. *J. Appl. Meteorol. Clim.* 54, 1 (2015), 170–188.
- [89] MELLOR, G. L., AND YAMADA, T. A hierarchy of turbulence closure models for planetary boundary layers. *J. Atmos. Sci.* 31 (1974), 1791–1806.
- [90] MEYERS, T. P., HALL, M. E., LINDBERG, S. E., AND KIM, K. Use of the modified Bowen-ratio technique to measure fluxes of trace gases. *Atmos. Environ.* 30, 19 (1996), 3321–3329.

- [91] MONIN, A. S., AND OBUKHOV, A. M. Basic laws of turbulent mixing in the surface layer of the atmosphere. *Contrib. Geophys. Inst. Acad. Sci. USSR* 151, 24 (1954), 163–187.
- [92] MORADI, M., DYER, B., NAZEM, A., NAMBIAR, M. K., NAHIAN, M. R., BUENO, B., MACKEY, C., VASANTHAKUMAR, S., NAZARIAN, N., KRAYENHOFF, E. S., NORFORD, L. K., AND ALIABADI, A. A. The vertical city weather generator (VCWG v1.3.2). *Geosci. Model Dev.* 14, 2 (2021), 961–984.
- [93] MORADI, M., KRAYENHOFF, E. S., AND ALIABADI, A. A. A comprehensive indoor–outdoor urban climate model with hydrology: The Vertical City Weather Generator (VCWG v2.0.0). *Building and Environment* 207 (2022), 108406.
- [94] MÜLLER, P. *The equations of oceanic motions*. Cambridge University Press, Cambridge, 2006.
- [95] NAHIAN, M. R., NAZEM, A., NAMBIAR, M. K., BYERLAY, R., MAHMUD, S., SEGUIN, A. M., ROBE, F. R., RAVENHILL, J., AND ALIABADI, A. A. Complex meteorology over a complex mining facility: Assessment of topography, land use, and grid spacing modifications in WRF. *J. Appl. Meteorol. Clim.* 59, 4 (2020), 769–789.
- [96] NAMBIAR, M. K., BYERLAY, R. A. E., NAZEM, A., NAHIAN, M. R., MORADI, M., AND ALIABADI, A. A. A Tethered Air Blimp (TAB) for observing the microclimate over a complex terrain. *Geosci. Instrum. Meth.* 9, 1 (2020), 193–211.
- [97] NAMBIAR, M. K., ROBE, F. R., SEGUIN, A. M., ENDSIN, M., AND ALIABADI, A. A. Diurnal and seasonal variation of area-fugitive methane advective flux from an open-pit mining facility in Northern Canada using WRF. *Atmosphere* 11, 11 (2020), 1227.
- [98] NIEUWSTADT, F. T. M. The turbulent structure of the stable, nocturnal boundary layer. *J. Atmos. Sci.* 41, 14 (1984), 2202–2216.
- [99] NOZAWA, K., AND TAMURA, T. Large-eddy simulation of the flow around a low-rise building immersed in a rough-wall turbulent boundary layer. *J. Wind Eng. Ind. Aerodyn.* 90, 10 (2002), 1151–1162.
- [100] OLENIACZ, R., AND RZESZUTEK, M. Intercomparison of the CALMET/CALPUFF modeling system for selected horizontal grid resolutions at a local scale: A case study of the MSWI Plant in Krakow, Poland. *Pol. J. Appl. Sci.* 8, 11 (2018), 2301.
- [101] PANOFSKY, H. A., AND DUTTON, J. A. *Atmospheric turbulence: Models and methods for engineering applications*. John Wiley&Sons, New York, 1984.
- [102] PANOFSKY, H. A., TENNEKES, H., LENSCHOW, D. H., AND WYNGAARD, J. C. The characteristics of turbulent velocity components in the surface layer under convective conditions. *Bound.-Lay. Meteorol.* 11, 3 (1977), 355–361.

- [103] PARLANGE, M. B., EICHINGER, W. E., AND ALBERTSON, J. D. Regional scale evaporation and the atmospheric boundary layer. *Rev. Geophys.* 33, 1 (1995), 99–124.
- [104] PERRIER, E. R., ROBERTSON, J., MILLINGTON, R., AND PETERS, D. Spatial and temporal variation of wind above and within a soybean canopy. *Agr. Meteorol.* 10 (1972), 421–442.
- [105] PONOMAREV, V. M., CHKHETIANI, O. G., AND SHESTAKOVA, L. V. Nonlinear dynamics of large-scale vortex structures in a turbulent Ekman layer. *Fluid Dyn.* 42, 4 (2007), 571–580.
- [106] POPE, S. B. *Turbulent flows*. Cambridge University Press, Cambridge, 2000.
- [107] QIU, X., CHENG, I., YANG, F., HORB, E., ZHANG, L., AND HARNER, T. Emissions databases for polycyclic aromatic compounds in the Canadian Athabasca oil sands region-development using current knowledge and evaluation with passive sampling and air dispersion modelling data. *Atmos. Chem. Phys.* 18, 5 (2018), 3457–3467.
- [108] RAJARATNAM, N. Skimming flow in stepped spillways. *J. Hydraul. Eng.* 116, 4 (1990), 587–591.
- [109] RANZATO, L., BARAUSSE, A., MANTOVANI, A., PITTARELLO, A., BENZO, M., AND PALMERI, L. A comparison of methods for the assessment of odor impacts on air quality: Field inspection (VDI 3940) and the air dispersion model CALPUFF. *Atmos. Environ.* 61 (2012), 570–579.
- [110] RASAM, A., BRETHERWER, G., SCHLATTER, P., LI, Q., AND JOHANSSON, A. V. Effects of modelling, resolution and anisotropy of subgrid-scales on large-eddy simulations of channel flow. *J. Turbul.*, 12 (2011), N10.
- [111] RAUPACH, M. R., ANTONIA, R. A., AND RAJAGOPALAN, S. Rough-wall turbulent boundary layers. *Appl. Mech. Rev.* 44, 1 (1991), 1–25.
- [112] RAZA, S., AVILA, R., AND CERVANTES, J. A 3-D Lagrangian stochastic model for the meso-scale atmospheric dispersion applications. *Nucl. Eng. Des.* 208, 1 (2001), 15–28.
- [113] REYNOLDS, A. J. The prediction of turbulent Prandtl and Schmidt numbers. *Int. J. Heat Mass Tran.* 18, 9 (1975), 1055–1069.
- [114] REYNOLDS, A. M. Incorporating terminal velocities into Lagrangian stochastic models of particle dispersal in the atmospheric boundary layer. *Sci. Rep.* 8, 1 (2018), 1–8.
- [115] ROCHETTE, P., AND ERIKSEN-HAMEL, N. S. Chamber measurements of soil Nitrous Oxide flux: Are absolute values reliable? *Soil Sci. Soc. Am. J.* 72, 2 (2008), 331–342.

- [116] RODOVALHO, E., QUAGLIO, O., FLESCH JUNIOR, W. S., PASCUAL, R., DE TOMI, G., AND SOARES TENÓRIO, J. A. Reducing GHG emissions through efficient tire consumption in open pit mines. *J. Clean. Prod.* 255 (2020), 120185.
- [117] ROTACH, M. W., AND ZARDI, D. On the boundary-layer structure over highly complex terrain: Key findings from map. *Q. J. Roy. Meteor. Soc.* 133, 625 (2007), 937–948.
- [118] ROTH, M. Review of atmospheric turbulence over cities. *Q. J. Roy. Meteor. Soc.* 126, 564 (2000), 941–990.
- [119] RUGGERI, M., LANA, N., ALTAMIRANO, J., AND PULIAFITO, S. Spatial distribution, patterns and source contributions of POPs in the atmosphere of Great Mendoza using the WRF/CALMET/CALPUFF modelling system. *Emerg. Contam.* 6 (2020), 103–113.
- [120] RZESZUTEK, M. Parameterization and evaluation of the CALMET/CALPUFF model system in near-field and complex terrain-terrain data, grid resolution and terrain adjustment method. *Sci. Total Environ.* 689 (2019), 31–46.
- [121] SANDHAM, J., AND WAITE, M. L. Spectral energy balance in dry convective boundary layers. *J. Turbul.* 16, 7 (2015), 650–675.
- [122] SATHE, A., MANN, J., BARLAS, T., BIERBOOMS, W. A. A. M., AND VAN BUSSEL, G. J. W. Influence of atmospheric stability on wind turbine loads. *Wind Energy* 16, 7 (2013), 1013–1032.
- [123] SCIRE, J. S., STRIMAITIS, D. G., AND YAMARTINO, R. J. A user’s guide for the CALPUFF dispersion model. Tech. rep., Earth Tech, Inc, Concord, 2000.
- [124] SEIBERT, P. Inverse dispersion modelling based on trajectory-derived source-receptor relationships. In *Air Pollution Modeling and Its Application XII*, S.-E. Gryning and N. Chaumerliac, Eds., vol. 22. Springer, New York, 1998, pp. 711–713.
- [125] SERGENT, M. E. *Vers une méthodologie de couplage entre la simulation des grandes échelles et les modèles statistique*. PhD thesis, École Centrale De Lyon, Lyon, 2002.
- [126] SHI, Y., FENG, X. S., WEI, F. S., AND JIANG, W. Three dimensional nonhydrostatic numerical simulation for the PBL of an open pit mine. *Bound-Lay. Meteorol.* 94, 2 (2000), 197–224.
- [127] SILVESTER, S. A., LOWNDES, I. S., AND HARGREAVES, D. M. A computational study of particulate emissions from an open pit quarry under neutral atmospheric conditions. *Atmos. Environ.* 43, 40 (2009), 6415–6424.

- [128] SÓWKA, I., PACIOREK, M., SKOTAK, K., KOBUS, D., ZATHEY, M., AND KLEJNOWSKI, K. The analysis of the effectiveness of implementing emission reduction measures in improving air quality and health of the residents of a selected area of the lower Silesian Voivodship. *Energies* 13, 15 (2020), 4001.
- [129] SÓWKA, I., SKRETOWICZ, M., SOBCZYŃSKI, P., AND ZWOŹDZIAK, J. Estimating odour impact range of a selected wastewater treatment plant for winter and summer seasons in Polish conditions using CALPUFF model. *Int. J. Environ. Pollut.* 54, 2-4 (2014), 242–250.
- [130] SPEZIALE, C. Turbulence modeling for time-dependent RANS and VLES: A review. *Am. Inst. Aeronaut. Astronaut. J.* 36, 2 (1998), 173–184.
- [131] STULL, R. B. *An introduction to boundary layer meteorology*. Kluwer Academic Publishers, Dordrecht, 1988.
- [132] TANG, S., HUANG, S., YU, H., GU, M., AND TANG, J. Impact of horizontal resolution in CALMET on simulated near-surface wind fields over complex terrain during Super Typhoon Meranti (2016). *Atmos. Res.* 247 (2021), 105223.
- [133] THÉ, J., AND YU, H. A critical review on the simulations of wind turbine aerodynamics focusing on hybrid RANS-LES methods. *Energy* 138 (2017), 257–289.
- [134] THOMAS, T. G., AND WILLIAMS, J. J. R. Generating a wind environment for large-eddy simulation of bluff body flows. *J. Wind Eng. Ind. Aerodyn.* 82, 1 (1999), 189–208.
- [135] TOMASI, E., GIOVANNINI, L., FALOCCHI, M., ANTONACCI, G., JIMÉNEZ, P. A., KOSOVIC, B., ALESSANDRINI, S., ZARDI, D., DELLE MONACHE, L., AND FERRERO, E. Turbulence parameterizations for dispersion in sub-kilometer horizontally non-homogeneous flows. *Atmos. Res.* 228 (2019), 122–136.
- [136] TUKKARAJA, P., KEERTHIPATI, M., AND FRENCH, A. Simulating temperature inversions in surface mines using computational fluid dynamics. *Proceedings of the South Dakota Academy of Science* 95 (2016), 119–124.
- [137] VAN DER LAAN, M. P., KELLY, M. C., AND SØRENSEN, N. N. A new k-epsilon model consistent with Monin-Obukhov similarity theory. *Wind Energy* 20, 3 (2017), 479–489.
- [138] VAN DRIEST, E. R. On turbulent flow near a wall. *J. Aeronaut. Sci.* 23, 11 (1956), 1007–1011.
- [139] WANG, W., SHAW, W. J., SEIPLE, T. E., RISHEL, J. P., AND XIE, Y. An evaluation of a diagnostic wind model (CALMET). *J. Appl. Meteorol. Clim.* 47, 6 (2008), 1739–1756.

- [140] WHITEMAN, C. D., HAIDEN, T., POSPICHAL, B., EISENBACH, S., AND STEINACKER, R. Minimum temperatures, diurnal temperature ranges, and temperature inversions in limestone sinkholes of different sizes and shapes. *J. Appl. Meteorol.* *43*, 8 (2004), 1224–1236.
- [141] WHITEMAN, C. D., MUSCHINSKI, A., ZHONG, S., FRITTS, D., HOCH, S. W., HAHNENBERGER, M., YAO, W., HOHREITER, V., BEHN, M., CHEON, Y., CLEMENTS, C. B., HORST, T. W., BROWN, W. O. J., AND ONCLEY, S. P. METCRAX 2006: Meteorological experiments in Arizona’s Meteor Crater. *B. Am. Meteorol. Soc.* *89* (2008), 1665–1680.
- [142] WILSON, J., YEE, E., EK, N., AND D’AMOURS, R. Lagrangian simulation of wind transport in the urban environment. *Q. J. Roy. Meteor. Soc.* *135*, 643 (2009), 1586–1602.
- [143] WILSON, J. D., FLESCH, T. K., AND BOURDIN, P. Ground-to-air gas emission rate inferred from measured concentration rise within a disturbed atmospheric surface layer. *J. Appl. Meteorol. Clim.* *49*, 9 (2010), 1818–1830.
- [144] WILSON, J. D., FLESCH, T. K., AND CRENNNA, B. P. Estimating surface-air gas fluxes by inverse dispersion using a backward lagrangian stochastic trajectory model. In *Geophysical Monograph Series*, J. Lin, D. Brunner, C. Gerbig, A. Stohl, A. Luhar, and P. Webley, Eds. American Geophysical Union, Washington DC, 2012, pp. 149–162.
- [145] WILSON, J. D., AND SAWFORD, B. L. Review of Lagrangian stochastic models for trajectories in the turbulent atmosphere. *Bound.-Lay Meteorol.* *78* (1996), 191–210.
- [146] WU, H., ZHANG, Y., YU, Q., AND MA, W. Application of an integrated Weather Research and Forecasting (WRF)/CALPUFF modeling tool for source apportionment of atmospheric pollutants for air quality management: A case study in the urban area of Benxi, China. *J. Air Waste Manag. Assoc.* *68*, 4 (2018), 347–368.
- [147] XIE, B. *Improved vortex method for LES inflow generation and applications to channel and flat-plate flows*. PhD thesis, École Centrale De Lyon, Lyon, 2016.
- [148] XU, G., LUXBACHER, K. D., RAGAB, S., XU, J., AND DING, X. Computational fluid dynamics applied to mining engineering: A review. *Int. J. Min. Reclam. Env.* *31*, 4 (2017), 251–275.
- [149] YAKHOT, V., ORSZAG, S. A., AND YAKHOT, A. Heat transfer in turbulent fluids-I. pipe flow. *Int. J. Heat Mass Tran.* *30*, 1 (1987), 15–22.
- [150] YOU, Y., MOUSSA, S. G., ZHANG, L., FU, L., BECK, J., AND STAEBLER, R. M. Quantifying fugitive gas emissions from an oil sands tailings pond with open-path Fourier transform infrared measurements. *Atmos. Meas. Tech.* *14*, 2 (2021), 945–959.

- [151] YOU, Y., STAEBLER, R. M., MOUSSA, S. G., BECK, J., AND MITTERMEIER, R. L. Methane emissions from an oil sands tailings pond: A quantitative comparison of fluxes derived by different methods. *Atmos. Meas. Tech.* 14, 3 (2021), 1879–1892.
- [152] YUAN, Y., YANG, K., DU, C., AND FU, X. Study on Schmidt number of pollutant diffusion in urban street atmosphere. *Procedia Engineer.* 205 (2017), 1711–1717.

Appendix A

Literature Summary Tables: Flux Chamber (FC), Eddy Covariance (EC), and Flux Gradient (FG) Methods

Table A.1: Literature review of Flux Chamber (FC), Eddy Covariance (EC), and Flux Gradient (FG) methods on GHG emission flux quantification.

Reference	Technique	Description
Meyers et al. (1996) [90]	FG	Direct measurements of fluxes and gradients for CO ₂ and H ₂ O were made at the forest floor of a boreal forest, over a lake surface, and at the forest floor of a leafless deciduous forest. They performed the experiment to examine the equality of CO ₂ and H ₂ O exchange coefficients.

Horst (1999) [56]	EC	<p>The flux footprint is calculated for fluxes estimated by micro-meteorological profile techniques. They found that the upwind extent of the footprint for concentration-profile flux estimates is similar to that of the footprint for eddy-covariance flux measurements, when the eddy-covariance measurement is made at a height equal to the arithmetic mean of the highest and lowest profile measurement heights for stable stratification or the geometric mean for unstable stratification.</p>
Rochette and Eriksen-Hamel (2008) [115]	FC	<p>They performed the study to determine criteria for assessing the quality of soil N₂O flux measurements made using Non-Flow-Non-Steady-State (NFT-NSS) chambers, to evaluate NFT-NSS chamber methodologies used in the scientific literature, and to propose a minimum set of criteria for NFT-NSS chamber design and deployment methodology. They showed that the quality of soil N₂O flux measurements reported in the literature is often poor.</p>
You et al. (2021) [150, 151]	EC and FG	<p>They conducted the studies to compare the two measurement techniques. They showed that flux chambers underestimated the fluxes. Also, their results showed that larger footprints together with high spatiotemporal resolution of micro-meteorological flux measurement methods (EC and FG) may result in more robust estimates of GHG emissions.</p>

Appendix B

Literature Summary Tables: Computational Fluid Dynamics (CFD) Models

Table B.1: Literature review of CFD simulations over simple and complex terrains.

Reference	Features	Description
Baklanov (1995 and 2000) [11, 12]	Key Parameters	Numerical modeling, CFD, experiment, local processes of dynamics and pollution of the atmosphere.
	Domain	Open-pit, cirques.
	Methodology and Objective	Investigation of natural ventilation in valleys, hollows, and open-pits.
	Results	Modified $k - \epsilon$ model is suggested for case of stable stratification, an effective scheme of boundary conditions for velocity profiles, based on the developed similarity theory for stably-stratified ABL, is suggested.
Kim et al. (2000) [69]	Key Parameters	Wind flow, numerical simulation, RANS.
	Domain	Hilly terrain.
	Methodology and Objective	Combination of standard and RNG-based $k - \epsilon$ models with wall functions.
	Results	RNG-based $k - \epsilon$ turbulence model gave better results than the standard model.

Shi et al. (2000) [126]	Key Parameters	Non-hydrostatic, three-dimensional Planetary Boundary Layer (PBL), shortwave radiation of the sun, long wave radiation of earth-atmosphere system.
	Domain	Open-pit with 100 [m] depth.
	Methodology and Objective	The $k - \epsilon$ closure scheme, non-hydrostatic simulation of air circulation inside open-pit.
	Results	Re-production of the air circulation inside the cavity is predicted, which is responsible for the dilution of pollution inside the pit. Importance of mechanical and thermal forcing mechanisms controlling the evolution of the atmosphere inside the pit are noted.
Kumar et al. (2006) [71]	Key Parameters	LES, ABL, CFD.
	Domain	Homogeneous terrain.
	Methodology and Objective	Simulation of a diurnal cycle of ABL flow over a homogeneous terrain using LES with the Lagrangian scale-dependent dynamic subgrid-scale model.
	Results	They showed that the profiles of turbulent variables plotted as a function of Obukhov length show “hysteretic” behavior that implies non-unique dependence.
Brés and Colonius (2008) [19]	Key Parameters	DNS, compressible flow, three-dimensional instabilities.
	Domain	Open cavity.
	Methodology and Objective	Linear stability analysis, two-dimensional mean flow, homogeneous cavities in the span-wise direction.
	Results	The results show that the instabilities were hydrodynamic (rather than acoustic) in nature and arose from a generic centrifugal instability mechanism associated with the mean recirculating vortical flow in the downstream part of the cavity.
Silvester et al. (2009) [127]	Key Parameters	Fugitive dust emission, CFD, thermally-neutral condition.
	Domain	Quarry open-pit.
	Methodology and Objective	Modeling the dispersion and deposition of dust particles, ventilation of the pit.

	Results	Between 30 and 60% of the emitted mineral particles were retained within the quarry boundary, with near field deposition fraction of 50%.
Kang and Sung (2009) [63]	Key Parameters	Wind tunnel experiments, Particle Image Velocimetry (PIV).
	Domain	Open cavity.
	Methodology and Objective	Low Mach number turbulent flows, considering oscillation modes.
	Results	The formation and development of large-scale vortical structures within the separated shear layer over an open cavity is responsible for self-sustained oscillations.
Cheng and Liu (2011) [24]	Key Parameters	CFD, LES, pollutant dispersion.
	Domain	Two-dimensional (2D) urban street canyons.
	Methodology and Objective	Five sets of Large-Eddy Simulations (LES) performed to examine the characteristics of flows and pollutant dispersion in two-dimensional (2D) urban street canyons of unit building-height-to-street-width ratio in neutral, unstable, and stable thermal stratifications.
	Results	They showed that LES is able to simulate explicitly the complex flows and turbulence structures in the atmospheric boundary layer in a transient manner. Its results can be used to complement field measurements and laboratory observations in order to enrich the fundamental understanding of atmospheric transport processes.
Labois and Lakehal (2011) [72]	Key Parameters	CFD, LES, VLES, DES, tube bundle.
	Domain	Tube bundle.
	Methodology and Objective	Comparison of VLES to conventional RANS and LES for a flow across a tube bundle.

	Results	They showed that the main distinction between VLES and the standard LES is the determination of filter width with respect to the grid size. In pure LES, the filter width is associated with the grid size, while the filter width in VLES can be set arbitrarily at any value between the grid size and the large characteristic length-scales of the flow.
Flores et al. (2014) [39]	Key Parameters	CFD, LES, turbulent buoyant atmospheric flows and pollutant dispersion, open-pit mines.
	Domain	Idealized and real open-pit mines with 1 [km] depth.
	Methodology and Objective	Considering only wind and only surface heat flux and combination of wind and surface heat flux.
	Results	Buoyancy modifies the flow patterns that the purely mechanically-induced re-circulation generates inside the pit, reducing the particle residence time seen in the purely mechanical case (non-buoyant case).
Bhowmick (2015) [16]	Key Parameters	Air Pollution, CFD, PM _{0.1} and PM ₁₀ particles.
	Domain	Idealized open-pit with 400 [m] depth, actual open-pit with 480 [m] depth.
	Methodology and Objective	Power law profile of velocity, LES, RANS.
	Results	Influence of wind speed and cloud cover on the air circulation inside the pit are noted.
Gordon et al. (2015) [46]	Key Parameters	Aircraft-based measurement, air pollutant emission.
	Domain	Oil sand open-pit.
	Methodology and Objective	Top-down Emission Rate Retrieval Algorithm (TERRA), determine facility emissions of pollutants.
	Results	Uncertainty of the methane emission rates is estimated as less than 30%.
Choudhury and Bandopadhyay 2016 [25]	Key Parameters	Deep open-pit mine, pit slope and geometry effects, dispersion of pollutants, CFD.
	Domain	Hypothetical Arctic deep open-pit mine with 500 [m] depth.

	Methodology and Objective	Considering air inversion exacerbated by the natural topography of an open-pit mine, effect of low influent velocity and large gust velocities on the contaminant profiles in the mine.
	Results	While higher velocities of air could remove contaminant from the pit bottom, they could not remove contaminant from the pit entirely and necessitated artificial mitigation measures.
Tukkaraja et al. (2016) [136]	Key Parameters	CFD, RANS, hypothetical open-pit mine .
	Domain	Hypothetical open-pit mine.
	Methodology and Objective	CFD with a RANS method based on the $k - \epsilon$ turbulence model.
	Results	They showed that the gas and dust particles were trapped inside the pit under inversion conditions while they were dispersed in the absence of inversion.
Han et al. (2016) [51]	Key Parameters	Complex terrain, atmospheric boundary layer (ABL) flow.
	Domain	Wind farm with ups and downs.
	Methodology and Objective	LES method on OpenFOAM to model the air flow over a wind farm.
	Results	They introduced new boundary conditions for LES of ABL over real complex terrain.
Ghoreishi-Madiseh et al. (2017) [43]	Key Parameters	Seasonal thermal energy storage, mine ventilation, CFD.
	Domain	Rock-pit.
	Methodology and Objective	Utilizing naturally-available renewable energy source from seasonal cycle for heating and cooling of underground mines.
	Results	The seasonal thermal energy storage of the rock pit could assist thermal management in an underground mine and could reduce energy consumption for winter heating and summer cooling.
Aliabadi et al. (2018) [7]	Key Parameters	VLES method of air flow.
	Domain	Rectangular tunnel.
	Methodology and Objective	VLES for a flat surface with OpenFOAM.

	Results	They introduced the VLES model and a synthetic turbulence generator at the inlet for ABL simulations.
Joseph et al. (2018) [61]	Key Parameters	CFD, fugitive dust deposition.
	Domain	Surface quarry (artificial and actual terrain models).
	Methodology and Objective	Modeling dust clouds as volumetric emissions, dispersion simulation by coupling the flow-field with stochastic tracking of the particulates, simulation of both adiabatic and non-adiabatic atmospheric stability conditions.
	Results	The flow behaviour at the upwind and downwind edges of the pit resembled the flow over backward and forward facing steps.
Baray et al. (2018) [13]	Key Parameters	Aircraft-based measurements, methane (CH_4).
	Domain	Oil sand open-pit.
	Methodology and Objective	Emission rates of CH_4 determined for the five primary surface mining facilities using the mass-balance method.
	Results	These results demonstrate the large contributions ($\sim 45\%$) of a few tailings ponds sources to the total fugitive CH_4 emissions.
Lin et al. (2021) [81]	Key Parameters	CFD, RANS, LES, urban environment.
	Domain	Urban area.
	Methodology and Objective	CFD simulations using RANS and LES models on the near-field dispersion of high-buoyancy exhaust gas emitted from a building's wake and validated using a wind tunnel experiment.
	Results	They showed that in low-Reynolds number or highly thermally-stable flows, LES can predict the unsteady variation in flow and concentration fields more accurately than RANS models.

Appendix C

Literature Summary Tables: CALifornia PUFF (CALPUFF) Model

Table C.1: Literature review of CALMET/CALPUFF and hybrid simulations over simple and complex terrains.

Reference	Features	Description
Chang et al. (2003) [23]	Key Parameters	CALMET/CALPUFF, different kinds of emission sources involving instantaneous release of sulfur hexafluoride tracer gas.
	Domain	A mesoscale region with desert basins and mountains.
	Methodology and Objective	Using different kinds of emission sources involving instantaneous release of sulfur hexafluoride tracer gas in a mesoscale region with desert basins and mountains. Use of networks of surface wind observations and special radiosonde and pilot balloon soundings to compare the model results and the observations.
	Results	They showed that CALMET and CALPUFF can predict the wind field and plume in the horizontal direction better than vertical direction.
Cox et al. (2005) [27]	Key Parameters	CALMET, MCSCIPUF, SWIFT.
	Domain	Complex terrain environment.

	Methodology and Objective	Assessment of the performance of three diagnostic wind models (CALMET, MCSCIPUF, and SWIFT) by direct comparison against wind field data.
	Results	Their results showed that the models appear to have nearly equal ability to produce valid horizontal winds and all models performed the best during non-stable times, as would be expected when more mixing is present.
Li and Guo (2006) [78]	Key Parameters	CFD, CALPUFF, odor dispersion modeling, different thermal stability conditions.
	Domain	A 3000-sow farrowing farm.
	Methodology and Objective	Using wind and temperature vertical profiles in PBL from the CFD calculation to evaluate their effects on odor dispersion.
	Results	In both CFD and CALPUFF the odor traveled farther under thermally-stable conditions than thermally-unstable conditions. Higher odor concentration were predicted by CFD than CALPUFF.
Wang et al. (2008) [139]	Key Parameters	CALMET, MM5, lake breeze.
	Domain	Chicago shoreline.
	Methodology and Objective	Comparison of Fifth-Generation Penn State/NCAR Mesoscale Model (MM5) with CALMET. Statistical evaluations to quantify overall model differences in wind speed and direction over the domain.
	Results	They showed that below 850 [m] above the surface, relative differences in wind speed were about 25 to 40 % (layer averaged) and the differences became larger because of the limited number of upper-air stations near the studied domain. Their analyses implied that model differences were dependent on time because of time-dependent spatial variability in winds.
Arregocés et al. (2016) [8]	Key Parameters	CALPUFF, intake fraction, dispersion and transport modeling.
	Domain	Open-pit coal mine.

	Methodology and Objective	Simulation of dispersion and transport of PM ₁₀ due to the emissions of the mining activities, using concept of intake fraction.
	Results	A significant portion of intake fraction occurs beyond 45 [km] of the source, emphasizing the need for detailed long-range dispersion modeling.
Giaiotti et al. (2018) [44]	Key Parameters	CALPUFF, dry and wet deposition.
	Domain	Chernobyl Nuclear Power Plant.
	Methodology and Objective	211 surface stations, 194 precipitation stations, and 14 upper air stations imported as meteorological input for feeding the CALMET pre-processor.
	Results	The results show smoother contamination pattern than the reality because of fine structure of the depositions. The results show that the predicted contamination pattern depends strongly on the source term employed in the simulation.
Cui et al. (2020) [28]	Key Parameters	Field campaign consisting of ABL observations and tracer experiments in a hilly region, using CALMET/-CALPUFF.
	Domain	Hilly region of the Gobi Desert in northwest China.
	Methodology and Objective	Comparison of CALMET/CALPUFF modeling results with tracer experiments.
	Results	The comparison of the CALPUFF model with the tracer measurements indicated that under the condition of low topographic influence, the predictions of CALPUFF are in good agreement with the measurements for the near distance, but in the far distance because of wind shears and vertical thermal discontinuity, a general tendency toward under-prediction of the concentration was observed.
Ruggeri et al. (2020) [119]	Key Parameters	WRF/CALMET/CALPUFF, airborne levels of Persistent Organic Pollutants.
	Domain	Medium-sized urban area.

	Methodology and Objective	CALMET/CALPUFF modeling system to estimate airborne levels of Persistent Organic Pollutants (POPs) in a medium-sized urban area. Ingestion of WRF meteorological fields into CALMET.
	Results	Results exhibited that the WRF/CALMET/-CALPUFF modeling system predicts POPs airborne concentrations with reasonable accuracy at a local scale.
Tang et al. (2021) [132]	Key Parameters	WRF/CALMET.
	Domain	Super Typhoon Meranti (2016).
	Methodology and Objective	Ingestion of WRF meteorological fields into CALMET to investigate the impact of horizontal resolution on the simulated near-surface wind fields of Super Typhoon Meranti (2016).
	Results	They indicated, by the reasonably large correlation coefficient (> 0.4) between the simulated and observed winds, that the performance of the WRF/CALMET coupled system was generally satisfactory. The simulation results appeared to improve slightly but continuously with higher horizontal resolution.

Appendix D

Literature Summary Tables: Lagrangian Stochastic (LS) Model

Table D.1: Literature review of Lagrangian Stochastic (LS) simulations over simple and complex terrains.

Reference	Technique	Description
Raza et al. (2001) [112]	Key Parameters	LS, Gaussian Plume Model (GPM).
	Domain	Meso-scale.
	Methodology and Objective	Comparison of the LS and GPM models.
	Results	They demonstrated the need for meso-scale atmospheric dispersion simulations, which provide better accuracy compared to the GPM approach.
Cassiani et al. (2015) [22]	Key Parameters	LS.
	Domain	Spore and pollen dispersal in vegetated areas.
	Methodology and Objective	Corrections to the LS model with respect to air density gradient, turbulence parameterizations, and settling velocity.
	Results	Their results show improvement in the accuracy of the model.
Ferrero and Maccarini (2021) [32]	Key Parameters	LS.
	Domain	Pollution dispersion.
	Methodology and Objective	Turbulence and advection-diffusion parameterizations.

	Results	The results showed that the parameterization for the variance dissipation time-scale, tested in neutral conditions, can be used also in stable and unstable conditions and in low-wind speed conditions.
Fattal et al. (2021) [30]	Key Parameters	LS.
	Domain	Pollutant dispersion from urban traffic.
	Methodology and Objective	Development of a mass-consistent LS model for pollutant dispersion with hybrid flow modelling.
	Results	They demonstrated the positive effect of urban green space on the reduction of concentration profiles.

Appendix E

Literature Summary Tables: Inverse Dispersion Modelling (IDM) Methods

Table E.1: Literature review of IDM simulations over simple and complex terrains.

Reference	Features	Description
Flesch et al. (1995) [37]	Key Parameters	bLS, IDM.
	Domain	Experimental farm field.
	Methodology and Objective	Examination of the relationship between forward and backward dispersion models.
	Results	They showed that IDM has many possible implementations based on combinations of dispersion models and gas sensor types.
Flesch et al. (2004) [36] and Wilson et al. (2010, 2012) [143, 144]	Key Parameters	bLS, IDM, ground to air emission.
	Domain	Experimental farm field.
	Methodology and Objective	Inference of the gas emission rate from an artificial surface area source using line-average concentration measured by an open-path laser situated up to 100 [m] downwind.
	Results	Using a backward Lagrangian stochastic model, a theoretical relationship was established for each experimental trial by simulating an ensemble of fluid-element paths arriving in the laser beam under the prevailing micrometeorological conditions.
	Key Parameters	bLS, IDM, Ammonia.
Flesch et al. (2005) [35]		

	Domain	Swine farm.
	Methodology and Objective	Inverse dispersion technique to diagnose gas emissions (ammonia) from a swine farm.
	Results	They showed that a backward Lagrangian stochastic model gives the emission-concentration relationship, so that downwind gas concentration establishes emissions.
	Key Parameters	Methane emission, micro-meteorological mass difference technique (MMD), IDM.
Gao et al. (2009) [41]	Domain	Experimental farm field.
	Methodology and Objective	MMD and the bLS methodologies for estimating CH ₄ emissions.
	Results	The simplified MMD and the bLS inverse dispersion techniques provided equally-accurate measurements of source emissions from the ensemble of release trials, inverse dispersion technique is preferable due to its simplicity.
	Key Parameters	IDM, data filtering.
Flesch et al. (2014) [33]	Domain	Experimental farm field.
	Methodology and Objective	Inverse dispersion technique to infer the emission rate of gas sources from concentration measurements and dispersion model calculations. Examination of the selection of measurement intervals having wind conditions conducive to the technique's accuracy on the basis of a short-range tracer experiment.
	Results	They showed that by introducing a supplementary condition of measuring vertical temperature gradient the technique is compatible with Monin–Obukhov similarity theory. It was possible to use a less stringent threshold for the friction velocity than has been previously used.
	Key Parameters	Agricultural gas emissions, flux measurements, IDM.
Hu et al. (2016) [57]	Domain	Experimental farm field.
	Methodology and Objective	Analysis on a trace gas dispersion experiment with multiple point sources and line-averaging laser gas detectors.

	Results	The unwanted impact of the terrain is adequately compensated by representing detector light paths as curves. The quality of the inversions is less sensitive to extreme temperature stratification than has been reported for other trials.
Liao et al. (2019) [79]	Key Parameters	Open-path laser, IDM, bLS.
	Domain	Vegetable greenhouse area.
	Methodology and Objective	Examination of the ability of an inverse dispersion technique, in combination with an open-path laser system, for measuring NH ₃ emissions from a vegetable greenhouse.
	Results	Determination of the area and height of the greenhouse sources are critical to emission estimates.

Appendix F

Surface-Layer Profiles

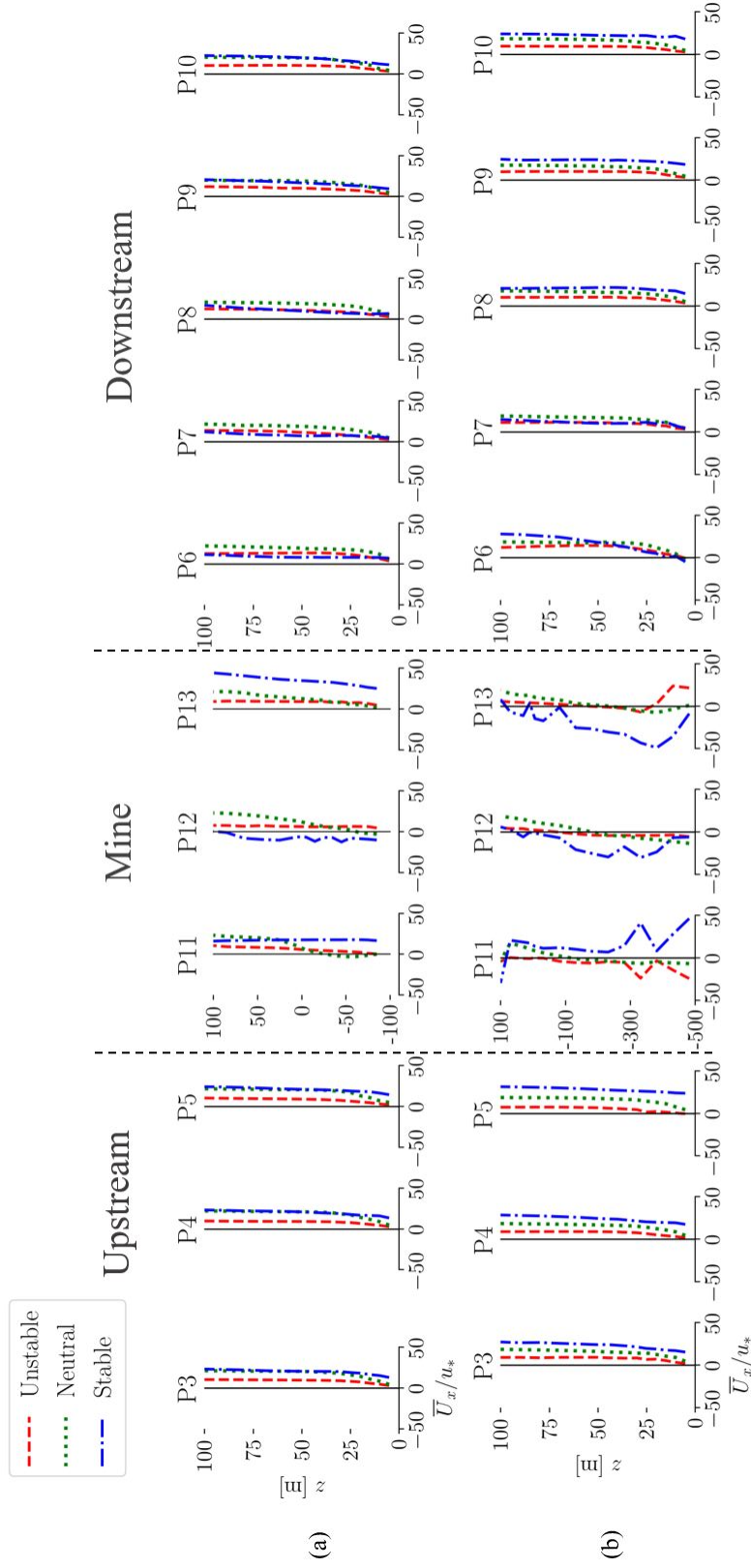


Figure F.1: Profiles of normalized mean velocity in the x -direction (\overline{U}_x) outside (P3 to P10) and inside (P11 to P13) the mine for different thermal stability cases and topographies; a) shallow and b) deep mines.

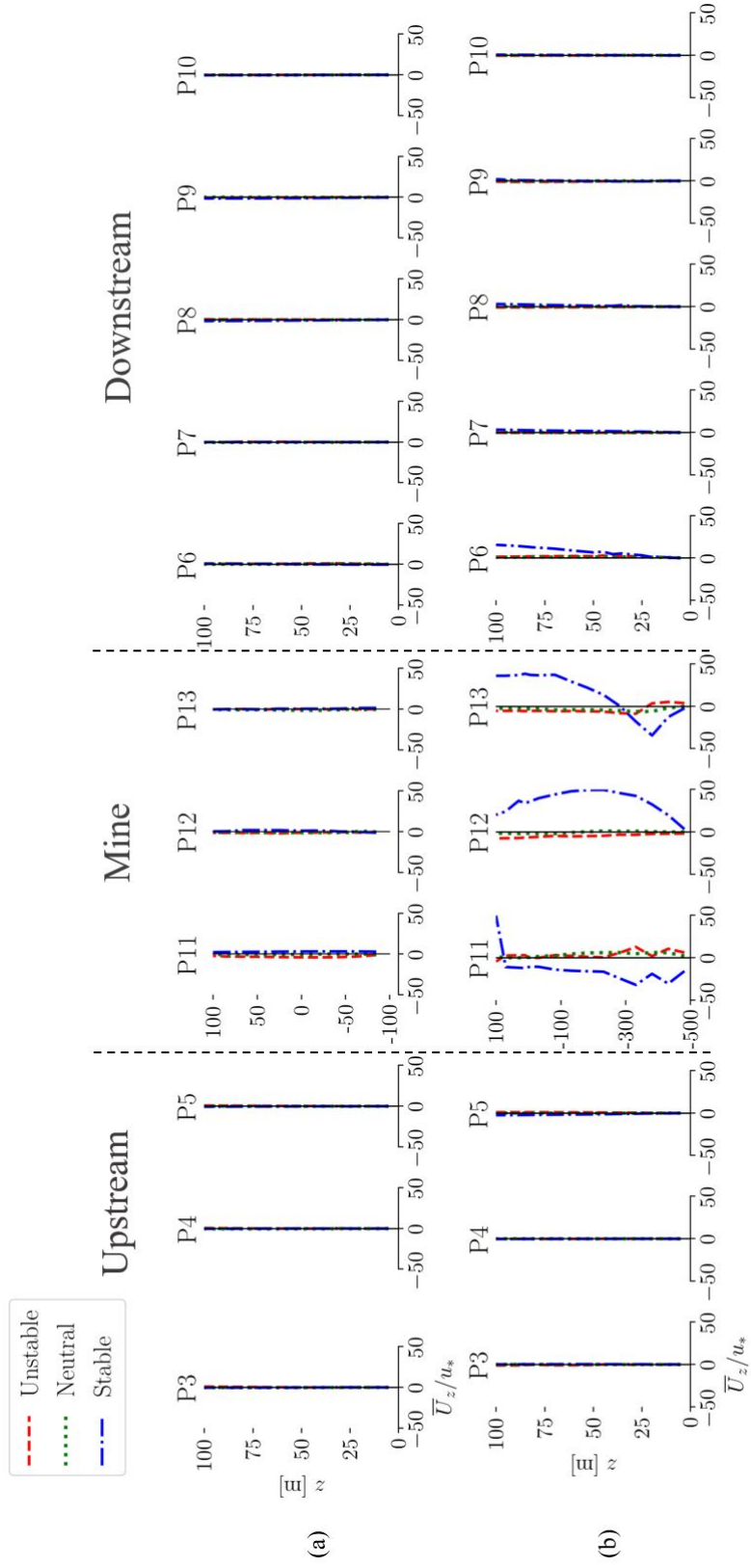


Figure F.2: Profiles of normalized mean velocity in the z -direction (\overline{U}_z) outside (P3 to P10) and inside (P11 to P13) the mine for different thermal stability cases and topographies; a) shallow and b) deep mines.

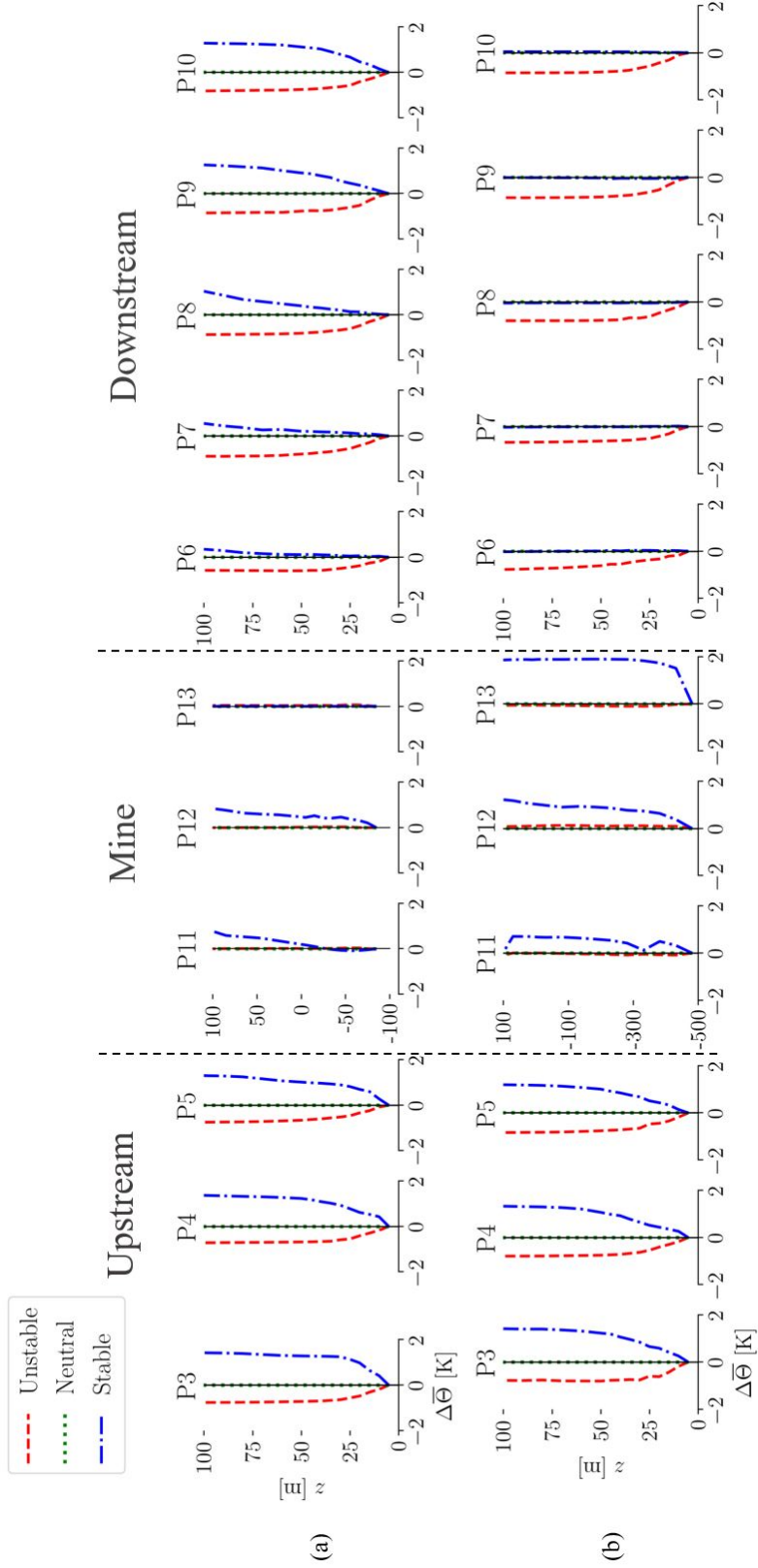


Figure F.3: Profiles of change in mean potential temperature from the surface ($\bar{\Theta}$) outside (P3 to P10) and inside (P11 to P13) the mine for different thermal stability cases and topographies; a) shallow and b) deep mines.

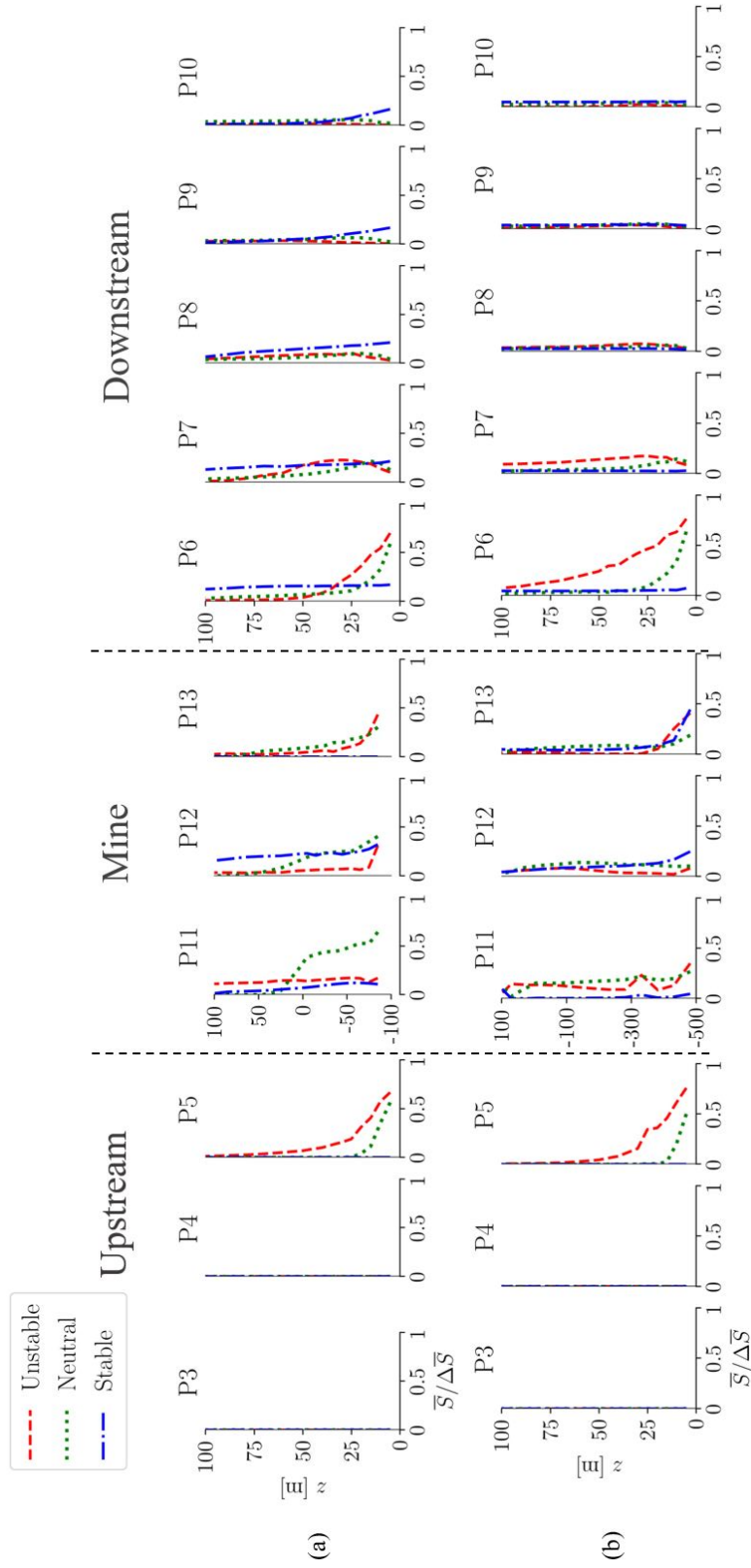


Figure F.4: Profiles of normalized mean mixing ratio (\bar{S}) outside (P3 to P10) and inside (P11 to P13) the mine for different thermal stability cases and topographies; a) shallow and b) deep mines.

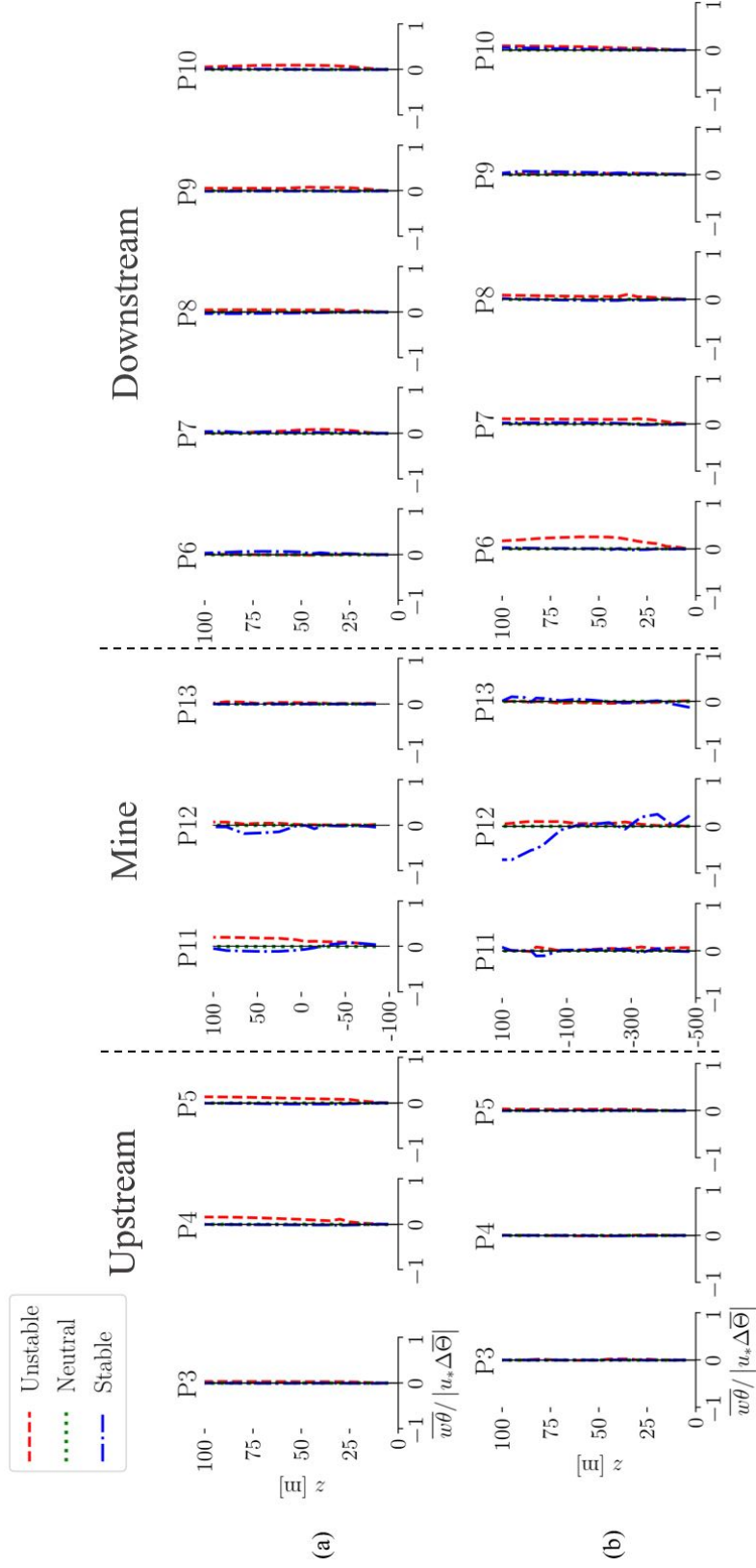


Figure F.5: Profiles of normalized turbulent sensible kinematic vertical heat flux ($\overline{w\theta}$) outside (P3 to P10) and inside (P11 to P13) the mine for different thermal stability cases and topographies; a) shallow and b) deep mines.

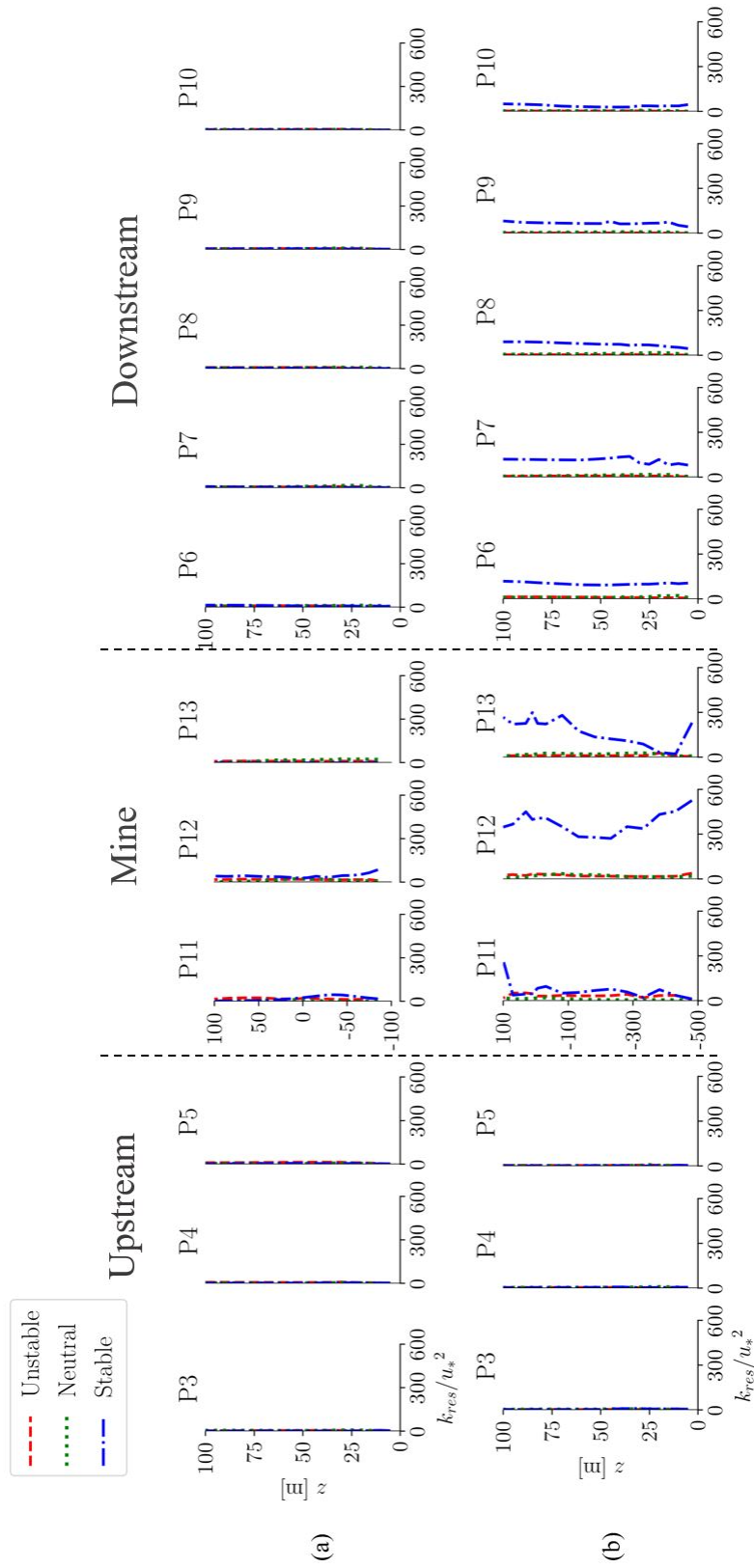


Figure F.6: Profiles of the normalized resolved TKE (k_{res}) outside (P3 to P10) and inside (P11 to P13) the mine for different thermal stability cases and topographies; a) shallow and b) deep mines.

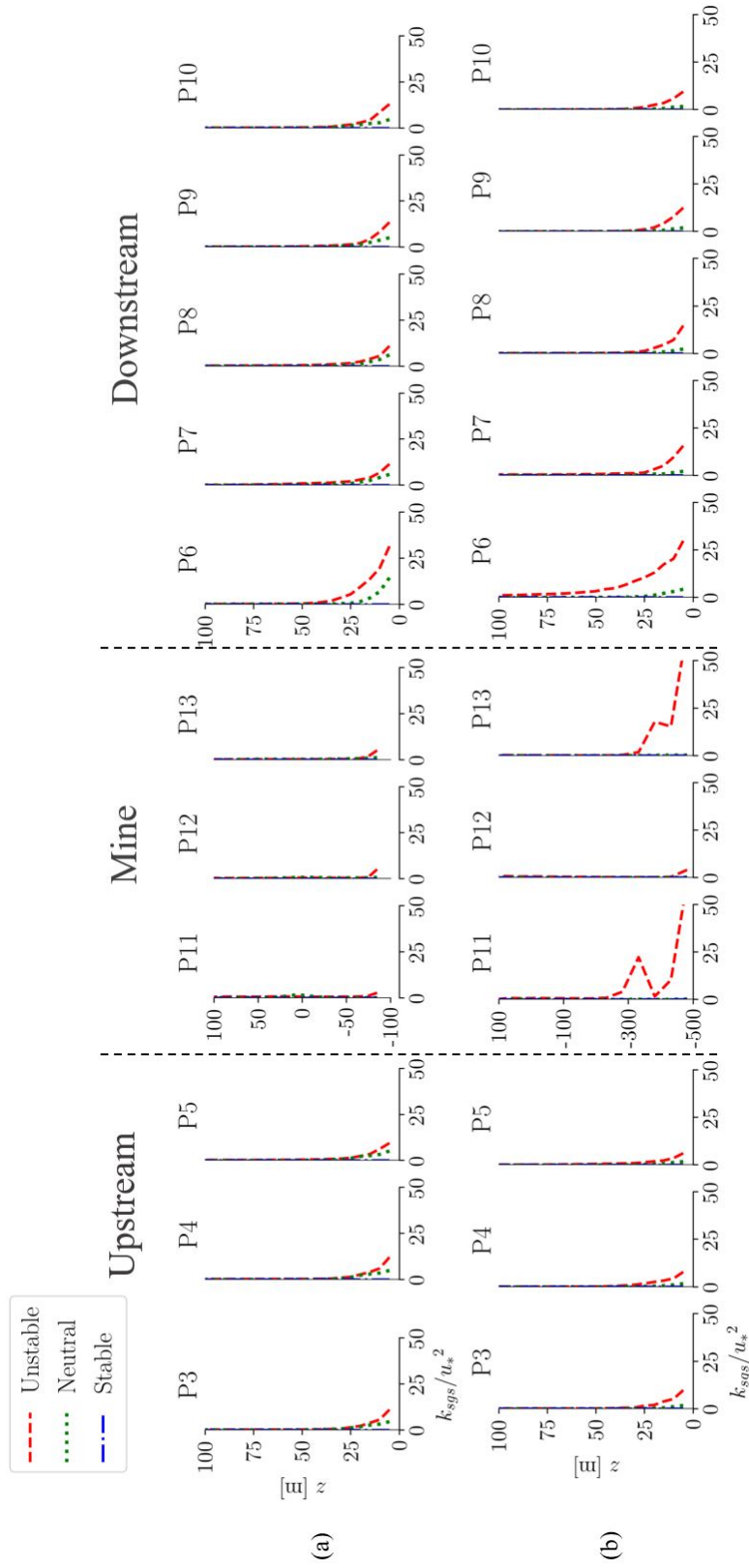


Figure F.7: Profiles of the normalized sub-grid TKE (k_{sgs}) outside (P3 to P10) and inside (P11 to P13) the mine for different thermal stability cases and topographies; a) shallow and b) deep mines.

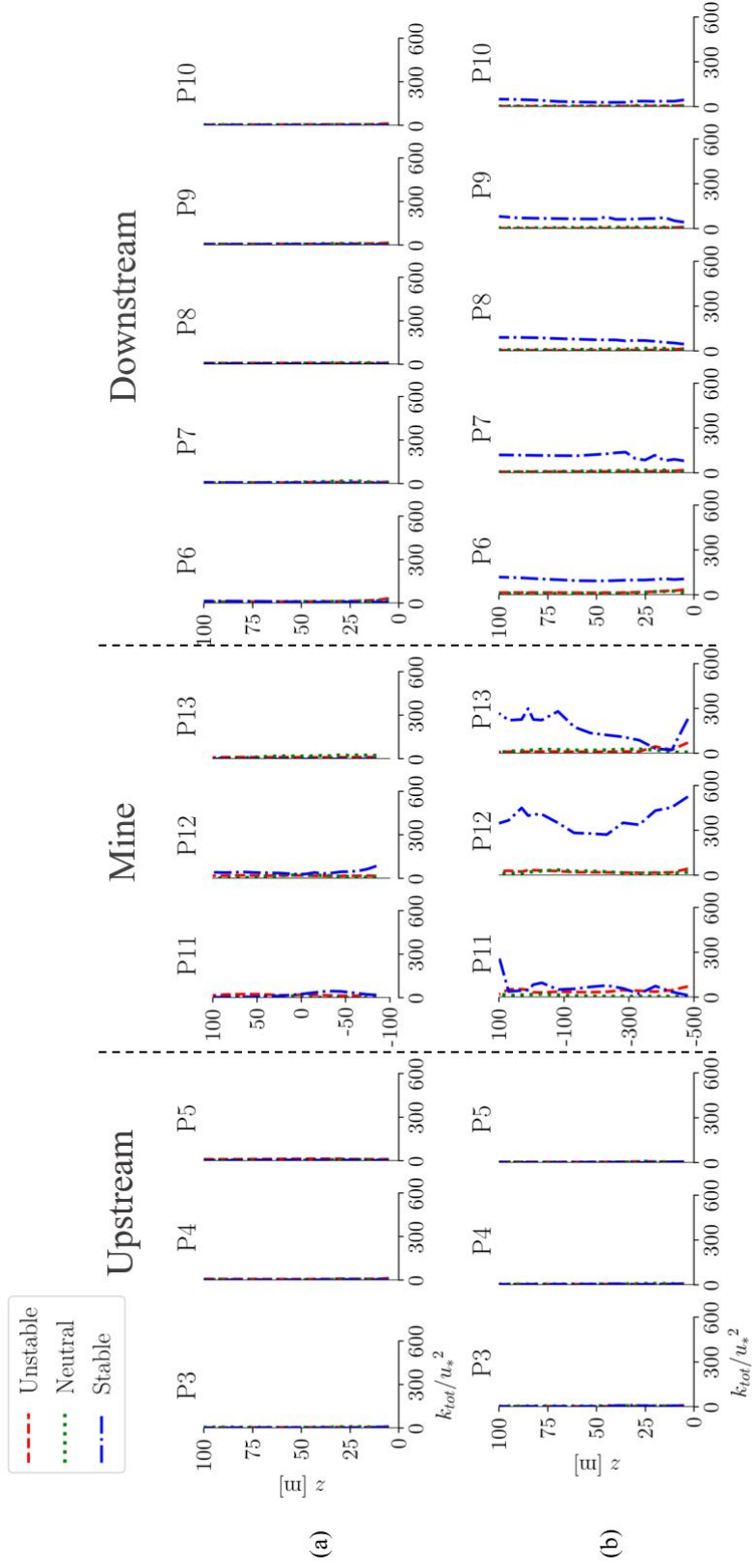


Figure F.8: Profiles of the normalized total TKE ($k_{tot} = k_{res} + k_{sgs}$) outside (P3 to P10) and inside (P11 to P13) the mine for different thermal stability cases and topographies; a) shallow and b) deep mines.

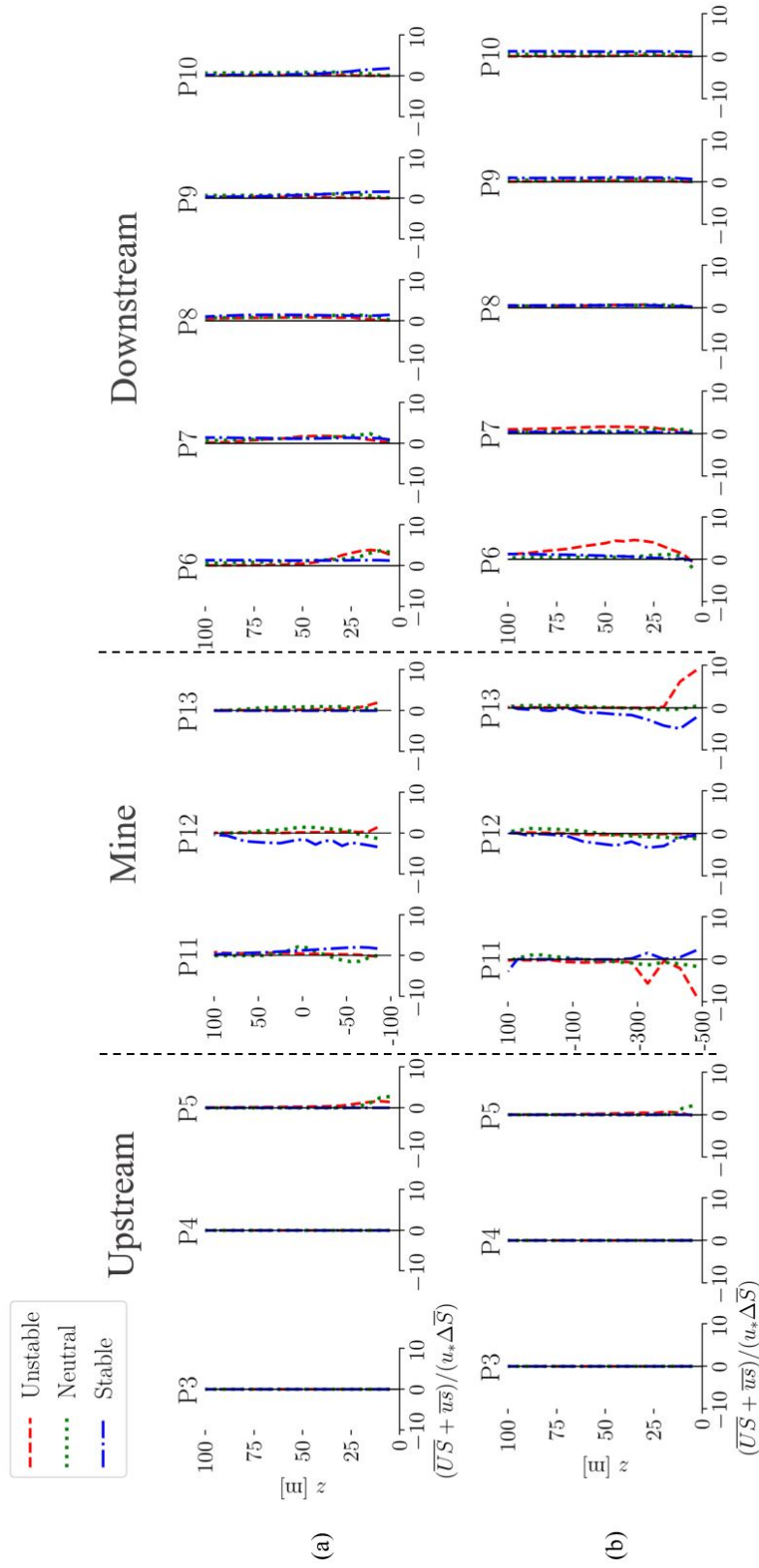


Figure F.9: Profiles of normalized advective plus turbulent flux of passive scalar in the x -direction ($\overline{US} + \overline{us}$) outside (P3 to P10) and inside (P11 to P13) the mine for different thermal stability cases and topographies; a) shallow and b) deep mines.

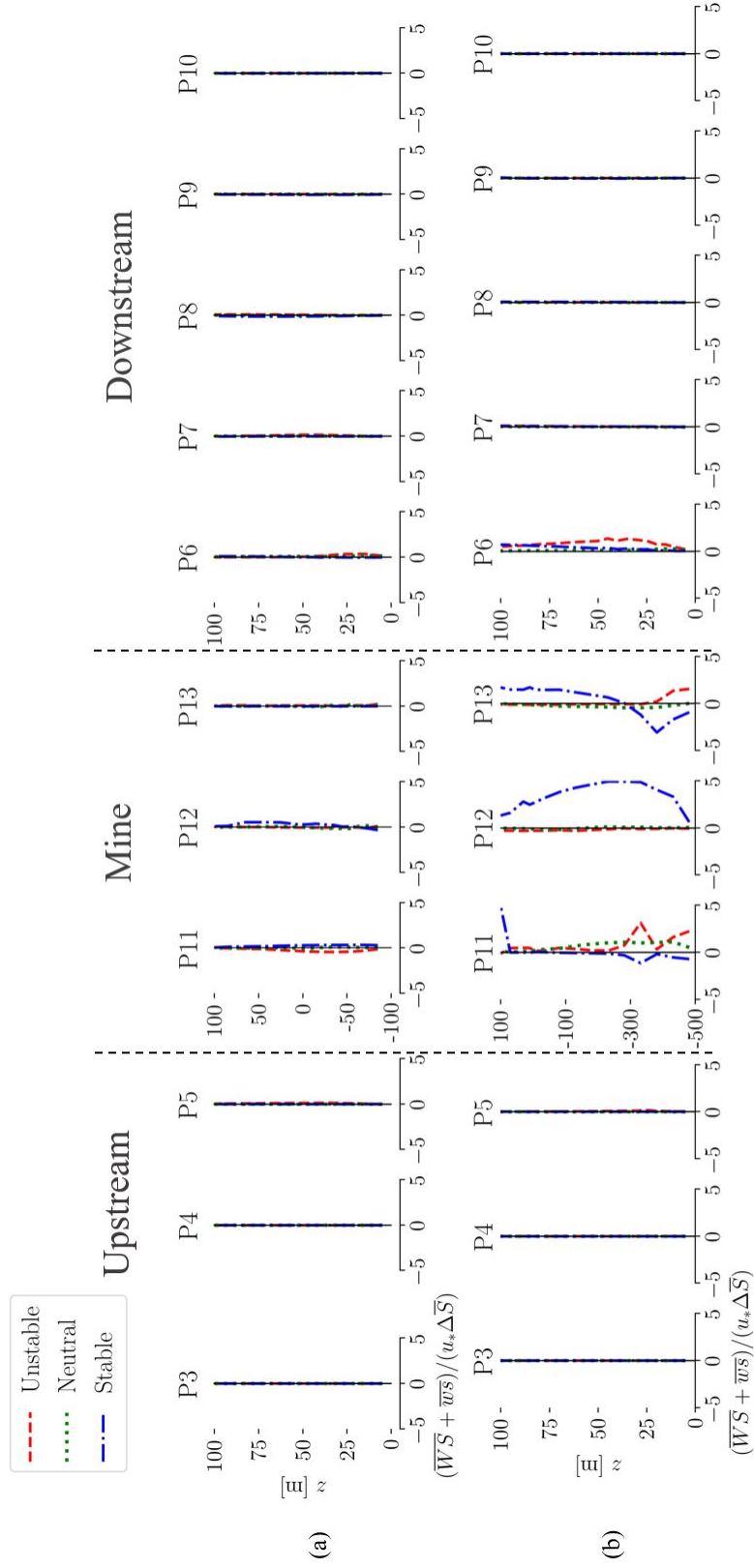


Figure F.10: Profiles of normalized advective plus turbulent flux in the z -direction ($\overline{WS} + \overline{ws}$) outside (P3 to P10) and inside (P11 to P13) the mine for different thermal stability cases and topographies; a) shallow and b) deep mines.

Appendix G

Code and Data Availability

The VLES code is available under the GNU v3.0 license at GitHub <https://github.com/AmirAAliabadi/VLESv1.0.0>. The Lagrangian Stochastic (LS) code is available via Drs. Thomas Flesch and John Wilson at the University of Alberta. The CALPUFF View 8.6.0 software is developed by Lakes Environmental Software and is available at <https://www.weblakes.com/>. The field environmental data may be shared with the authorization of the data owners.

Appendix H

Published Work

H.1 Peer-Reviewed Journal Papers

1. Kia, S., Flesch, T. K., Freeman, B. S., and Aliabadi, A. A. Atmospheric transport over open-pit mines: The effects of thermal stability and mine depth. *J. Wind Eng. Ind. Aerod.* 214 (2021), 104677. [Chapter 1, 2, 3, 4].
2. Kia, S., Flesch, T. K., Freeman, B. S., and Aliabadi, A. A. How well do CALPUFF and CFD-LS compare when predicting gas dispersion from open-pit mines? and the prospects for emission quantification using IDM. *J. Wind Eng. Ind. Aerod.* (2021), under review. [Chapter 1, 2, 3, 4].

H.2 Refereed Conferences

1. Kia, S., Flesch, T. K., Freeman, B. S., and Aliabadi, A. A. Atmospheric transport over open-pit mines: The effects of thermal stability and mine depth. In *Proceedings of Air & Waste Management Association 114th Annual Conference & Exhibition* (14-17, June, 2021), United States.